

Investigation of the Supernova Remnants 1006 and N132D in prospect of the *eROSITA* mission

Master's Thesis in Physics

Presented by
Melanie Lang
26.05.2020

Dr. Karl Remeis Sternwarte Bamberg
Friedrich-Alexander-Universität Erlangen-Nürnberg



Supervisor: Prof. Dr. Manami Sasaki

Abstract

When stars reach the end of their lifetime some of them explode in a supernova. The remainders of these violent explosions are so called supernova remnants (SNRs). Depending for instance on the type of the supernova, the density and distribution of the ambient medium, and the time that has passed since the explosion the morphology of the supernova remnant shows different characteristics. Therefore, these remainders can give hints about the composition and the properties of their progenitors before their death. Supernova remnants can be observed in all wavelength bands – from the radio and infrared via optical and UV light up to X-rays and γ -rays. X-ray emission provides insights into the extreme conditions inside a supernova remnant.

The latest mission that performs an all-sky survey in the X-ray regime is the *eROSITA* mission which was launched in July 2019. During its all-sky survey phase it will cover many supernova remnants and will allow to further investigate these objects. Predictions for this mission so far mainly concentrated on point-like sources and extended sources like supernova remnants were not in the focus of these studies. Therefore, the aim of this thesis is to investigate two supernova remnants in prospect of the *eROSITA* mission and to give first insights into the visibility of SNRs by *eROSITA*. Before going into a detailed analysis the theory behind supernovae and supernova remnants as well as the principles of X-ray telescopes will be explained. In order to be able to predict the results of the *eROSITA* all-sky survey phase regarding supernova remnants it is necessary to study the basic properties of a supernova remnant. For this task the Galactic SNR 1006 was chosen. Due to its position above the Galactic plane in a relatively clean environment it is possible to derive an undisturbed description of a supernova remnant. The information on the properties of the supernova remnant 1006 obtained from the analysis of *XMM-Newton* data will then be used as an input for simulations of this object during the *eROSITA* all-sky survey phase.

Finally, a calibration observation of the supernova remnant N132D located in the Large Magellanic Cloud which was obtained at the beginning of the *eROSITA* mission will be investigated. This study allows to evaluate the performance of the *eROSITA* instrument regarding supernova remnants during a pointed observation instead of an all-sky survey observation. Furthermore, this analysis will give hints on the visibility of supernova remnants and the ability to determine their properties during the all-sky survey phase of the *eROSITA* mission.

Zusammenfassung

Manche Sterne explodieren in einer Supernova, sobald sie das Ende ihres Lebens erreicht haben. Die Überreste einer solchen Explosion werden Supernova Überreste genannt. In Abhängigkeit von beispielsweise dem Typ der Supernova, der Dichte und der Verteilung des umliegenden Materials oder der Zeit, die seit der Explosion vergangen ist, weisen Supernova Überreste eine unterschiedliche Gestalt und Form auf. Aus diesem Grund können sie Hinweise auf die Zusammensetzung und die Eigenschaften der Sterne geben, aus denen sie entstanden sind. Supernova Überreste können in allen Wellenlängen-Bereichen beobachtet werden – von Radio und Infrarot über optisches und UV-Licht bis hin zu Röntgen- und Gammastrahlung. Die Emission im Röntgenbereich erlaubt Einblicke in die extremen Bedingungen im Inneren eines Supernova Überrests.

Die neueste Mission, die eine komplette Durchmusterung des Himmels im Röntgenbereich durchführt, ist die *eROSITA*-Mission, welche im Juli 2019 gestartet wurde. Während der Phase, in der sie den kompletten Himmel abscannt, wird sie viele Supernova Überreste beobachten und es so ermöglichen, diese Objekte weiter zu untersuchen. Bisherige Vorhersagen für diese Mission hatten sich meist auf punktförmige Quellen konzentriert, weshalb ausgedehnte Objekte wie Supernova Überreste nicht im Fokus ihrer Studien standen. Deshalb ist das Ziel dieser Masterarbeit, zwei Supernova Überreste im Hinblick auf die *eROSITA*-Mission zu untersuchen und erste Einblicke in die Sichtbarkeit von Supernova Überresten durch *eROSITA* zu geben. Zu Beginn werden die Theorie hinter einer Supernova und ihrem Überrest ebenso wie die Grundprinzipien von Röntgenteleskopen erklärt. Um Vorhersagen über die Ergebnisse der Himmelsdurchmusterung von *eROSITA* in Bezug auf Supernova Überreste treffen zu können, ist es notwendig, die Eigenschaften eines solchen Objektes zu studieren. Dafür wurde der galaktische Überrest 1006 ausgewählt, der es aufgrund seiner Lage oberhalb der galaktischen Ebene in einer relativ reinen Umgebung ermöglicht, eine ungestörte Beschreibung eines Supernova Überrests zu erzielen. Informationen über seine Eigenschaften wurden anhand der Auswertung von *XMM-Newton*-Daten erhalten und werden als Input für die Simulationen dieses Objekts für *eROSITA* dienen.

Abschließend wird eine Kalibrationsbeobachtung des Supernova Überrests N132D analysiert, welcher sich in der Großen Magellanschen Wolke befindet. Die Auswertung dieser Beobachtung, die zu Beginn der *eROSITA*-Mission durchgeführt wurde, erlaubt es, die Leistungsfähigkeit des *eROSITA*-Instruments in Bezug auf Supernova Überreste anhand einer gezielten Beobachtung anstelle eines Himmelsscans zu beurteilen. Dadurch gibt die Auswertung dieser Beobachtung Hinweise auf die Sichtbarkeit von Supernova Überresten und die Möglichkeit, ihre Eigenschaften zu bestimmen, während der Himmelsdurchmusterungsphase der *eROSITA*-Mission.

Contents

1	Introduction	6
2	Supernovae	8
2.1	Core collapse supernovae	9
2.2	Thermonuclear supernovae	10
3	Supernova Remnants	12
3.1	Classification of Supernova Remnants	12
3.2	Evolution of Supernova Remnants	13
3.2.1	Free expansion phase	13
3.2.2	Sedov phase	14
3.2.3	Radiative phase	15
3.2.4	Merging phase	16
3.3	Analytical description	16
3.4	X-ray emission from Supernova Remnants	19
3.4.1	Thermal X-ray emission	19
3.4.2	Line emission associated with radioactivity	21
3.4.3	Non-thermal emission	22
3.5	Particle acceleration by Supernova Remnants	24
4	X-ray telescopes	25
4.1	Basic principles	25
4.1.1	Wolter telescopes	25
4.1.2	X-ray CCDs	26
4.2	<i>XMM-Newton</i>	27
4.2.1	EPIC	30
4.3	The <i>eROSITA</i> mission	31
4.3.1	Technical characteristics	33
4.3.2	Survey strategy	34
5	<i>XMM-Newton</i> data analysis of the Galactic SNR 1006	37
5.1	Description of SNR 1006	37
5.2	Observational details	38
5.3	Data reduction	39
5.4	Sources of background contamination	40
5.5	Region definition	42
5.6	Spectral modelling	43
5.7	Estimating the age of SNR 1006	46
5.8	Preparing the simulation	49

6	Simulation and data extraction software for <i>eROSITA</i>	54
6.1	SIMPUT	54
6.2	SIXTE	55
6.3	eSASS	57
6.4	Data extraction without the use of eSASS	57
7	Simulations of SNR 1006 for <i>eROSITA</i>	59
7.1	The SIMPUT file of SNR 1006	59
7.2	Simulation results after one complete scan of the sky	59
7.3	Simulation results after four years of all-sky survey	60
7.3.1	Spectral analysis	60
7.3.2	Summary of the simulations	72
8	Analysis of <i>eROSITA</i> data of SNR N132D	74
8.1	Description of SNR N132D	74
8.2	Observational details and data reduction	76
8.3	Light leak in TM5 and TM7	76
8.3.1	Investigation of the amount of background counts	76
8.3.2	Influence on the background spectra	80
8.3.3	Estimating the influence of the light leak on the flux	82
8.3.4	Possible reason for the light leakage	83
8.4	Spectral analysis of the individual telescope modules	84
8.4.1	Contribution of the background	84
8.4.2	Spectral analysis	87
8.5	Estimating the age of the LMC SNR N132D	92
9	Conclusion and outlook	96
9.1	The Galactic SNR 1006	96
9.1.1	Analysis of <i>XMM-Newton</i> data	96
9.1.2	Results of the simulation for the <i>eROSITA</i> all-sky survey	96
9.2	The LMC SNR N132D	98
9.2.1	Light leak in TM5 and TM7	98
9.2.2	Spectral analysis of the individual telescope modules	99
9.2.3	Estimating the age of the LMC SNR N132D	100
9.3	Outlook	100
	References	102
	Acknowledgment	106
	Eigenständigkeitserklärung	108

1 Introduction

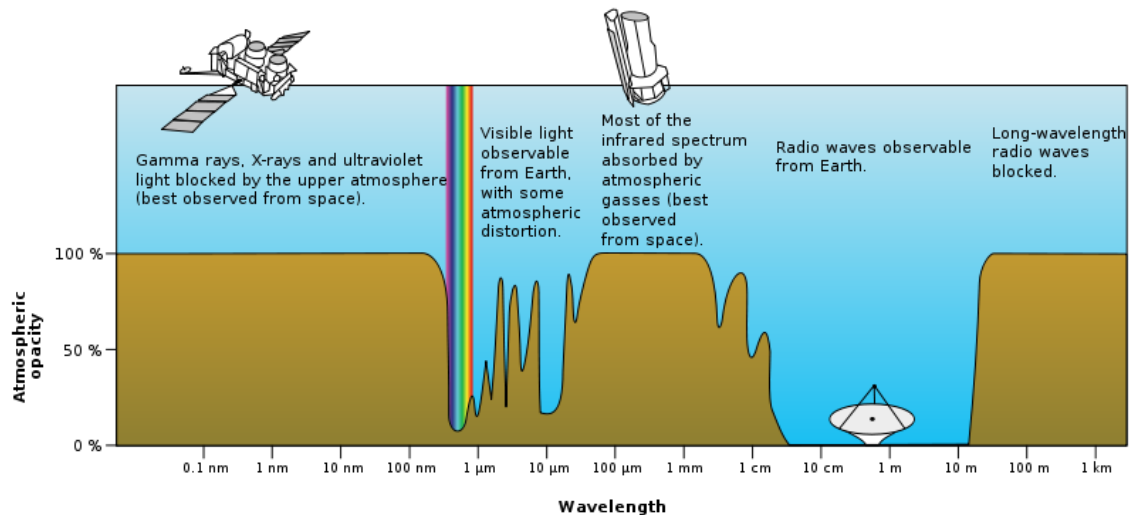


Figure 1.1: The atmospheric window (taken from <https://i.stack.imgur.com/p8dD0.png>; accessed on 2020 April 4). Only the emission of some wavelength bands reaches the Earth's surface. Others like X-rays are blocked by the atmosphere.

Astronomy is not only fascinating a small number of experts but also a large number of laymen. Thinking of astronomy the first thing that comes to someone's mind is the night sky with its multitude of stars. Although it is not visible in the night sky the most well known star is our Sun. This picture will be followed by an image of the Earth, our planet. Continuing these thoughts even further might lead to black holes, the probably most famous extremes of our universe. But there are more extreme objects like an explosion of a star, a so called supernova. The remainder of such an explosion, a supernova remnant, can give hints on the composition and properties of the star before its death. These objects can be studied in all wavelength bands from radio via infrared, visible light, and UV to X-rays and γ -rays. The extreme conditions inside supernova remnants are investigated best in X-rays. However, unlike the situation of radio and visible light it is not possible to observe X-ray emission from the Earth's surface. As visualized in Fig. 1.1 the atmospheric opacity varies as a function of the wavelength. In particular X-ray emission is blocked by the atmosphere and does not reach the Earth's surface. Therefore, it is necessary to place X-ray telescopes above the Earth's atmosphere in space. In this thesis two X-ray telescope missions are presented which were used to study the properties of two supernova remnants and to predict the possibilities of the most recently launched X-ray telescope mission in the prospect of supernova remnants.

The thesis is structured as follows: at first the theory of supernovae and supernova remnants is explained in chapters 2 and 3, respectively. This is followed in chapter 4 by an introduction to the working principle of X-ray telescopes and an overview of the two missions (*XMM-Newton* and *eROSITA*) of which observations were analyzed. Chapter 5 describes the data analysis of the first supernova remnant, SNR 1006, studied in this thesis. The results of this analysis were used to perform simulations of that remnant for the recently launched X-ray telescope mission *eROSITA* in chapter 7. Before the results of the simulations are presented, chapter 6 gives an introduction to the simulation software. Finally, in chapter 8 a calibration observation of the second supernova remnant, the LMC SNR N132D, taken by the new instrument was analyzed. The major results of the work presented in this thesis are summarized in chapter 9.

2 Supernovae

Even few hundreds of years ago the sudden appearance and fading of very bright objects on the sky has been observed. These objects can reach luminosities up to those of galaxies, which can be nicely seen in Fig. 2.1, where the images of two photo plates are shown. In the earlier taken plate on the left a galaxy is visible, whereas in the right image also a new source can be seen with a luminosity comparable to that of the galaxy. Nowadays, we know that these phenomena mark the end of the lifetime of stars and we call them supernovae (SNe). Supernovae play an important role in our understanding of the universe. They give insights in the chemical evolution of the universe, are an important energy source for the interstellar medium (ISM), and some special types of them can be even used as standard candles in cosmology. Since these events are quite rare, only 2–3 events per century occur in a typical spiral galaxy like the Milky Way. Their remainders, the so called supernova remnants (SNRs), reveal details about the explosion mechanism and probe the immediate surroundings of the SN. In addition, they allow to study collisionless shocks and particle acceleration (Vink, 2012). But what exactly are supernovae? And how are they created?

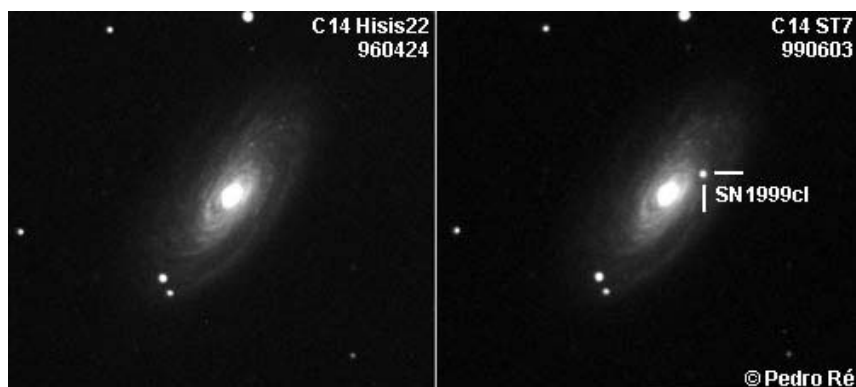


Figure 2.1: Comparison of plates for SN1999d. The supernova was discovered on 1999 May 29 by the Lick Observatory Supernova Search. The left image shows the host galaxy observed in 1996, whereas the right image was taken in June 1999. The bright new source is a supernova of Type Ia (taken from Vitale, 2004, but image property of Pedro Ré).

Supernovae are caused by the explosion of stars. Historically, one distinguished two types of SNe called Type I and Type II (see Fig. 2.2). This distinction goes back to Minkowski (1941) and is based on optical observations. SNe without hydrogen in the spectrum were classified as Type I. Consequently, those showing hydrogen in their spectra were classified as Type II. These classes are further subdivided into Type Ia showing silicon absorption lines and Type Ib and Ic, which both do not show silicon absorption lines. The difference between Type Ib and Ic is that Type Ib supernovae show helium

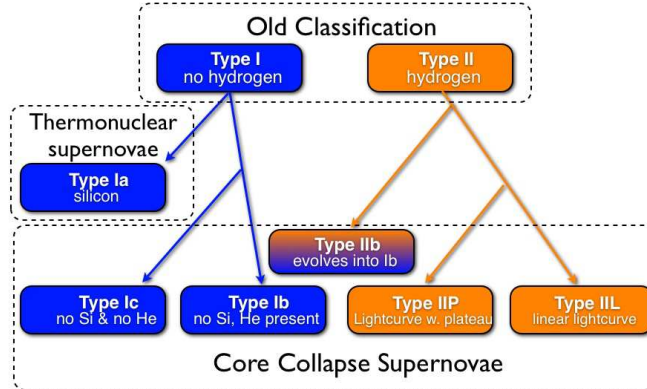


Figure 2.2: Classification of SNe (taken from Vink, 2012).

absorption lines in their spectra, whereas Type Ic SNe do not. Supernovae of Type II can be subdivided based on their lightcurves into Type IIP (plateau), Type IIL (linear lightcurve), and Type IIb, which evolves into a Type Ib supernova. There is one more type which is not listed in Fig. 2.2, the Type IIn SNe. This type is characterized by narrow hydrogen emission lines, which are thought to come from a dense circumstellar environment. Its place in the diagram is not quite clear (Vink, 2012; Filippenko, 1997; Helder et al., 2012).

According to the explosion mechanism, the current understanding is that there are only two different types of SNe, namely the thermonuclear SNe and the core collapse SNe. Only the Type Ia supernovae belong to the thermonuclear SNe, whereas all the other types are core collapse SNe (Vink, 2012; Helder et al., 2012).

2.1 Core collapse supernovae

Core collapse supernovae mark the end of the lives of massive stars ($M \gtrsim 8 M_{\odot}$) (see Woosley & Janka, 2005, for a review). Once the star reaches the silicon burning phase and produces iron in its core, its end is near since it cannot gain energy from the nuclear fusion of iron. The core starts to collapse, either into a neutron star if the degeneracy pressure of the nucleons is strong enough to balance gravitation, or into a black hole if it is not and the collapse ends in a gravitational singularity (Vitale, 2004). The amount of gravitational energy liberated by this process is approximately 10^{53} erg. Most of this energy is released in form of neutrinos (Vink, 2012).

The explosion mechanism works as follows (see, e.g., Irrgang, 2018): The iron core produced by silicon burning contracts until the electrons become a degenerate gas. Contraction becomes even more rapid once the degenerate core's mass surpasses the Chandrasekhar limit ($1.4 M_{\odot}$) because at this stage the electron degeneracy pressure is not capable of opposing self-gravity. Two types of instabilities develop. Firstly, electron capture accelerates the infall of matter, and secondly, the temperature rises unrestrained due to a low temperature sensitivity of highly degenerate gas. At some point, photons get energetic enough to disintegrate nuclei, which consumes energy. This loss of energy

then turns the collapse into almost free fall. This process continues until photons become energetic enough to break helium nuclei into protons and neutrons. Eventually, the free protons can capture the free electrons and turn into neutrons. This process absorbs energy as well as reduces the pressure, making the core collapse continue further. Finally, the neutron gas becomes degenerate which generates sufficient pressure to halt the collapse. But this abrupt deceleration leads to some rebound of matter resulting in pressure waves being sent outwards into the infalling material. The shock wave even gains in strength due to absorption of neutrinos by the compressed matter. This finally leads to an eruptive explosion during which the outer layers of the star are expelled. The ejected material therefore consists mainly of hydrogen, helium, carbon, oxygen, magnesium, silicon, and sulfur (Irrgang, 2018). As described above the distinction of core collapse supernovae to some extent was based on the presence or absence of absorption lines of certain elements in the spectra. For example, the absence of hydrogen and helium can be understood as the explosion of stars that have lost their hydrogen- and helium-rich envelope as a result of stellar wind mass loss or through binary interaction (Vink, 2012). Depending on its mass the remnant becomes either a neutron star or a black hole. Core collapse SNe have been observed in arms of spiral galaxies, where the young giant stars are located, but rarely in elliptical galaxies (Vitale, 2004).

2.2 Thermonuclear supernovae

In contrast to a core collapse supernova the progenitor of a thermonuclear supernova is not a massive star but a white dwarf (WD). White dwarfs represent the final stage in the lifetime of non-massive stars ($M \lesssim 8 M_{\odot}$). WDs are compact objects characterized by high surface temperatures and an internal pressure supplied by degenerate electrons. No nuclear reaction takes place in a WD. Usually, it slowly cools via radiating thermal energy away (Irrgang, 2018). But white dwarfs in a binary system can accrete matter from their companion, for instance via Roche-lobe overflow or through stellar winds. Once a C/O white dwarf has accreted a critical amount of material it undergoes a thermonuclear runaway process, which will result in an explosion completely disrupting the progenitor. This evolution is sketched in Fig. 2.3. A merger of two white dwarfs leads to the same result. Since the properties of the progenitor before the explosion are always similar, SNe of Type Ia can be used as cosmological standard candles (Vink, 2012). For this, an empirical relation between the peak brightness and the post peak decline rate of the lightcurve can be used (Phillips et al., 1992). Lightcurves of SNe of Type Ia consist of a fast rise and an exponential decay with a characteristic time of 55 days (Vitale, 2004). The determination of distances to SNe of Type Ia also gives evidence that the expansion of the universe is accelerating. For the discovery of that fact, Saul Perlmutter, Brian P. Schmidt, and Adam G. Riess received the nobel prize in 2011¹. Thermonuclear supernovae happen in all types of galaxies (Vitale, 2004). During the explosion process an energy amount of 10^{51} erg is released. Only 1% of this energy is emitted as visible light. The major part is available as kinetic energy to blow up the ejected material at a speed $> 10^7$ m s⁻¹ (Vitale, 2004; Soderberg et al., 2008; Helder et al., 2012).

¹ <https://www.nobelprize.org/prizes/physics/2011/summary/> (accessed on 2019 June 19)

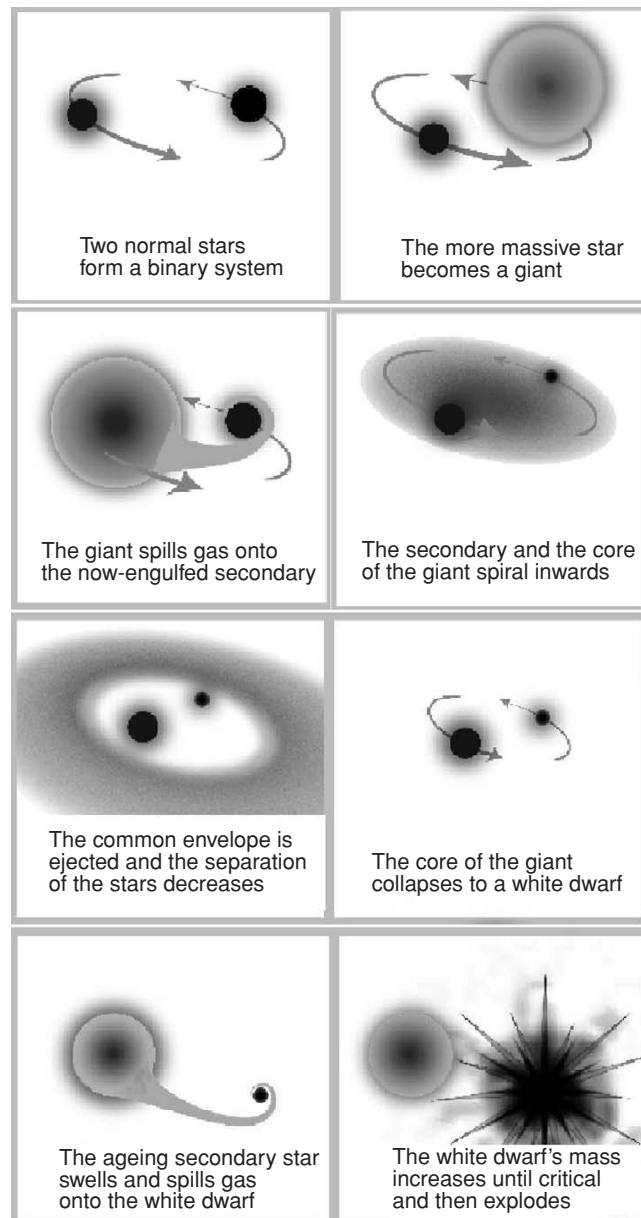


Figure 2.3: One mechanism to create a Type Ia supernova starting from a binary system with two normal stars (taken from Seward & Charles, 2010).

3 Supernova Remnants

Supernova remnants (SNRs) form after a supernova explosion and are a fascinating kind of astronomical sources. So far, about 300 SNRs in the Milky Way are known (Green, 2019). Inside the remnants interstellar gas is heated to temperatures of $10^6 - 10^7$ K. Furthermore, they add heavier chemical elements to the ISM, which were produced inside the progenitors or during the explosion. In addition, in the shock wave particles get accelerated to highly relativistic energies. Accelerated electrons produce synchrotron radiation, which makes SNRs bright radio sources. But they are also visible in other wavelength bands. For instance, in X-rays the emission of the thermal plasma can be observed. Non-thermal X-ray emission from electrons can also be detected in some young supernova remnants (Sasaki, 2019; Helder et al., 2012; Koyama et al., 1995; Vink, 2012).

3.1 Classification of Supernova Remnants

Naively, one would hope to be able to classify the remnants of supernova explosions in the same manner as the explosion itself into thermonuclear and core collapse SNRs. But often it is not possible to determine the origin of a remnant. For young remnants this can be done via X-ray spectroscopy. Contrary, in old SNRs the emission mainly comes from shocked interstellar gas, which means one has to rely on secondary indicators. The most reliable indicator is the presence of a neutron star inside the SNR. In this case, the origin of the remnant is a core collapse supernova (Vink, 2012). However, chance alignment has to be considered as well (Kaspi, 1998). A second indicator is the location of the remnant. Massive stars, the progenitors of core collapse SNe, can be found in star forming regions or in an OB association (e.g. Westerlund, 1969) since they are still quite young when they end their lives. But this cannot be taken as a proof for such an origin. On the contrary, a location high above the Galactic plane supports the hypothesis of a thermal SN origin. An example for that case is SN 1006 (Stephenson & Green, 2002).

These considerations show that it is difficult to establish the supernova origin of an SNR. Therefore, remnants are classified based on their morphology. The first recognized classes were shell-type SNRs, plerions, and plerionic composite SNRs. Shell-type SNRs are characterized by a limb brightened shell which is produced by the blast wave sweeping up interstellar medium and creating a shell of shock heated plasma (Vink, 2012). Famous examples of this type are Tycho's and Kepler's SNRs or the Cygnus Loop (Schaudel, 2003).

In the case of a neutron star being created in a core collapse SN, it may be expected to rotate rapidly. Due to this rotation it loses energy, which produces a wind of relativistic electrons and positrons. This terminates in a shock, where the particles are accelerated to ultra-relativistic energies. Now the particles can diffuse away from the shock and create a nebula of relativistic electrons and positrons (Vink, 2012). These emit via synchrotron radiation (radio to soft γ -ray bands) and inverse Compton scattering (soft γ -ray band to TeV band) (see Gaensler & Slane, 2006, for a review). The resulting nebula is called a

pulsar wind nebula. The most prominent example is the Crab Nebula (Vink, 2012), which is associated with the supernova of 1054 (Stephenson & Green, 2002). Since remnants like this do not exhibit a shell, but only bright central emission, they are called plerions. The name derives from the Greek word “pleres” which means “full” (Weiler & Panagia, 1978). Pulsar wind nebulae can be found around both young and old pulsars. It is debated if pulsar wind nebulae should be referred to as supernova remnants since the central emission is powered by the pulsar wind and not by the supernova explosion (Vink, 2012).

The last traditionally distinguished class are the plerionic composite SNRs. These are characterized by showing a shell and a plerion in radio as well as in X-rays. Examples for this class are Kes 75 and Vela (Sasaki, 2019). Here the central emission again comes from a pulsar wind nebula. Energetic pulsars with ages $\lesssim 20,000$ years are expected to already exhibit a pulsar wind nebula while they are still surrounded by the supernova remnant shell (Vink, 2012). Therefore, both the shell and the plerion are visible.

Imaging capabilities of X-ray satellites like *Einstein* and *ROSAT* improved the classification since the 1980s (Vink, 2012). They revealed that there is another class of SNRs, called the mixed morphology SNRs (Rho & Petre, 1998). This type shows a shell-type morphology in radio but a plerionic one in X-rays (White & Long, 1991; Rho & Petre, 1998). In general, these supernova remnants are relatively old and are associated with dense ISM (Vink, 2012) as the central emission comes from shocked clouds or, sometimes, also from a pulsar wind nebula (Sasaki, 2019).

Nowadays, sometimes even further types of SNRs are distinguished. For instance Type Ia SNRs or oxygen-rich SNRs. The latter ones are likely the remnants of the most massive stars and show enhanced oxygen abundances (Vink, 2012).

3.2 Evolution of Supernova Remnants

Like almost everything in the Universe supernova remnants are not stable but follow a specific evolution, which can be divided into four phases. These phases are called free expansion phase, Sedov phase, radiative phase, and merging phase. One should always keep in mind that this categorization into four phases is a simplification. It might not always be possible to assign a certain phase to a remnant. Even worse, different parts of a remnant can be in different phases (Vink, 2012).

3.2.1 Free expansion phase

In the first evolutionary phase of SNRs the expansion is dominated by the ejecta and lasts a few hundred years. During a supernova explosion approximately $10^{50} - 10^{51}$ erg of kinetic energy are available for ejecting masses in the order of few solar masses. The speed of the ejecta $v = \sqrt{2E_0/M_{ej}}$ is on the order of 10^7 m s^{-1} , whereas the sound speed in the ISM is on the order of 10^4 m s^{-1} . This means the ejecta’s motion through the ISM happens with a supersonic velocity, which causes the formation of a shock wave (Vitale, 2004). This shock wave, in turn, sweeps up the ambient ISM. However, the mass of the swept up material is negligible compared to the mass of the ejecta. Characteristic properties of this phase are a constant temperature within the supernova remnant and a constant expansion velocity of the shell (Seward & Charles, 2010). An example of an SNR in free expansion phase is the remnant of SN1987A. It is one of the youngest supernova remnants known

so far. Fig. 3.1 shows how its size changed from 1996 until 2003. The image shows the remnant in the optical (*HST*), the X-ray (*Chandra*), and the radio (*ATCA*) wavelength regime. Especially in X-rays and radio the increase of its size can be clearly seen.

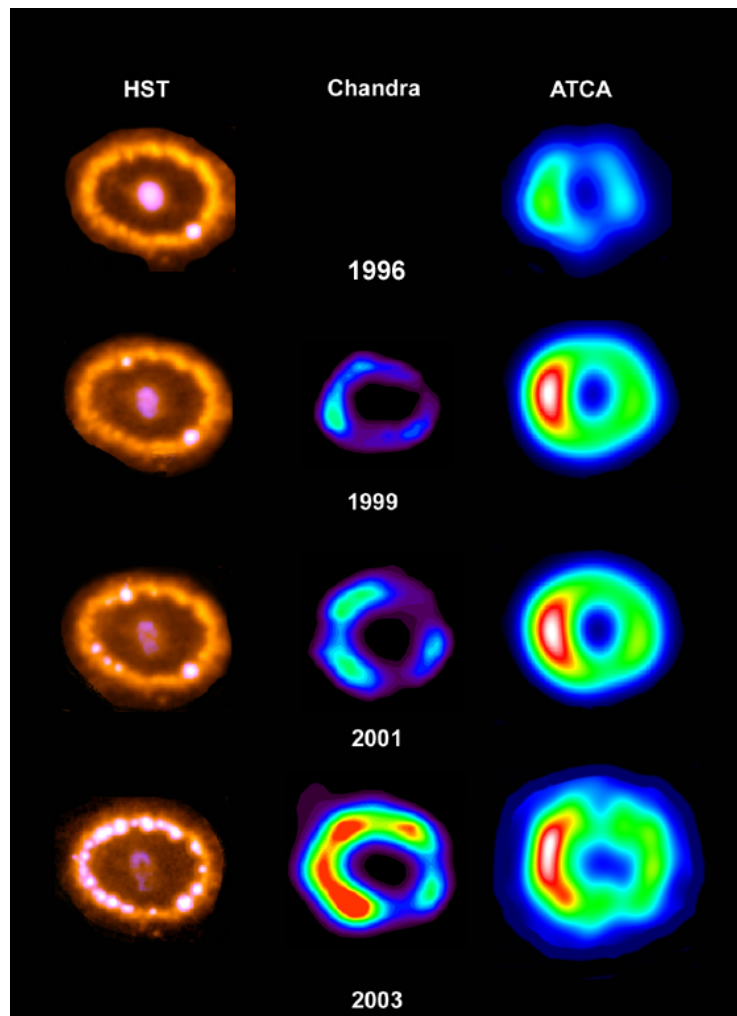


Figure 3.1: Expansion of SNR1987A in optical (*HST*), X-rays (*Chandra*), and radio (*ATCA*) (taken from <https://www.spacetelescope.org/static/archives/images/original/opo0409r.jpg>; accessed on 2019 August 29).

3.2.2 Sedov phase

The second evolutionary phase, the Sedov phase, is often also called the Sedov-Taylor or adiabatic phase. It is reached when the mass of the material swept up by the shock wave starts to become higher than the mass of the ejecta. In addition, the energy radiated away by the shell is still small compared to the internal energy of the SNR in this phase (Seward & Charles, 2010). The kinetic energy in terms of expansion energy is converted into internal energy of the system, which means the total energy stays roughly constant. This is the explanation why this phase is also called the adiabatic phase (Wilms, 2018). Only

the initial energy deposited by the explosion E_0 and the density of the ISM n determine the rate of expansion. While the forward shock is still moving away from the center of the supernova explosion, the interaction of the shock wave with the surrounding interstellar medium forms an additional shock wave that is directed inwards, the so called reverse shock (Seward & Charles, 2010). The formation of the reverse shock is a consequence of the internal part of the remnant being less affected by the resistance of the swept-up material, which slows down the external shock. Therefore, the relative velocity between the internal part and the external shock increases, generating a reverse shock (Vitale, 2004). The boundary between the ejecta and the circumstellar material is called contact discontinuity. Only the material between these two shock fronts is hot because the interstellar gas has been heated and compressed by the expanding ejecta. The material in the central region is still expanding freely. Since only the shocked material is hot enough to emit X-rays, the bright observed shells in young supernova remnants are formed (Seward & Charles, 2010). An example of a contact discontinuity is shown in Fig. 3.2. The figure depicts a color composite image of the SNR E0102-72 in X-rays, radio, and in the optical wavelength regime. The radio observations in red trace the forward shock, which is expanding into the surrounding material. In contrast, the X-ray emission in blue results from gas that has been heated by the reverse shock wave. This means, the contact discontinuity is located at the border between the radio and the X-ray emission since it separates the regions of shocked ejecta and shocked ISM. The optical emission in green shows filaments of dense clumps of colder gas within the remnant.

The shell of an SNR is Rayleigh-Taylor unstable and breaks into clumps since the shell of dense, shocked ejecta is gradually decelerated by lower density shocked circumstellar material (Blondin & Ellison, 2001). As the ejecta push against the shocked ISM at the contact discontinuity of an expanding remnant, the Rayleigh-Taylor instability causes finger-like structures, which protrude ahead of the originally spherical contact discontinuity. These structures themselves are unstable and the consequent turbulence leads to a mixing of the SNR's ejecta with the gas that was just shocked by the outer blast wave (Seward & Charles, 2010). A famous example where material is ejected beyond the outer blast wave is given by the SNR Cassiopeia A. An X-ray image of this source is depicted in Fig. 3.3. For instance, at the left-hand side of the image material can be seen which is clearly beyond the outer blast wave forming a jet-like structure. The results of a 3D simulation of Rayleigh-Taylor instabilities are illustrated in Fig. 3.4. The density of shocked and unshocked material is color-coded. White represents the density of unshocked circumstellar material, whereas black denotes the high density of the shocked ejecta. The figure shows that the forward shock remains spherical, although finger-like structures are formed (Blondin & Ellison, 2001).

This second evolutionary phase lasts between 10,000 and 20,000 years (Sasaki, 2019).

3.2.3 Radiative phase

The radiative or snowplow phase, is the third phase in the evolution of a supernova remnant. It begins after the shell has cooled down to around 5×10^5 K (Vink, 2012; Helder et al., 2012). Due to the decreasing temperature of the plasma electrons start to recombine with heavier atoms. The energy radiated away from the shell by this process can be observed as UV and optical line emission forming filaments (Vitale, 2004). This energy loss, in turn, cools the shell even faster. Therefore, the shell shrinks and becomes

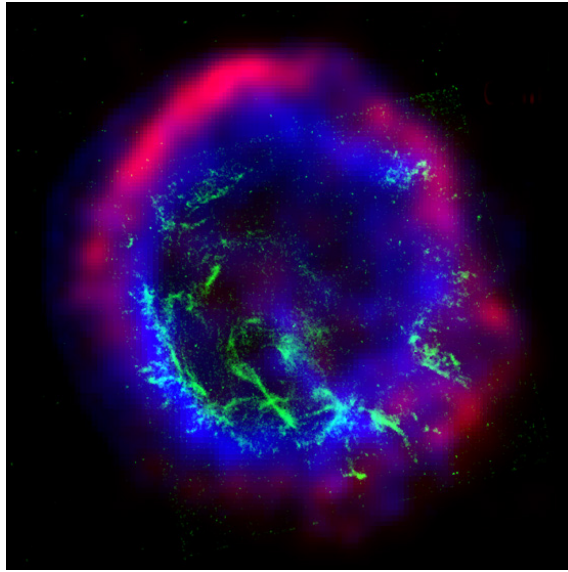


Figure 3.2: Composite image of the supernova remnant E0102-72, which is located in the Small Magellanic Cloud. In blue the X-ray image of *Chandra* is shown. In red radio observations taken with *ATCA* are depicted. Green symbolizes the optical wavelength regime represented by observations of the *HST* (Credit: X-ray: NASA/CXC/SAO, Optical: NASA/HST, Radio: CSIRO/ATNF/ATCA; taken from https://chandra.harvard.edu/photo/2000/0015multi/e0102_multi.jpg; accessed on 2020 March 03). In the image the forward as well as the reverse shock and the contact discontinuity are visible.

more dense. The expansion is no longer driven by energy conservation, but by pressure and, finally, momentum conservation (Sasaki, 2019; Helder et al., 2012). At the end of this phase, which lasts for about 100,000 years, most of the internal energy of the system has been radiated away (Vitale, 2004).

3.2.4 Merging phase

The end of the radiative phase also marks the end of the supernova remnant. As soon as the shock velocity becomes comparable to the turbulent velocity and the temperature behind the shock becomes comparable to the temperature of the ambient ISM, the remnant starts to get fainter and fainter and dissolves into the ISM (Sasaki, 2019). In the course of the merging, the elements which were produced during the supernova mix into the ISM and lead to a chemical enrichment. Furthermore, a huge amount of energy is released by an SNR. This energy heats the ISM, which would be much cooler without the energy injected by supernova remnants (Vitale, 2004).

3.3 Analytical description

Nowadays, there are analytical models describing the different phases in the lifetime of a supernova remnant. The early evolution can be described by a model by Chevalier (1982).

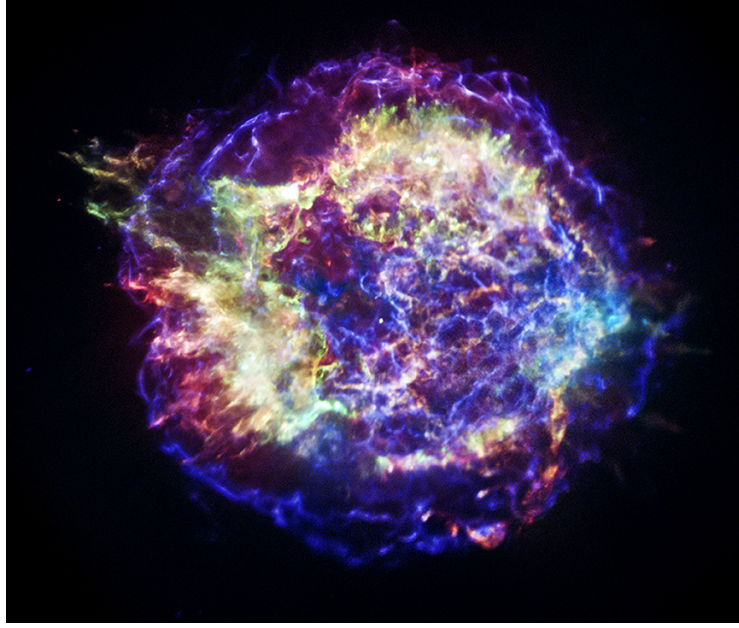


Figure 3.3: *Chandra* image of Cassiopeia A. Red denotes the 0.5–1.5 keV band, green the 1.5–2.5 keV band, and blue the 4.0–6.0 keV band. In this image material ejected beyond the nominal radius of the forward shock can be clearly seen (Credit: NASA/CXC/SAO; taken from <https://chandra.harvard.edu/photo/2013/casa/>; accessed on 2019 November 5).

The density distribution of the freely expanding ejecta is approximated by a powerlaw, $\rho_{\text{ej}} \propto v_{\text{ej}}^{-n}$, where $n = 7$ for thermal SNe, and $n = 9–12$ for core collapse SNe. These values are justified by numerical simulations. According to Chevalier (1982) a self-similar solution of the form $R_s \propto t^\beta$ can be applied (notation convention taken from Vink, 2012). R_s denotes the shock radius. The expansion parameter β is given by $\beta = \frac{n-3}{n-s}$, where s represents the powerlaw index of the distribution of a stationary medium with which the shock interacts. This model describes a self-similar velocity, pressure, and density structure. But it is important to stress that it only applies for the early evolution of an SNR, when the reverse shock has not reached the inner most ejecta (Vink, 2012).

Once the inner most ejecta are reached by the reverse shock, the Sedov-Taylor model applies (Sedov, 1959; Taylor, 1950). This model makes two main assumptions. The first one is that the explosion energy E_0 is instantaneously injected into a uniform medium with uniform density ρ_0 . And the second one that no energy losses occur (Vink, 2012). The model describes the adiabatic evolution of a spherical explosion. Since the solution is self-similar it is valid at all times after the explosion, therefore, the independent variables are r and t (Borkowski et al., 2001). The Sedov-Taylor model takes the continuity equation as well as the Euler equations for the adiabatic flow in a spherically symmetric geometry into account. Additionally, it respects the conservation of energy (Sasaki, 2019; Borkowski et al., 2001).

The first step of the self-similar approach is to introduce a dimensionless variable that connects r and t : $\xi = r/R(t)$ (Sasaki, 2019).

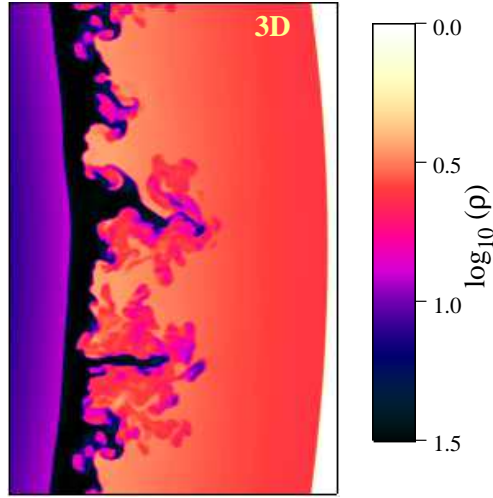


Figure 3.4: 3D simulated Rayleigh-Taylor instabilities. The colors depict the gas density which is scaled to the density of the preshock gas. White represents the low density of the unshocked circumstellar material and black the high density of the shocked ejecta (taken from Blondin & Ellison, 2001).

Since in the Sedov phase the energy is conserved, the sum of the kinetic and the internal energy must be constant:

$$E_0 \sim \underbrace{\frac{1}{2} \left(\frac{4\pi}{3} \right) \rho_0 R^3 v^2}_{\text{kinetic energy}} + \underbrace{A \rho_0 v^2 \left(\frac{4\pi}{3} \right) R^3}_{\text{internal energy}} = \text{const.} \quad (3.1)$$

Here, A denotes a constant. Solving the equation for $v = dR/dt$ yields

$$\frac{dR}{dt} \propto \left(\frac{E_0}{\rho_0} \right)^{1/2} R^{-3/2}. \quad (3.2)$$

Separation of variables then gives

$$R \propto \left(\frac{E_0}{\rho_0} \right)^{1/5} t^{2/5}. \quad (3.3)$$

(Wilms, 2018)

Inserting this into the dimensionless variable ξ yields

$$\xi = \beta \left(\frac{E_0}{\rho_0} \right)^{-1/5} r t^{-2/5}, \quad (3.4)$$

where β is a proportionality constant. At the boundary of the shock wave $\xi = 1$ holds. Therefore, the radius of the shock can be written as

$$R_s = \alpha \left(\frac{E_0}{\rho_0} \right)^{1/5} t^{2/5}, \quad (3.5)$$

with $\alpha = 1/\beta$. Using this result, the expansion velocity of the outer blast wave is

$$v_s = \frac{dR_s}{dt} = \alpha \frac{2}{5} \left(\frac{E_0}{\rho_0} \right)^{1/5} t^{-2/5} = \frac{2R_s}{5t} \quad (3.6)$$

(Sasaki, 2019; Vink, 2012).

Truelove & McKee (1999) developed an analytical model to smoothly connect the models of phase I and phase II.

The radiative phase can be described by the “thin shell” model. This model assumes that the whole mass and the kinetic energy of an SNR is concentrated in a thin shell just behind the outer blast wave shock. Contrary, the interior of the remnant is filled with a very hot and thin gas, whose mass is negligible but which contains most of the internal energy of the SNR. The gas in the central region of the remnant is so thin that the cooling time is larger than its age. In this case, the pressure-driven snowplow model holds (Sasaki, 2019). Here, the expansion pressure of the dense and cool shell sustains the pressure of the hot interior (Schaudel, 2003). According to McKee & Ostriker (1977) the radius of the remnant increases as $R_s \propto t^{2/7}$. In the momentum-driven snowplow model, the expanding shell cannot be sustained any longer by the pressure and expands only due to conservation of radial momentum. In this case the radius of the supernova remnant evolves as $R_s \propto t^{1/4}$ (Oort, 1951).

3.4 X-ray emission from Supernova Remnants

3.4.1 Thermal X-ray emission

Shocks created by supernova remnants have two characteristic properties: firstly, they can be assumed to be optically thin, which holds to a very good approximation. Secondly, the ionization distribution of atoms is often out of equilibrium, which is described by the term non-equilibrium ionization (NEI). In general, in coronal plasmas excitations and ionizations are predominantly caused by electrons colliding with ions. Most of the spectral characteristics of thermal emission is determined by the electron temperature, which not necessarily is the same as the ion temperature. Contrary, the most important spectroscopic effect of the ion temperature is thermal line broadening. However, this effect is difficult to measure with the current generation of X-ray spectroscopic instruments (Vink, 2012).

Thermal continuum emission

In general, thermal continuum emission is caused by bremsstrahlung (free-free emission), recombination continuum (free-bound emission), and two-photon emission. The latter is produced by radiative electron transitions from a meta-stable quantum level (Vink, 2012). In particular for metal-rich plasmas in young SNRs free-bound and two-photon emission can be the dominant source of continuum emission (Kaastra et al., 2008).

Bremsstrahlung is a result of the collision of a free electron and an ion. If for the emitted photon energy E holds $E \ll kT$, then the bremsstrahlung spectrum is flat. Whereas, for $E > kT$ it drops exponentially (Kaastra et al., 2008). For solar or sub-solar abundances, the main collision partners of the electrons are protons and helium ions (Vink, 2012).

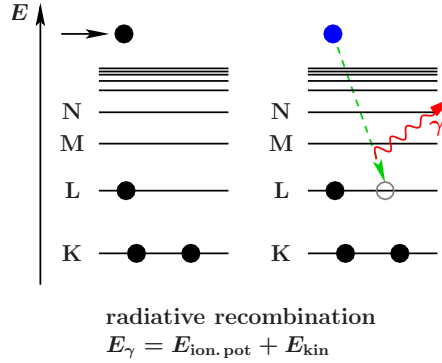


Figure 3.5: Sketch of the process of radiative recombination (taken from Hell, 2017).

The recombination continuum, free-bound emission, occurs during radiative recombination (Kaastra et al., 2008). A sketch that illustrates this process is given in Fig. 3.5. A free electron is captured by an ion releasing a photon with the sum of the kinetic energy of the electron and the binding energy of the recombined ion (Hell, 2017). Free-bound emission shows a sharp edge near series limits since the energy difference for levels with high principal quantum number n is small. In the situation of photo-ionized or overionized plasmas, where $kT \ll h\nu$, free-bound emission results in narrow emission peaks near series limits of lines. These features are called radiative-recombination continua and are for instance observed in mature SNRs (Vink, 2012).

The process of two-photon emission is in particular important for hydrogen- or helium-like ions. If these ions get excited via a collision with a free electron, they can deexcite from this meta-stable state via a second collision with a free electron. For low densities, like in supernova remnants, the probability for collisional deexcitation is low. In this case the deexcitation can happen via two-photon emission (Kaastra et al., 2008).

Non-equilibrium ionization

The simple reason why plasmas of SNRs are often out of ionization equilibrium, in the so called non-equilibrium ionization, is, that not enough time has passed since the plasma was shocked. The densities in supernova remnants are so low that per ion only a few ionizing collisions have occurred since the medium was shocked (Itoh, 1977). The number fraction of atoms in a given ionization state is a differential equation and a function of $n_e t$, with the electron density n_e . The parameter $n_e t$ is also called the ionization age of the plasma. But neither kT_e nor n_e are expected to be constant in time (Vink, 2012).

The main effect of non-equilibrium ionization in young SNRs is that the ionization states at a given temperature are lower than in the collisional ionization equilibrium situation. For temperatures which are relevant for young SNRs ($kT_e = 0.5 - 4$ keV) an ionization time of approximately $n_e t \approx 10^{12} \text{ cm}^{-3} \text{ s}$ is needed to reach collisional ionization equilibrium. In contrast, typical values for SNRs are $n_e t = 10^9 - 5 \times 10^{12} \text{ cm}^{-3} \text{ s}$, meaning that the

plasmas of most supernova remnants are not in collisional ionization equilibrium (Vink, 2012; Seward & Charles, 2010).

Line emission diagnostics

The line emission in supernova remnants results from collisional excitation of ions, which is dominated by collisions between electrons and ions. In this process the excitation happens either directly or through recombination. Due to the low density, it can be assumed that most ions are in the ground state. Additionally, once an excitation occurs, collisional deexcitation or further excitation or ionization can be neglected because of the low density. One result of this is that the ionization balance can be treated independently of the line emission properties (see Mewe, 1999, for a full treatment).

An important aspect of line emission in non-equilibrium plasmas is inner shell ionization. During this process an electron from an inner shell is removed whereas higher level atomic shells are still filled. The result is an ion with a hole in one of the innermost shells. One possibility for this ion to deexcite is to fill the hole and use the energy from that transition for further ionization. These transitions are called Auger transitions and no radiation is emitted. Another possibility to deexcite is via radiation, which is called fluorescence (Vink, 2012).

One important diagnostic tool for the state of the supernova remnant plasma is iron line emission. It allows to draw conclusions about the average electron temperature and the ionization age. For an electron temperature $kT_e \gtrsim 2$ keV, Fe K-shell emission can be observed for all ionization states of iron and its average line energy provides information about the dominant ionization state. In contrast, Fe L-shell emission occurs for lower temperatures. But together, Fe K- and L-shell emission can be used to accurately determine the ionization state of a plasma (Vink, 2012).

Furthermore, $K\alpha$ line emission from low ionization states of iron can be a result of dust grains embedded in hot SNR plasmas (Borkowski & Szymkowiak, 1997). If a hot electron penetrates a dust grain, an inner shell ionization inside the grain can be induced, whereas the emitted photon can escape from small grains. Additionally, nearly neutral iron is slowly released into the hot plasma due to the destruction of dust grains in hot plasmas via dust sputtering. As a result, a broad range of ionization stages of Fe inside the plasma are present (Vink, 2012).

Another line diagnostic tool is given by the triplet line emission from He-like ions. It is available in high resolution spectroscopy ($E/\Delta E \gtrsim 200$) (Vink, 2012) and consists of three prominent lines, which are called resonance, intercombination, and forbidden (see Gabriel & Jordan, 1969; Mewe, 1999; Liedahl, 1999; Porquet et al., 2010). Some ratios between these lines are interesting for studying supernova remnants since they are sensitive to temperature and ionization state of the plasma (Mewe & Schrijver, 1978; Liedahl, 1999; Vink, 2012).

3.4.2 Line emission associated with radioactivity

Line emission in SNRs can not only be caused by collisional processes but also by radioactivity. Radioactive elements can be produced either during the lifetime of the star or during the supernova explosion. The most important radioactive element is ^{56}Ni , which decays in 8.8 days into ^{56}Co , which subsequently decays into ^{56}Fe in 111.3 days (see Diehl

& Timmes, 1998, for a review). This chain is the dominant source of energy for expanding supernova ejecta during the first year after the SN explosion and has also a significant imprint on the lightcurves of supernovae. Furthermore, ^{56}Fe is the most abundant iron isotope in the universe. Type Ia SNe contribute to that by producing typically an amount of $0.6 M_{\odot}$ per explosion (Vink, 2012). In contrast, in core collapse SNe ^{44}Ti is produced with expected yields of $10^{-5} - 10^{-4} M_{\odot}$ (e.g. Prantzos, 2011). This isotope has a decay time of 85 years (Ahmad et al., 2006), which is much longer compared to that of ^{56}Ni . For the supernova remnant phase ^{44}Ti is interesting because of two reasons: firstly, it is sensitive to the expansion speed of the inner layers of the ejecta as its yield is determined by the amount of α -particles left over after the initial stages of explosive nuclear burning (Arnett, 1996; Vink, 2012). Secondly, the isotope is sensitive to the mass cut, which describes the boundary between what is accreted onto the proto-neutron star and what will be ejected, and also to explosion asymmetries (Nagataki et al., 1998).

A direct sign of radioactivity are γ -ray lines associated with their decay (as predicted by Clayton & Silk, 1969). Since daughter products of radioactive elements are usually not in their nuclear ground states, they rapidly deexcite through the emission of γ -ray lines. It might also be that the daughter products have a vacancy in the K-shell, resulting in a K-shell transition, which emits in X-rays (Vink, 2012). These transitions could be detected by future X-ray telescopes such as *ATHENA* (Bookbinder, 2010).

For the investigation of SNRs, the $K\alpha$ line emission of ^{44}Ti and ^{59}Ni is of particular interest since the decay times are compatible with the lifetimes of supernova remnants. K-shell transitions also have the advantage that the spatial resolution of soft X-ray telescopes is in general better than that of hard X-ray or γ -ray telescopes. Nevertheless, it should be noted that these line transitions are not unique. In addition, K-shell transitions are a function of the ionization state of the atom, which complicates matters even more (Vink, 2012).

3.4.3 Non-thermal emission

Non-thermal emission from supernova remnants consists of X-ray synchrotron radiation and non-thermal bremsstrahlung. In principle inverse Compton scattering could be another source of non-thermal radiation, but for SNRs it is only important in the GeV up to TeV γ -ray band (Hinton & Hofmann, 2009). Nevertheless, for magnetic fields inside an SNR it is not expected to be important in the soft X-ray band (Vink, 2012).

X-ray synchrotron radiation

One source of synchrotron radiation are relativistic electrons gyrating in a magnetic field (Ginzburg & Syrovatskij, 1967). In astrophysics, the electron population which is emitting synchrotron radiation mostly is a non-thermal one and can be well approximated by a powerlaw distribution. Synchrotron radiation covers a wide band of frequencies, ranging from radio to X-rays. Most SNRs are radio synchrotron sources, where the synchrotron radiation comes from the remnant's shell. For composite SNRs also embedded pulsar wind nebulae can be the origin of the synchrotron emission. The discovery that X-ray synchrotron radiation is not only emitted by a pulsar wind nebula but also by young SNR shells was made relatively recently (Koyama et al., 1995; Vink, 2012). The first time it was confirmed for the remnant of SN 1006 based on *ASCA* data, which indicated that emission

from the edges of the remnant's shell is dominated by non-thermal emission from electrons accelerated to energies of ~ 100 TeV within the shock front (Koyama et al., 1995).

Considering a relativistic electron with energy E , which moves in a magnetic field with strength B , it will emit synchrotron radiation with a maximum emission at the characteristic frequency ν_{ch} , which is given by

$$\nu_{ch} = 1.8 \times 10^{18} B \left(\frac{E_{\perp}}{1 \text{ erg}} \right)^2 \text{ Hz}, \quad (3.7)$$

$$h\nu_{ch} = 13.9 \left(\frac{B_{\perp}}{100 \mu\text{G}} \right) \left(\frac{E}{100 \text{ TeV}} \right)^2 \text{ keV}, \quad (3.8)$$

where $B_{\perp} \approx \sqrt{2/3}B$ denotes the component of the magnetic field perpendicular to the motion of the electron (Ginzburg & Syrovatskii, 1965). The typical magnetic field strength in supernova remnants ranges between 10 and 500 μG , which means electrons with energies in the range of 10–100 TeV are emitted (Vink, 2012). It is possible that these electrons are responsible for many of the detected TeV γ -ray emission (e.g. Aharonian et al., 2001, 2004). However, it is still under debate which radiation process dominates the TeV emission from SNRs as pion production as well gives rise to TeV γ -ray emission (see Hinton & Hofmann, 2009, for a review).

For relativistic electrons with a powerlaw shaped energy distribution, the spectral index α of the synchrotron flux density spectrum is related to the photon index of the X-ray emission via $\Gamma = \alpha + 1$. Typical photon indices of X-ray synchrotron spectra of young supernova remnants range between 2 and 3.5, which means the slope is rather steep. This is an indication for a rather steep underlying electron energy distribution (Vink, 2012). It can be shown (see Zirakashvili & Aharonian, 2007, for a detailed derivation) that one requirement for X-ray synchrotron radiation is a relatively high shock velocity $\gtrsim 2,000 \text{ km s}^{-1}$. Such high shock velocities are only encountered in young supernova remnants (Vink, 2012).

Non-thermal bremsstrahlung

A second contribution to non-thermal X-ray emission from supernova remnants is non-thermal bremsstrahlung. Bremsstrahlung caused by a population of non-thermal distributed electrons has been considered as a possible source of X-ray continuum emission for almost 30 years (e.g. Asvarov et al., 1990; Vink et al., 1997; Bleeker et al., 2001; Laming, 2001). The electrons that produce X-ray bremsstrahlung have non-relativistic to mildly relativistic energies. Therefore, identifying non-thermal bremsstrahlung would allow to obtain information about the low energy end of the electron cosmic ray distribution. However, the contribution of non-thermal bremsstrahlung is probable not enough to identify it with the current generation of hard X-ray telescopes (Vink, 2012). Since Coulomb interaction between thermal and non-thermal electrons thermalizes the low energy tail of the electrons on relatively short timescales, non-thermal bremsstrahlung can only be expected in a narrow region close to the shock front (Vink, 2008) or for SNRs that have an overall low ionization age like in SNR 1006. But there, the X-ray continuum is overwhelmed by synchrotron radiation. Furthermore, a low ionization age is caused by a low plasma density, which consequently makes the bremsstrahlung emissivity small (Vink, 2012).

3.5 Particle acceleration by Supernova Remnants

SNRs are one candidate source for cosmic rays (Ginzburg & Syrovatskij, 1967) up to energies of 3×10^{15} eV (Blandford & Eichler, 1987; Berezhko & Völk, 2007; Vink, 2012). In particular, they are the only known sources to provide enough power for the Galactic cosmic ray production. Furthermore, non-thermal radio emission from supernova remnants as well as the detection of X-ray synchrotron radiation provide clear evidence for particle acceleration in SNRs (Vink, 2012). Observations tell us that particle acceleration mostly takes place during the early SNR stages, such as the free expansion or the Sedov phase (Helder et al., 2012). The main acceleration process is the so called first order Fermi process, which is also often referred to as diffusive shock acceleration (Axford et al., 1977; Bell, 1978; Blandford & Ostriker, 1978). In this process particles scatter back and forth across the shock front while scattering elastically on either side of the shock due to the presence of a turbulent magnetic field (Vink, 2012; Seward & Charles, 2010). In the course of this process, the particles gain energy with every repetition (Sasaki, 2019; Bell, 1978; Seward & Charles, 2010). There are two requirements for diffuse shock acceleration. Firstly, a strong shock is needed. And secondly, the velocities of particles on either side of the shock are randomized (Bell, 1978). One major uncertainty of diffuse shock acceleration is how charged particles are injected into this process (Vink, 2012).

Recently, in the supernova remnant of the SN 1006 TeV emission has been detected (Acero et al., 2010). For the origin of the γ -ray emission two major scenarios are known. In the leptonic model relativistic electrons interact with low-energy photons, which causes inverse Compton up-scattering of photons. Additionally, bremsstrahlung is emitted by the interaction of the non-thermal electrons with ions in the SNR (Miceli et al., 2012; Sasaki, 2019). The second scenario describes a hadronic model. Here, proton-proton interaction produces neutral π^0 s, which subsequently decay into γ -ray photons (Miceli et al., 2012; Sasaki, 2019). This process is believed to be enhanced in SNRs near high-density clouds, where the probability of colliding protons is higher (Sasaki, 2019). Furthermore, the hadronic scenario would directly prove that SNRs can accelerate cosmic rays up to PeV energies (Miceli et al., 2012).

One way to reveal the presence of particle acceleration in SNRs is to investigate the shock dynamics since the interaction of high-energy particles with the plasma is predicted to increase the shock compression ratio and to decrease the postshock temperature (Berezhko & Ellison, 1999; Decourchelle et al., 2000; Blasi, 2002; Vink et al., 2010). This effect is also known as “shock modification”. For an observational test of these predictions accurate diagnostics of thermal X-ray emission from the shocked ISM is necessary. However, in SNRs with efficient particle acceleration the contribution of the ISM in the X-ray spectra is usually masked out by bright synchrotron emission and by thermal emission from shocked ejecta (Miceli et al., 2012).

4 X-ray telescopes

4.1 Basic principles

In this chapter some basic principles of X-ray telescopes and X-ray detectors will be explained. In addition, two examples of X-ray telescopes are mentioned. The first one is the telescope *XMM-Newton*, which celebrated its 20th anniversary in 2019. In chapter 5 observations of the supernova remnant 1006 taken with *XMM-Newton* are investigated. The second example is *eROSITA*, which was recently launched (July 2019). Simulations for this X-ray telescope are presented in chapter 7 of this thesis. Before showing the examples, the basic principles of X-ray telescopes and detectors are described in the following.

4.1.1 Wolter telescopes

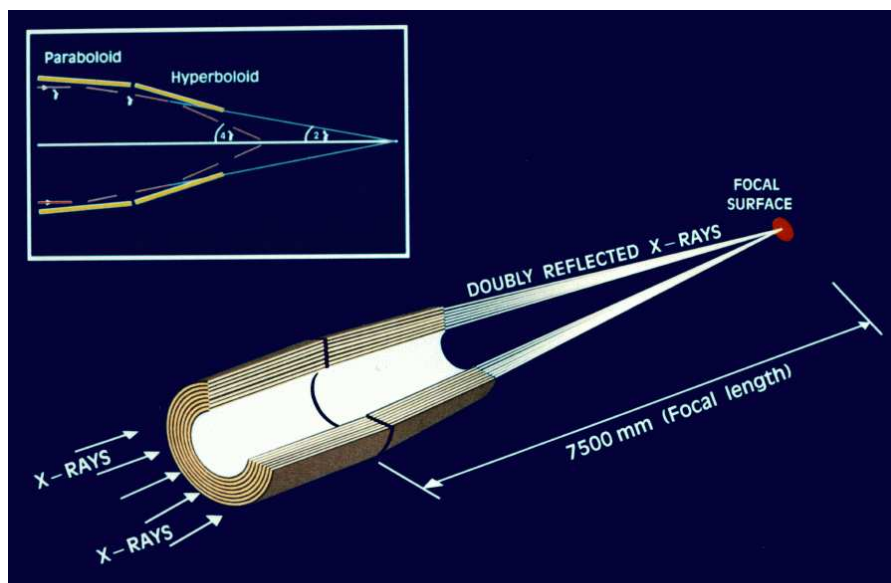


Figure 4.1: Sketch of the light path in *XMM-Newton*'s open X-ray telescope (taken from ESA: *XMM-Newton* SOC, 2019).

The short wavelength of X-ray radiation results in a small critical angle of reflection. The critical angle for X-ray reflection can be described by

$$\theta_c = 5.6' \left(\frac{\rho}{1 \text{ g cm}^{-3}} \right)^{1/2} \frac{\lambda}{1 \text{ nm}}. \quad (4.1)$$

A typical X-ray wavelength is $\lambda \sim 1$ nm, resulting in a critical reflection angle of $\theta_c \sim 1^\circ$. Usually, iridium or gold are chosen for the mirror material due to their density. In order to focus the incoming light to the focal point of the telescope two mirrors are used. Contrary to the case of optical telescopes, where two parabolic mirrors are used, for X-ray wavelength a paraboloid and a hyperboloid are utilized. Mirrors of this type are called Wolter telescopes (Wolter, 1952a,b). The combination of parabolic and hyperbolic mirrors allows to shorten the focal length below ~ 10 m. A small focal length in turn facilitates to launch the telescope on a rocket, which is necessary as Earth's atmosphere is opaque for X-ray radiation. Furthermore, to increase the effective area of the telescope, several mirror shells are nested. A mirror where photons are reflected at small angles is called a "grazing incidence telescope". A sketch of the light path in *XMM-Newton* is shown in Fig. 4.1. Additionally, on the top left corner the arrangement of the two mirrors is depicted. The quality of a telescope is characterized by its sensitivity, its resolution, its effective area, and its efficiency to reject stray light. Stray light is caused by photons from a nearby source, which are scattered singly by the mirrors and reach the camera. One way to reduce stray light is to implement an X-ray baffle in front of the mirrors to shadow the singly reflected photons. The effective area describes the ability of a mirror to collect radiation at different photon energies (ESA: XMM-Newton SOC, 2019).

4.1.2 X-ray CCDs

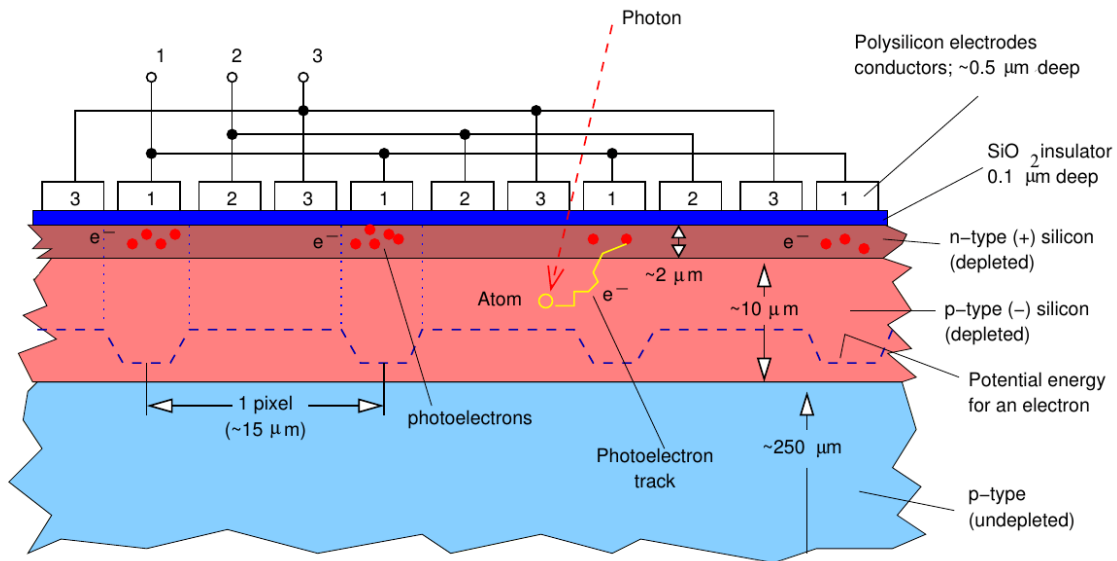


Figure 4.2: Sketch of the structure of an X-ray CCD. An incident X-ray photon excites electrons, which are accumulated in potential wells and read out with three phased pulses (Wilms after Bradt, 2004).

With the use of a Wolter telescope, X-rays coming from an astronomical source are focused onto the focal point of the telescope. The next step in the detection of these photons is to measure the signal via a charge-coupled device, abbreviated with CCD. The working principle of X-ray and optical CCDs is the same. Nevertheless, due to the higher



Figure 4.3: Artist's impression of *XMM-Newton* (Credit: ESA/D. Ducros, taken from <https://sci.esa.int/web/xmm-newton/-/18015-xmm-newton-spacecraft>; accessed on 2019 November 19).

energy of X-ray photons and the resulting larger penetration depths, a larger detector volume is needed. Fig. 4.2 illustrates the basic structure of an X-ray CCD during exposure. CCDs make use of the mechanism of a pn-junction, which means that incident X-ray photons excite electron-hole pairs. The excited electrons are accumulated in potential wells and transferred to the read out via phased pulses. This mechanism allows to determine the individual location and energy of an incoming photon (Krauss, 2016).

4.2 *XMM-Newton*

The *X-ray Multi-Mirror* observatory (*XMM-Newton*) is a cornerstone mission of the European Space Agency's Horizon 2000 programme and was launched on 1999 December 10 (Jansen et al., 2001). An artist's impression of the spacecraft in flight is depicted in Fig. 4.3. The orbit of the *XMM-Newton* spacecraft is highly eccentric with a period of ~ 48 hours (Jansen et al., 2001). A sketch of *XMM-Newton*'s orbit is depicted in Fig. 4.4. The 10 m long spacecraft (Jansen et al., 2001) carries different instruments: two Reflection Grating Spectrometers (RGS; den Herder et al., 2001), the European Photon Imaging Camera (EPIC; consisting of an EPIC PN (Strüder et al., 2001) and two EPIC MOS imaging detectors (Turner et al., 2001)), and an Optical Monitor instrument (OM; Mason et al., 2001). A sketch of the telescope's payload is displayed in Fig. 4.5. The three CCD cameras of the EPIC instrument can be used for X-ray imaging, moderate resolution spectroscopy, and X-ray photometry. The resolving power $E/\Delta E$ ranges between 20 and 50 for the EPIC cameras. The two spectrometers of the RGS instrument are essentially identical and allow high-resolution X-ray spectroscopy and spectro-photometry. Here, the resolving power is on the order of 200–800. Finally, the OM instrument provides optical

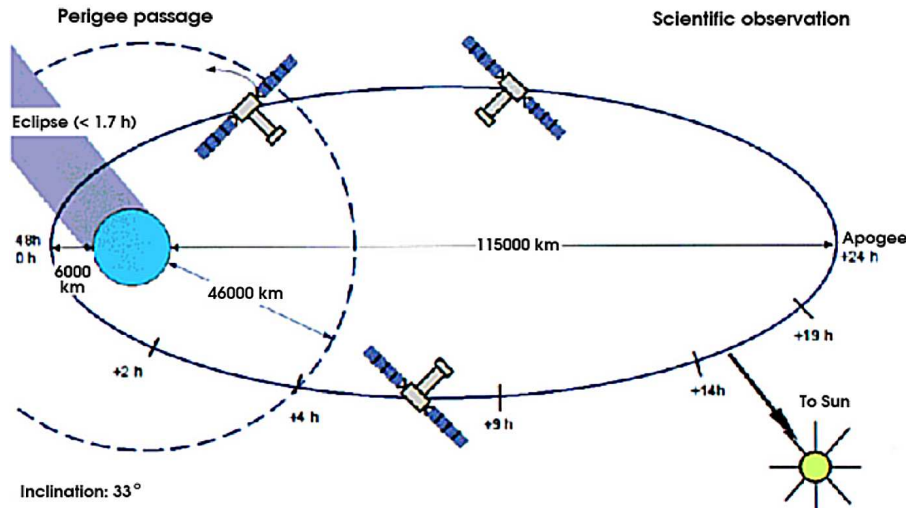


Figure 4.4: Sketch of the highly elliptical *XMM-Newton* orbit (figure courtesy of Dornier Satellitensysteme GmbH; taken from ESA: *XMM-Newton* SOC (2019)).

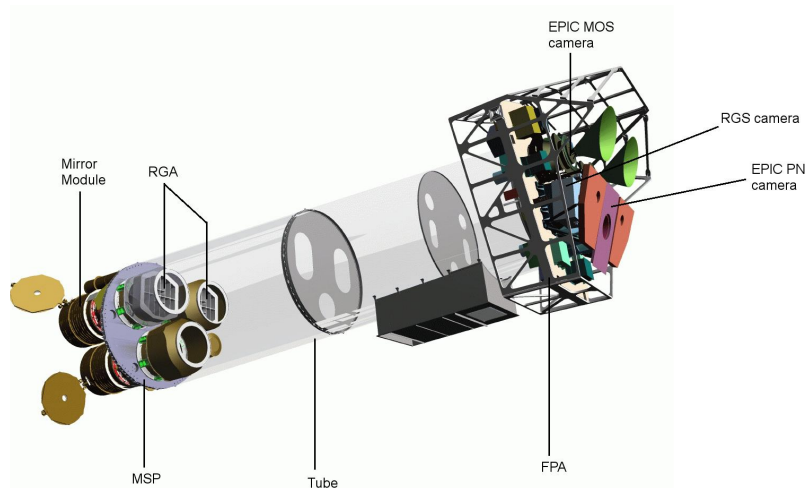


Figure 4.5: Sketch of the *XMM-Newton* payload (figure courtesy of Dornier Satellitensysteme GmbH, modified by Kreikenbohm (2013)).

Table 4.1: Overview of basic characteristics of *XMM-Newton* (taken from ESA: XMM-Newton SOC, 2019).

Instrument	EPIC MOS	EPIC PN	RGS	OM
bandpass	0.15 – 12 keV	0.15 – 12 keV	0.35 – 2.5 keV	180 – 600 nm
sensitivity	$\sim 10^{-14}$ (1)	$\sim 10^{-14}$ (1)	$\sim 8 \times 10^{-5}$ (2)	20.7 mag
FOV	30'	30'	$\sim 5'$	17'
PSF (FWHM/HEW) (3)	5"/14"	6"/15"	N/A	1.4" – 2.0"
pixel size	40 μm	150 μm	81 μm	0.476513"
timing resolution (4)	1.75 ms	0.03 ms	0.6 s	0.5 s
spectral resolution (5)	~ 70 eV	~ 80 eV	0.04/0.025 Å (6)	180 (7)

(1) in units of $\text{erg s}^{-1} \text{cm}^{-2}$ (2) in units of $\text{photons cm}^{-2} \text{s}^{-1}$

(3) PSF: Point-Spread Function, FWHM: Full Width at Half Maximum, HEW: Half Energy Width

(4) in fast data acquisition mode

(5) at 1 keV

(6) in -1^{st} and -2^{nd} order, resp.(7) resolving power ($\lambda/\Delta\lambda$) with UV and optical grism

and UV imaging and grism spectroscopy (ESA: XMM-Newton SOC, 2019). Tab. 4.1 presents an overview of the basic characteristics of the instruments implemented onboard *XMM-Newton*. As can be seen in this table *XMM-Newton* features a high sensitivity and good angular resolution. Furthermore, it allows simultaneous operation of all science instruments (ESA: XMM-Newton SOC, 2019).

The mirrors of the X-ray telescopes consist of gold. In front of the mirror system X-ray baffles are placed, which act as collimators and considerably reduce the amount of stray light in the field of view (FOV) of the focal plane cameras (Jansen et al., 2001). Nevertheless, for bright extended sources, e.g., some supernova remnants, there might be degradation in the ability of performing spatially resolved spectroscopy (ESA: XMM-Newton SOC, 2019).

A further characteristic that influences the quality of an X-ray telescope is its effective area. The effective area of *XMM-Newton*'s X-ray telescopes as a function of the photon energy is plotted in Fig. 4.6. As it is visible from the figure, the EPIC instrument is most efficient in the energy range from 0.1 to 10 keV with a maximum at ~ 1.5 keV. Moreover, there is a pronounced edge near 2 keV, which is related to the Au M edge. As can be seen in Fig. 4.7, the MOS detectors are partially obscured by the RGS' Reflection Grating Assembly. Due to this fact only $\sim 44\%$ of the incoming radiation reaches these cameras, which results in lower effective areas than that of the pn (ESA: XMM-Newton SOC, 2019). For sources, which are not in the center of the FOV but at a certain distance from the center, at the so called off-axis angle, less photons finally reach the focal plane than enter the telescope. This effect is called vignetting and is reflected by a decline of the effective area with increasing off-axis angle (ESA: XMM-Newton SOC, 2019). Another property, which depends on the off-axis angle is the point-spread function (PSF). This property describes how the shape of a point source looks like when being imaged. For *XMM-Newton* the core of the on-axis PSF is narrow and varies only little over a wide energy range from 0.1 to 6 keV (ESA: XMM-Newton SOC, 2019). This means, on-axis

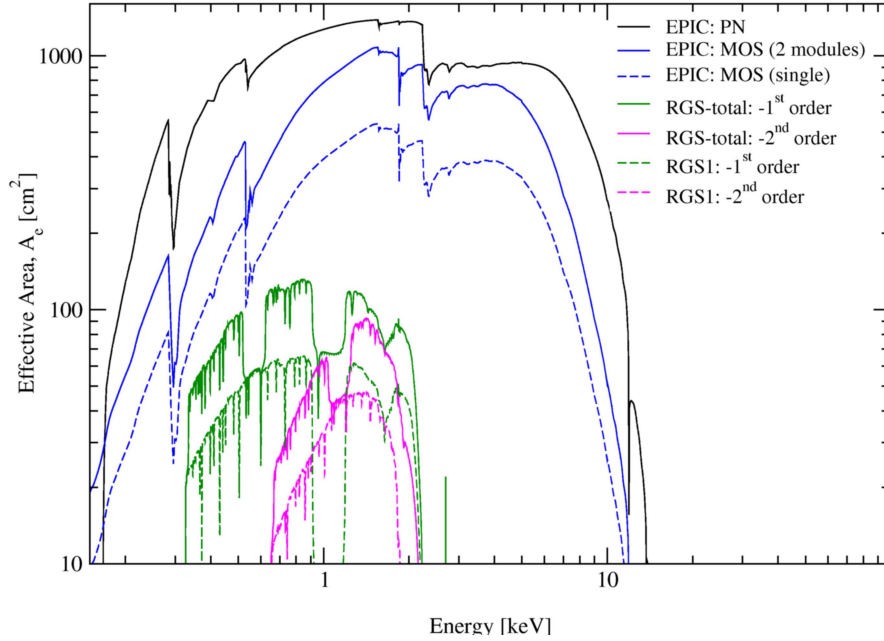


Figure 4.6: Net effective area of *XMM-Newton*'s X-ray telescopes as a function of photon energy in logarithmic scale (taken from ESA: *XMM-Newton* SOC, 2019).

point sources remain point-like. However, with increasing off-axis angle the shape gets more and more elongated.

4.2.1 EPIC

As already mentioned, two of the EPIC instruments onboard *XMM-Newton* comprise MOS-type detectors and one a PN-type detector. The abbreviation MOS stands for Metal Oxide Semiconductor. One MOS detector is made of seven individual, identical, front-illuminated CCD chips, whereas the PN detector consists of a single silicon wafer with twelve back-illuminated CCD chips. The arrangement of the CCD chips can be seen in Fig. 4.8. All EPIC CCDs operate in photon counting mode. Furthermore, there are several data acquisition modes, namely: Full Frame, Extended Full Frame, Large Window, Small Window, Timing, and Burst mode. In addition, since the CCDs are also sensitive to optical, UV, and IR light, aluminised optical blocking filters are implemented. Each detector possesses its own set of filters, consisting of a thick, a medium, and a thin one. Unfortunately, CCD6 and CCD3 of MOS1 were hit by micrometeorites in 2005 and 2012, respectively. After these events, they had to be switched off. Moreover, the impact on CCD3 also affected MOS1 CCD4 by increasing the noise level. Nevertheless, this CCD is still in operation. The angular resolution of MOS and PN is $1.1''$ and $4.1''$, respectively. In general, the readout of PN is much faster than that of MOS (ESA: *XMM-Newton* SOC, 2019).

When investigating extended sources, the background of EPIC is of particular interest. It consists of a cosmic X-ray background and an instrumental background. The instrumental background itself has two components: one detector noise component, which is

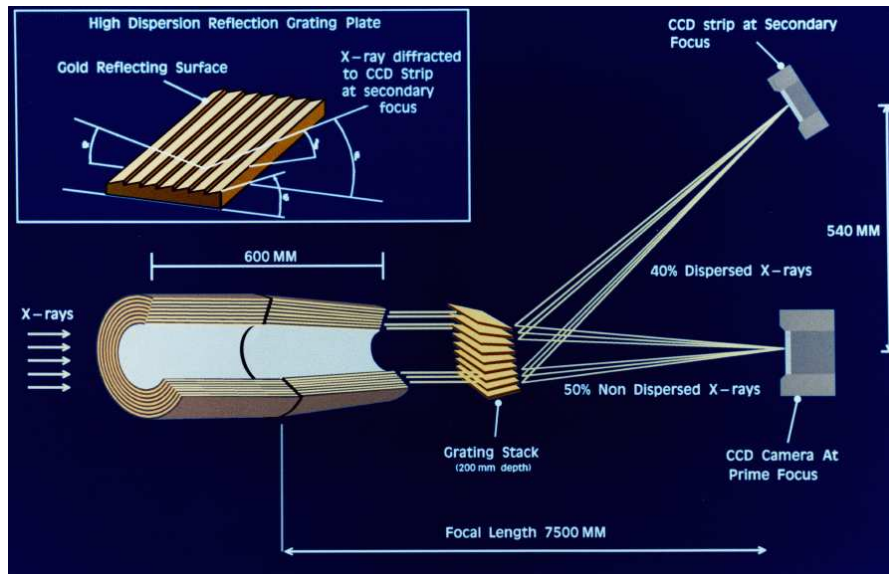


Figure 4.7: Sketch of the light path in the two *XMM-Newton* X-ray telescopes with grating assemblies (taken from ESA: *XMM-Newton* SOC, 2019).

important for energies below 0.3 keV, and a particle induced component. The latter is caused by soft protons and the interaction of high-energy particles, which have an energy higher than some 100 MeV, with the structure surrounding the detectors. Fig. 4.9 displays the detector background for MOS1 and PN. As it is clearly visible there, another important component of the background are fluorescence lines from the detector and the surrounding structure (ESA: *XMM-Newton* SOC, 2019). For a more detailed description of the *XMM-Newton* EPIC background components the reader is referred to Carter & Read (2007).

4.3 The *eROSITA* mission

The name *eROSITA* is an abbreviation for *extended ROentgen Survey with an Imaging Telescope Array* (Merloni et al., 2012). It is one of the newest X-ray telescopes and was launched on 2019 July 13. *eROSITA* was built and is operated by a German consortium led by the Max Planck-Institute for extraterrestrial physics (MPE). It is the main instrument onboard the Russian/German *Spectrum-Roentgen-Gamma (SRG)* mission (Predehl et al., 2006, 2007, 2010, 2016, 2018), which carries the Russian *Astronomical Roentgen Telescope X-ray Concentrator (ART-XC)*; Pavlinsky et al., 2007; Arefiev et al., 2008; Pavlinsky et al., 2011, 2016, 2018) in addition, another imaging X-ray telescope with a harder response than *eROSITA* (Predehl et al., 2018). *eROSITA* is planned to be the successor of the failed *ABRIXAS* (Predehl, 1999) and the canceled *ROSITA* mission (Predehl et al., 2003a,b). The presumed lifetime of the mission is 7.5 years. Approximately the first half year is devoted for reaching its destination at the Lagrangian point L2, performing in-flight calibrations, and a science verification phase. A schematic view of the location of the orbit of *SRG* is shown in Fig. 4.10. At the Lagrangian point L2 the gravitational forces and the orbital motion are balanced. This phase was finished in December 2019. The following

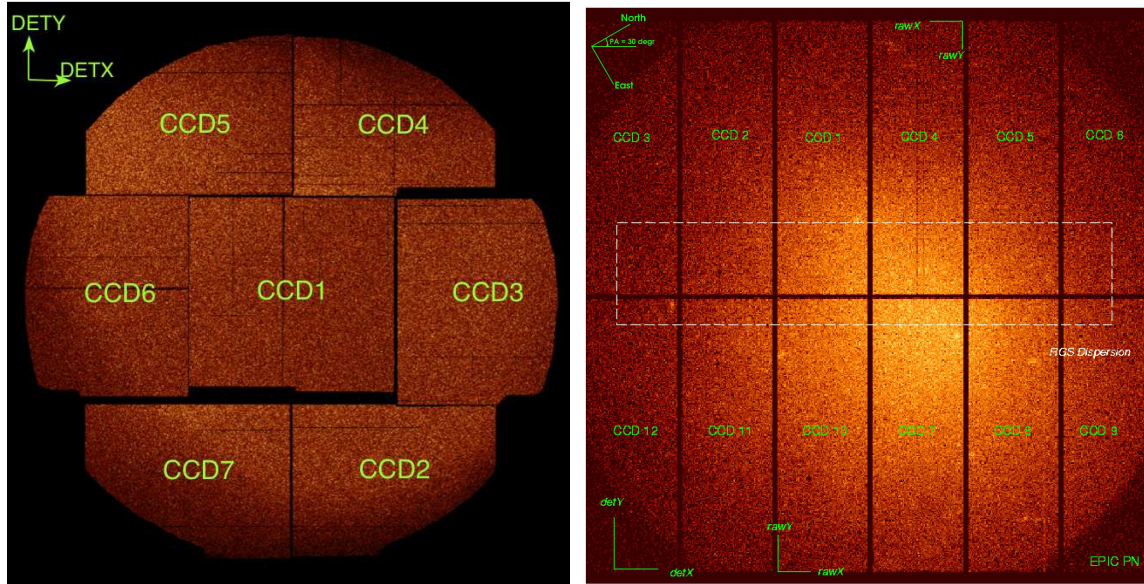


Figure 4.8: Layout of EPIC MOS2 (left) and EPIC PN (right) cameras (taken from ESA: XMM-Newton SOC, 2019).

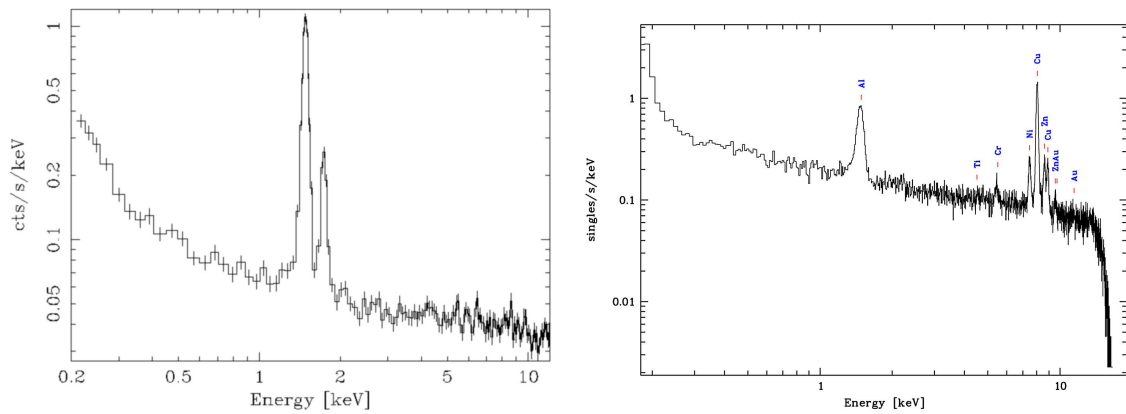


Figure 4.9: Background spectrum for MOS1 (left) and EPIC PN (right) during an observation with the filter wheel in closed position (taken from ESA: XMM-Newton SOC, 2019).

four years will be used to perform a deep survey of the entire X-ray sky. Finally, at least three years of pointed observations are intended (Predehl et al., 2018). *eROSITA* will perform the first X-ray all-sky survey since the *ROSAT* all-sky survey (Voges et al., 1999; Truemper, 1982). In the soft X-ray band (0.5–2.0 keV), *eROSITA*'s all-sky survey will be about 30 times more sensitive than *ROSAT*'s, while in the hard X-ray band (2.0–8.0 keV) it will provide the first ever true imaging survey of the sky (Predehl et al., 2018). The design-driving science of *eROSITA* is to study the large scale structure in the Universe, to test and characterize cosmological models including Dark Energy by detecting very large samples of galaxy clusters out to redshifts $z > 1$. Furthermore, the mission will provide insights in a wide range of astrophysical phenomena, including Active Galactic Nuclei (AGN), supermassive black holes, accreting binaries, active stars, and diffuse emission within our Galaxy (Merloni et al., 2012). Additionally, the survey allows to study time variability of different sources.

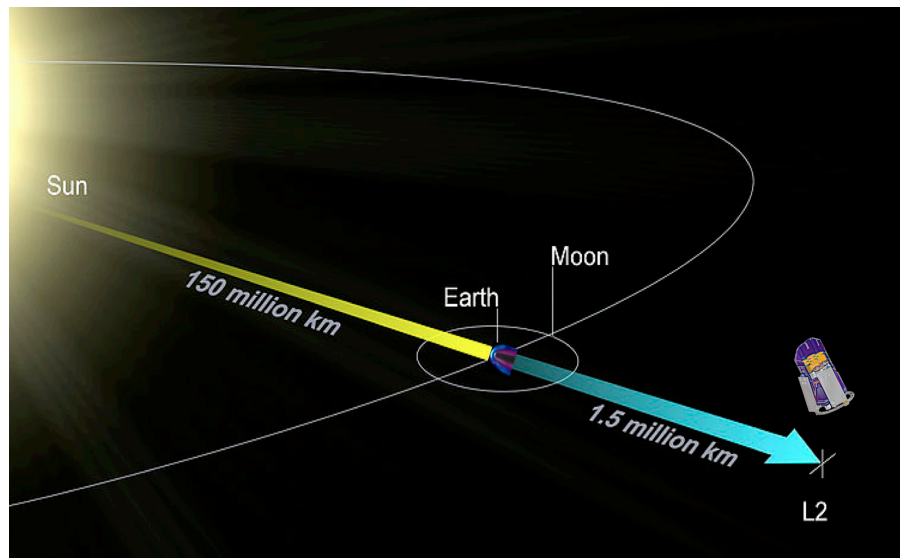


Figure 4.10: Schematic view of the location of the Lagrangian point L_2 orbit of SRG (composite image courtesy of K. Dennerl; taken from Merloni et al. (2012)).

4.3.1 Technical characteristics

A schematic view of *eROSITA*'s telescope structure is depicted in Fig. 4.11. The most important technical characteristics are summarized in Tab. 4.2. The X-ray telescope consists of seven identical mirror modules (Friedrich et al., 2008; Burwitz et al., 2014) with co-aligned optical axes. Each of them is made up by 54 nickel mirror shells coated with gold and carries an X-ray baffle (Friedrich et al., 2014) in front. The advantages of a multiple mirror system in contrast to a large single mirror system are mainly a shorter focal length, which reduces the instrumental background, and a reduced pileup when observing bright sources (Merloni et al., 2012). Pileup is defined as the arrival of more than one X-ray photon in one camera pixel or in adjacent pixels before it is read out (ESA: XMM-Newton SOC, 2019). During launch the front cover was closed (Merloni et al., 2012).

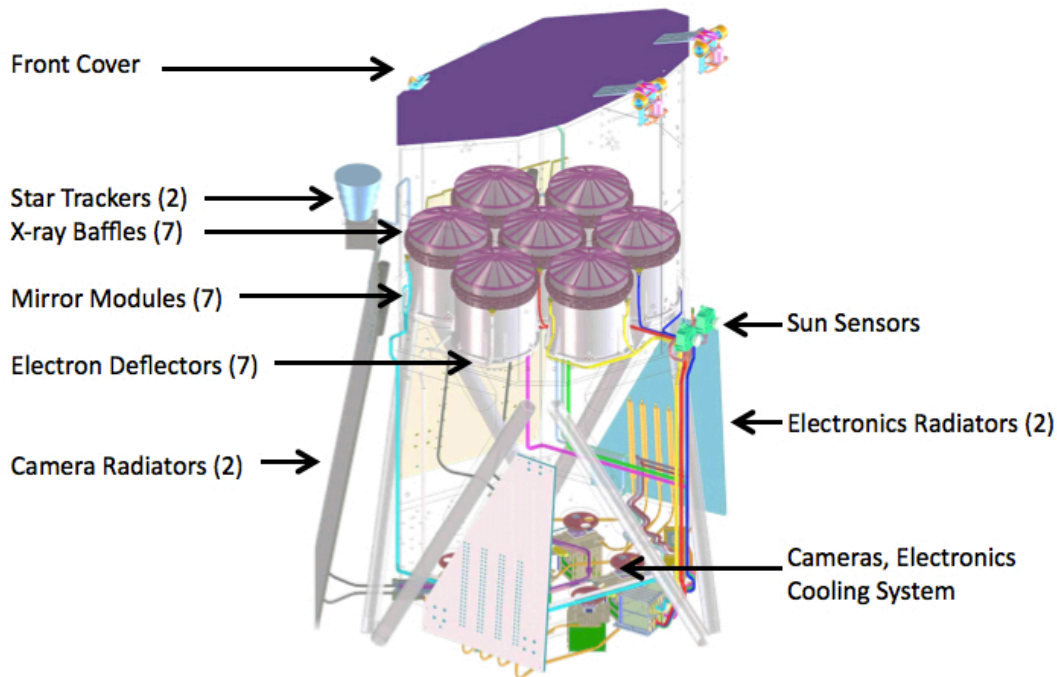


Figure 4.11: Schematic diagram of the *eROSITA* telescope structure (taken from Merloni et al., 2012).

***eROSITA* cameras**

Compared to the *XMM-Newton* PN-CCD (Strüder et al., 2001) there are improvements for the *eROSITA* cameras (Meidinger et al., 2008, 2011, 2014). For instance, the CCD has been extended by a frame store area in order to reduce out-of-time events (Meidinger et al., 2011). Out-of-time events are photons registered during the readout. Therefore, wrong detector positions are assigned to these events (ESA: *XMM-Newton* SOC, 2019). The *eROSITA* CCD has 384×384 pixels, which corresponds to an image area of $28.8 \text{ mm} \times 28.8 \text{ mm}$ or a field of view of 1.03° diameter. The nominal integration time is 50 ms. The CCDs are shielded against particle radiation by a massive copper housing surrounding the entire CCD module. All CCD modules are cooled down to about -90° C (Merloni et al., 2012).

4.3.2 Survey strategy

During its all-sky survey phase *eROSITA* will perform one complete scan of the celestial sphere every half year, resulting in eight scans of the sky in the four years planned for the survey (Merloni et al., 2012). Fig. 4.12 visualizes the observing strategy. The scans of the celestial sphere are performed in approximate great circles. One circle takes four hours and is called an eroday. Due to the motion of the satellite around the sun, the plane of the scans advances, leading to a full coverage of the entire sky in six months. For a rotation axis facing directly towards the sun, the exposure is distributed relatively uniform over the whole sky with the exception of the ecliptic poles. These regions are deeply exposed

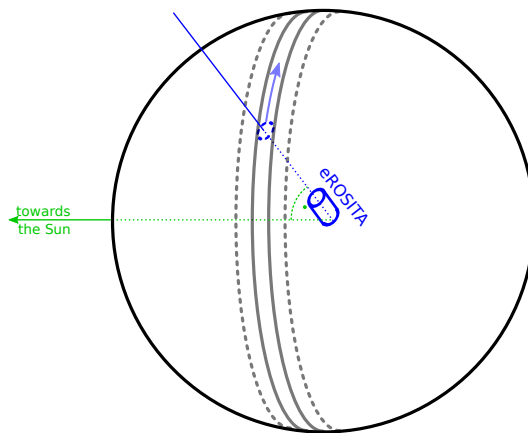


Figure 4.12: During the all-sky survey phase *eROSITA* scans the celestial sphere in approximate great circles. As the scan axis is facing the sun the great scanning circles are precessing. And due to the motion of the satellite around the sun the entire sky is covered once in a half year (taken from Schmid, 2012).

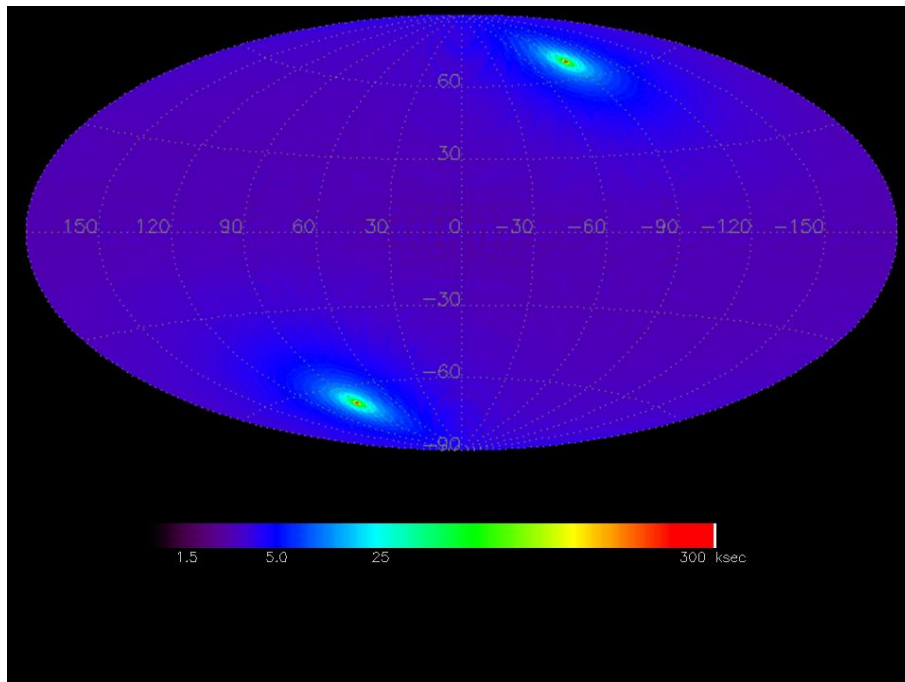


Figure 4.13: Exposure map after the four years of *eROSITA*'s all-sky survey in equatorial coordinates (taken from <http://www.mpe.mpg.de/455799/instrument>; accessed on 2020 January 27). Brighter pixels symbolize higher exposure time.

Table 4.2: Summary of the technical details of *eROSITA* (Merloni et al., 2012; Meidinger et al., 2011, 2014)

attribute	value
mirror modules	7
mirror shells per module	54
energy range	0.2 – 10 keV
outer diameter	358 mm
angular resolution (at 1.5 keV)	< 15'' on axis
energy resolution (at 1.5 keV)	~ 80 eV
CCD size	384 × 384 pixels
CCD pixel size	75 μm
nominal integration time	50 ms
focal length	1.6 m
FOV	1.03° diameter

because the great scanning circles overlap there. An average exposure time of about 2.5 ks is reached (Merloni et al., 2012). In the case of *eROSITA* the satellite's rotation axis has a small tilt with respect to the direction towards the sun. This allows to create larger areas with deep exposure close to the ecliptic poles (Predehl, 2017). A simulated exposure map after the four years of all-sky survey is depicted in Fig. 4.13. Due to the survey strategy time variability on timescales of few hours up to months can be investigated. This allows to constrain the nature of certain variable phenomena, e.g., tidal disruption events. The all-sky survey data will be split equally between the German and Russian consortia via splitting the celestial sphere through the Galactic center and the Galactic poles into two hemispheres (Merloni et al., 2012). This scheme guarantees a fair share of both the Galactic and extragalactic areas (Predehl, 2017).

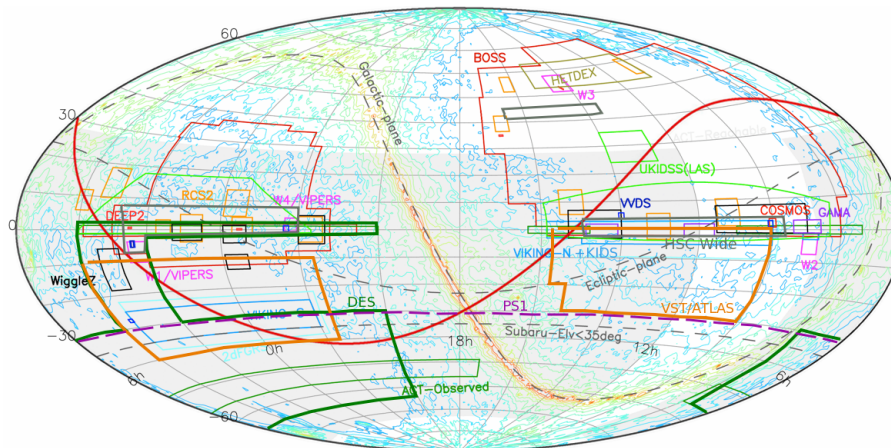


Figure 4.14: Scheme of the entire sky in equatorial coordinates. The thick red line symbolizes the separation line between the German and the Russian *eROSITA* sky. The southern one is the German part (figure courtesy of A. Nishizawa, IPMU; taken from Merloni et al. (2012)).

5 *XMM-Newton* data analysis of the Galactic SNR 1006

5.1 Description of SNR 1006

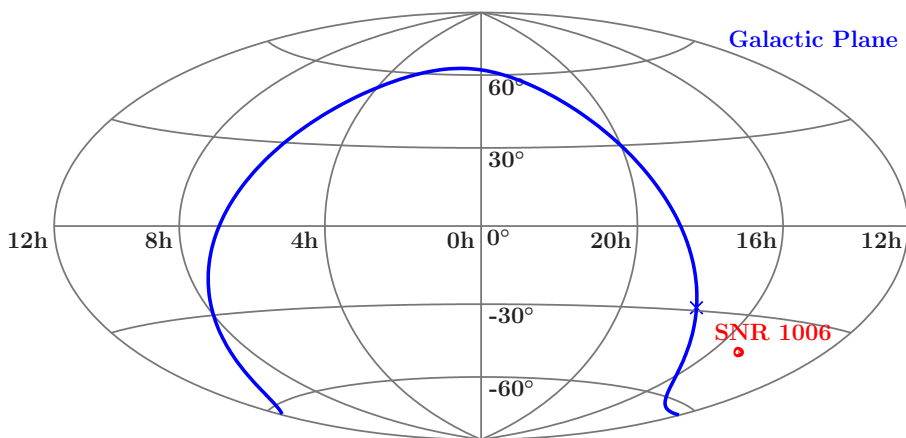


Figure 5.1: Location of SNR 1006 on the sky in an equatorial coordinate system. In addition, the Galactic plane is shown in blue.

This thesis is concentrated on the supernova remnant (SNR) 1006, which is located in the stellar constellation Lupus at a right ascension of $15^{\text{h}} 02^{\text{m}} 22.1^{\text{s}}$ and a declination of $-42^{\circ} 05' 49''$ ¹. Its position is also visualized in Fig. 5.1. The distance to SNR 1006 was determined to (2.17 ± 0.08) kpc (Long et al., 2003). It is almost circular and with a diameter of $30'$ SNR 1006 has a similar size as the full moon. The physical radius is 9.5 pc (Long et al., 2003). The supernova from which the remnant originates was observed in the year 1006 AD and can be found in, for instance, Chinese and Arabic records from that time. During daylight it was probably visible for three months and for three years also during the night with the naked eye. SN 1006 was a thermonuclear supernova of Type Ia (Seward & Charles, 2010). Its remnant was first identified through its radio emission (Gardner & Milne, 1965). A few years later, X-ray emission was detected (Winkler & Laird, 1976), followed by the observation of faint optical filaments (van den Bergh, 1976).

SNR 1006 exhibits two opposed radio, X-ray, and γ -ray bright limbs dominated by non-thermal emission, separated by an inner region of low surface brightness and soft, thermal X-ray emission (Miceli et al., 2012). Therefore, it can be categorized as a shell-type SNR. Since the northeast and southwest limbs are significantly brighter than the northwest and southeast area, SNR 1006 is often classified as a bipolar or barrel-shaped supernova

¹<http://simbad.u-strasbg.fr/simbad/sim-basic?Ident=Sn+1006&submit=SIMBAD+search> (accessed on 2020 February 1)

remnant (Long et al., 2003). The fact that SNR 1006 is almost circular can be explained by its location above the Galactic plane in a relatively homogeneous environment, in which the spherical geometry of a point explosion can be maintained (Acero et al., 2010). Because of its age, SNR 1006 is expected to be in the Sedov phase of its evolution or at least in a transition to this phase (Long et al., 2003).

Thermal X-ray emission has been associated with shocked ejecta from the supernova explosion (Acero et al., 2007; Miceli et al., 2009). But also a component from the shocked ISM is possible (Miceli et al., 2012). Thermal emission is expected since the initial kinetic energy of the ejecta is gradually converted into heat as the blast wave is slowed down by the interstellar medium (Willingale et al., 1996). In addition, an iron overabundance has been revealed in the interior of the remnant (Yamaguchi et al., 2008). The non-thermal emitting limbs of SNR 1006 are indicative of synchrotron emission from high-energy electrons, which was observed for the first time in an SNR in X-rays (Koyama et al., 1995). The possibility of this kind of emission was mentioned about 15 years earlier by Becker et al. (1980). Therefore, particle acceleration is more efficient in these non-thermal limbs (Miceli et al., 2012). According to Miceli et al. (2009), the emission at the rim of the shell can be described by a mixture of thermal emission from plasma in non-equilibrium of ionization and non-thermal emission.

Why was this source chosen to play a main role in this thesis? First of all, so far, extended sources have not been considered in detail when making predictions for the *eROSITA* mission. Because of that, this thesis will provide first insights in the visibility of SNRs by *eROSITA* during its all-sky survey phase. This answers the question of why the investigation of a supernova remnant was chosen in the prospect of the *eROSITA* mission. The question of why specifically the SNR 1006 was chosen, can be addressed on one hand by its position on the sky. It is located above the Galactic plane in a region, which is part of the sky area, for which the German consortium of the *eROSITA* mission will obtain data. In addition, due to its location in a relatively clean environment it is possible to derive an undisturbed description of a supernova remnant, which would be quite difficult by investigating a supernova remnant, for instance, in the Large Magellanic Cloud (LMC). Last but not least, the spectrum of SNR 1006 is harder than that of a typical SNR and allows to predict the expected counts for non-thermal SNRs, which will be detected with *eROSITA*.

5.2 Observational details

In this thesis *XMM-Newton* observations of SNR 1006 have been analyzed. The observations with ID 0555630101, 0555631001, and 0653860101 are used for spectral modelling. These were taken on 2008 August 22, 2008 August 28, and 2010 August 28 with exposure times of 46 ks, 66 ks, and 130 ks, respectively. These observations only cover the south of the supernova remnant. Therefore, two more observations were used to create a mosaic image of the full remnant. The corresponding observation IDs are 0077340101 and 0143980201. These observations were taken on 2001 August 10 and 2003 August 14 with durations of 66 ks and 31 ks, respectively. Tab. 5.1 summarizes the considered observations. All observations were taken in full frame mode with the medium filter.

Table 5.1: Details of the considered *XMM-Newton* observations of SNR 1006 for the spectral analysis and the creation of a mosaic image of the remnant.

obsID	date	duration [ks]	used for spectral analysis
0555630101	2008 August 22	46	yes
0555631001	2008 August 28	66	yes
0653860101	2010 August 28	130	yes
0077340101	2001 August 10	66	no
0143980201	2003 August 14	31	no

5.3 Data reduction

The data were reduced following the *XMM* ESAS Cookbook², which provides a standard guideline for the reduction of data of extended sources using the *XMM-Newton* Extended Source Analysis Software (ESAS). Only the basic steps are described here. For the extraction of the data the XMM SAS version 16.0.0 was used. Important to note is that the Observation Data Files (ODF) contain uncalibrated science files. The task `odfingest` produces a detailed ASCII summary file, which, amongst others, includes a description of the instrumental configuration. Moreover, the Current Calibration File (CCF) contains calibration data and the Calibration Index File (CIF) enables the access to the calibration files (ESA: *XMM-Newton* SOC, 2019). After setting up the analysis directory filtered event files are created with the help of the ESAS tasks `epchain`, `pn-filter`, `emchain`, and `mos-filter`. For these files soft proton flares are also filtered out. Furthermore, CCDs in an anomalous state like CCD6 of MOS1 after the strike of a micrometeorite in 2005³ were excluded from further processing. Afterwards, point sources are detected and excised with the task `cheese` with the default parameters, i.e., a PSF threshold to which the point sources are masked of 0.25. This means that a point source is removed down to a level at which the surface brightness of the point source is one quarter of the surrounding background. In addition, a point source flux threshold of 1.0×10^{-14} ergs cm⁻² s⁻¹ and a minimal separation of point sources of 40.0 arcsec is set. In a next step, model particle background spectra and images are created. This is done via `mos-spectra` and `pn-spectra` and taking into account the filtered source exclusion regions, which were produced in the previous step. Next, quiescent particle background (QPB) spectra and images are produced using `mos_back` and `pn_back`. Afterwards, the spectra are rebinned to a minimum of 50 counts per channel via `grppha`. Before images can be created finally, it is necessary to recast the produced particle background images from detector coordinates into sky coordinates with the help of the task `rot-im-det-sky`. Although the data were already filtered for soft proton flares, it is possible that some residual soft proton contamination is left. In order to determine its level, a broken powerlaw which is not folded through the instrumental effective areas is added to the spectral fit model. Additionally, since the solid angle of the single detectors is not the same, a scaling factor needs to be introduced. This scaling factor can be determined with the task `proton_scale`,

²<https://heasarc.gsfc.nasa.gov/docs/xmm/esas/cookbook/xmm-esas.html> (accessed on 2020 January 27)

³https://xmm-tools.cosmos.esa.int/external/xmm_user_support/documentation/uhb/epic.html (accessed on 2020 January 27)

which returns a backscale factor, the area, an average flux, and the scaled average flux for each detector. Now an image of the soft proton background can be produced by the task `proton`. For this task the normalization and the indices of the additional broken powerlaws need to be stated. The resulting images are also recasted from detector to sky coordinates. Since no bright source is located nearby, there is no stray light and therefore no correction needs to be applied. With the images of the quiescent particle background and of the soft proton background, all components for a background-subtracted and exposure-corrected image are ready. But before creating a background-subtracted and exposure-corrected image, it is reasonable to combine the MOS1, MOS2, and PN data with `comb`, which adds the individual components from the three instruments with proper scalings for different filters and different instruments. Since typically the counts in an image are too few, the image is smoothed with the adaptive filter task `adapt`, which produces a reasonable background-subtracted and exposure-corrected image. Here, it is done with a smoothing kernel of 50 counts, a threshold for excluding low exposure regions of 0.02, and a binning of 2. If one uses the images of different observations, a mosaic image can be created. Fig. 5.2 shows such a mosaic image of SNR 1006 for the used 5 observations. Furthermore, three different energy bands – soft, intermediate, and hard – are color coded in red, green, and blue.

5.4 Sources of background contamination

As a supernova remnant is an extended source with relatively low surface brightness, it is necessary to not only model the source spectrum but also to have a good knowledge of the background. A way to do this is also explained in the *XMM* ESAS Cookbook. First of all, the instrumental background needs to be modeled. For example the AlK_α and the SiK_α lines for both MOS detectors and the AlK_α and the CuK_α lines for the PN need to be modeled. Altogether, the detector lines can be modeled by two Gaussian lines located at an energy of 1.49 keV and 1.75 keV for the MOS detectors, and six Gaussian lines located at 1.49 keV, 7.49 keV, 7.11 keV, 8.05 keV, 8.62 keV, and 8.90 keV for PN. Further instrumental background which is caused by soft protons is already corrected by separate model components with diagonal unitary matrices. For simplicity, contrary to the case of creating images, for spectral modelling a powerlaw is chosen to model the soft proton contamination instead of a broken powerlaw model.

Another source of contamination is given by the cosmic background. This kind is a significant background in all directions of the sky and at all energies, which varies both in intensity and spectral shape over the sky. According to the *XMM* ESAS Cookbook, the cosmic background can usually be modeled by four components. The first one represents the emission from the Local Hot Bubble or heliosphere and is given by a cool ($E \sim 0.1$ keV), unabsorbed thermal component (`appec`). Another cool ($E \sim 0.1$ keV), but absorbed thermal component describes the emission from the cooler Galactic halo. The third component represents the emission from the hotter halo and/or intergalactic medium. It is given by an absorbed thermal component with a higher temperature ($E \sim 0.25 - 0.7$ keV). The fourth and final component is an absorbed powerlaw with a photon index of 1.46, representing the unresolved background of cosmological sources. Therefore the resulting spectral model for the cosmic background is `appec + (appec + appec + powerlaw) · tbabs`. The `appec` model

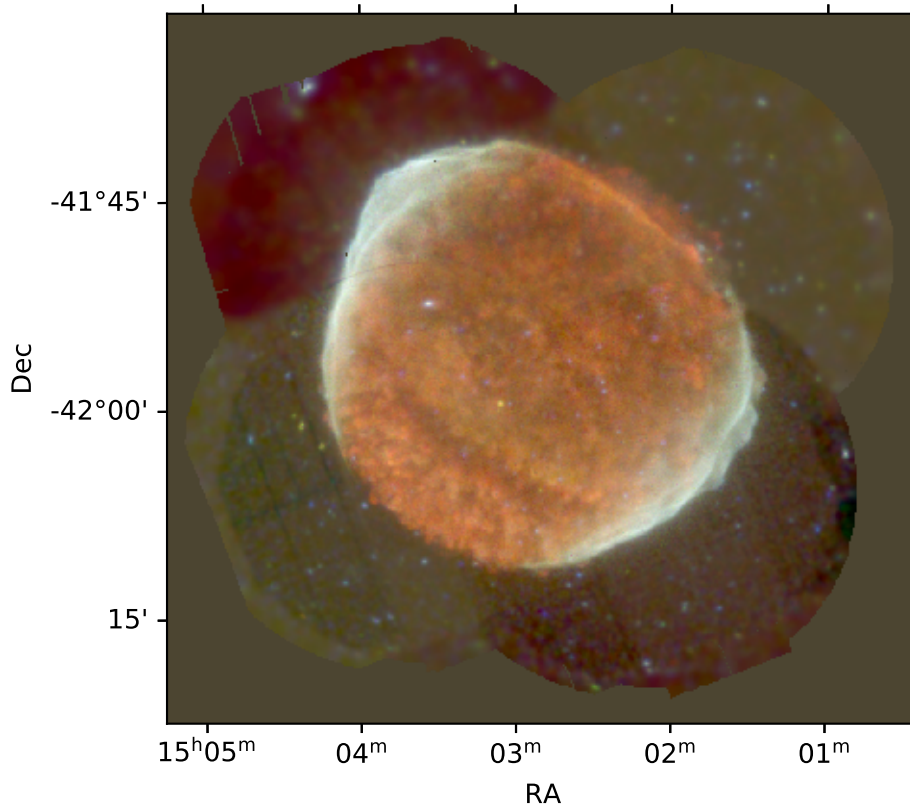


Figure 5.2: RGB composite image of 5 *XMM-Newton* observations of SNR 1006. The red channel is assigned to the energy band 0.3–0.8 keV, green to 0.8–2.0 keV, and blue to 2.0–4.5 keV.

describes an emission spectrum from collisionally-ionized plasma in thermal equilibrium⁴. `tbabs` is a Tuebingen-Boulder ISM absorption model, which describes the gas-phase ISM, the grain-phase ISM, as well as the molecules in the ISM⁵.

A third source of contamination originates in the solar system and in the near-Earth environment, the so called solar wind charge exchange (SWCX). This phenomenon occurs when ions interact with neutral atoms or molecules. During the interaction one or more electrons are transferred to the ion into an excited state. In the subsequent relaxation of the ion, a cascade of photons may be emitted. The ions present in the solar wind are highly-charged oxygen, carbon, and neon. These result in emission of X-rays⁶.

⁴<https://heasarc.gsfc.nasa.gov/xanadu/xspec/xspec11/manual/node39.html#apec> (accessed on 2020 January 27)

⁵<https://heasarc.gsfc.nasa.gov/xanadu/xspec/xspec11/manual/node42.html#tbabs> (accessed on 2020 January 27)

⁶<https://www2.le.ac.uk/departments/physics/research/xroa/astrophysics-1/SWCX> (accessed on 2020 January 27)

5.5 Region definition

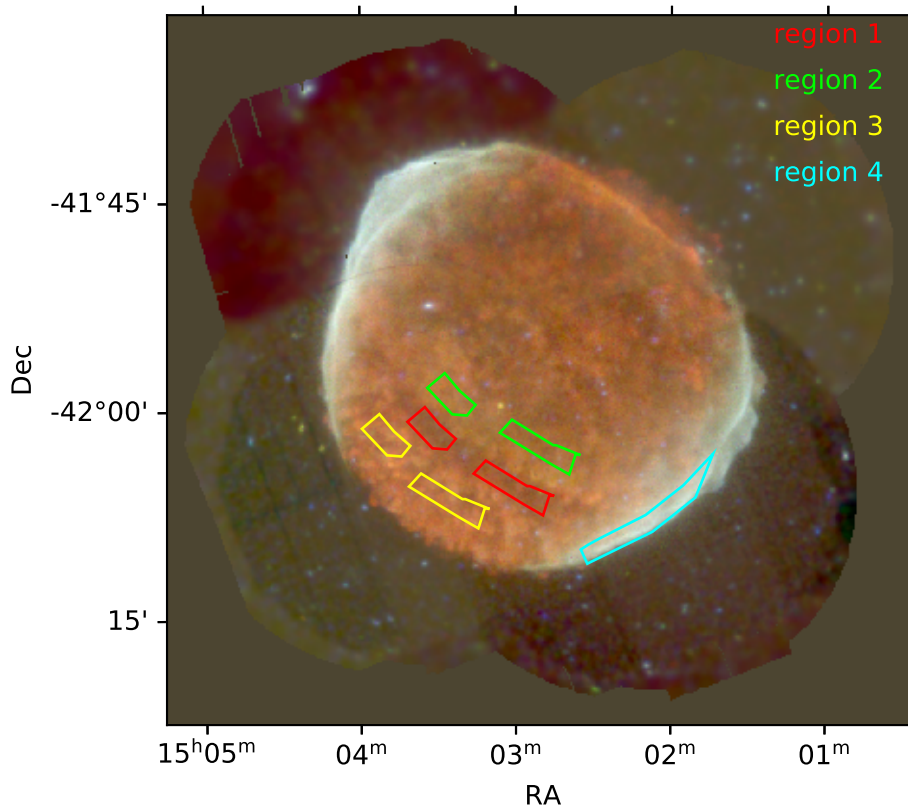


Figure 5.3: RGB composite image of 5 *XMM-Newton* observations of SNR 1006 like in Fig. 5.2. Here additionally the four used regions for spectral modelling are plotted in different colors.

Looking at the image of SNR 1006, which can be seen in Fig. 5.2, it seems that the southwestern and the northeastern rims of the remnant are dominated by hard X-rays, whereas the interior is dominated by soft X-rays. Therefore, for modelling the spectrum of the remnant a hard and a soft component is necessary. The hard component can be determined using a region covering the southwestern rim of SNR 1006, corresponding to region 4 in Fig. 5.3. This region was observed in 2010 (obsID 0653860101). Region 1, shown in red in Fig. 5.3, also seems interesting since it is darker than its surroundings. Since there is a hard X-ray source located in the middle of the dark area, region 1 is splitted into two regions. In order to test if the darker area is caused by higher absorption, two more regions were chosen, one located above and one below region 1. Both of these regions have the same size as region 1 but are shifted in order to stay inside the detector area of the two observations in 2008 (obsID 0555630101 and 0555631001).

5.6 Spectral modelling

For spectral analyses throughout this thesis the X-ray Spectral Fitting Package XSPEC (Arnaud, 1996) was used in the version 12.11.0.

A first attempt was to use the fit model of Miceli et al. (2012) to model the *XMM-Newton* data of SNR 1006. In their paper they use one `vpshock` component for the ejecta, another one with solar abundances to describe the ISM, and a non-thermal emission given by `srcut`. The `vpshock` model (Borkowski et al., 2001) describes an isothermal and optically thin plasma in non-equilibrium of ionization with a linear distribution of ionization timescale versus emission measure (Miceli et al., 2012). The `srcut` model (Reynolds & Keohane, 1999) describes a synchrotron spectrum from electrons with a distribution described by a powerlaw with an exponential cut-off in a homogeneous magnetic field⁷. The same parameters as in Miceli et al. (2012) were fixed. In order to account for the remaining proton contamination, a powerlaw, which is not folded through the instrumental effective area, is added to the fit model. The data were fitted in the energy range between 0.3 keV and 7.0 keV. Nevertheless, the fit result was not convincing. A reason for that could be that Miceli et al. (2012) used different regions, mainly located at the southeastern rim of the remnant.

Therefore, the fit models were switched to the model `vnei` for the thermal components and `powerlaw` for the non-thermal emission. The `vnei` model is a non-equilibrium ionization collisional plasma model. It assumes a constant temperature and single ionization parameter⁸. Furthermore, only one thermal component was considered. Fitting two thermal components with the element abundances of one of them set to solar values, showed that the second component does not contribute much to the spectrum and therefore, was removed.

Instead of analyzing PN and MOS spectra simultaneously, only the PN spectra were considered. A reason for this is the different behavior of the EPIC PN and the EPIC MOS instruments. Due to the higher effective area of PN than MOS (as can be seen in Fig. 4.6), the measured intensity of radiation is higher for the PN detector. In order to avoid difficulties with different normalizations and different instrumental lines, only the PN data were analyzed as they exhibit the best statistics. Since the regions 1, 2, and 3 were covered in two observations, for these regions the PN spectra of both observations were fitted simultaneously. Contrary, region 4 is only included in one observation, therefore only one PN spectrum was fitted.

The considered energy range is 0.3–10.0 keV for all spectra and regions. Also for the source model absorption has to be taken into account, for which we used the `tbabs` Tuebingen-Boulder absorption model. The best fit parameters for the thermal and non-thermal components as well as the absorption for all four regions can be found in Tab. 5.2. The table also shows the reduced χ^2 value of the fit as well as the degrees of freedom (DoF). The spectra of all four regions, which were binned to a minimum of 50 counts per channel, together with the best-fit models are presented in Fig. 5.4 and Fig. 5.5.

First, the spectrum of region 4 was fitted in order to determine the photon index of the `powerlaw`, which should be frozen to this value for the other regions. This results from

⁷<https://heasarc.gsfc.nasa.gov/xanadu/xspec/xspec11/manual/node40.html#srcut> (accessed on 2020 January 27)

⁸<https://heasarc.gsfc.nasa.gov/xanadu/xspec/xspec11/manual/node40.html#vnei> (accessed on 2020 January 27)

Table 5.2: Best fit parameters for all four regions considered in the XMM-Newton data analysis of SNR 1006. The Gaussian line is for modelling a solar wind charge exchange line. The absorbed flux values are given in the energy range 0.3–10.0 keV.

parameter	region 1	region 2	region 3	region 4
tfabs.nH [10^{22} cm $^{-2}$]	$0.34^{+0.04}_{-0.04}$	$0.60^{+0.05}_{-0.018}$	$0.24^{+0.03}_{-0.06}$	$0.115^{+0.003}_{-0.003}$
vnei.kT [keV]	$0.45^{+0.04}_{-0.05}$	$0.74^{+0.09}_{-0.18}$	$0.6^{+0.20}_{-0.09}$	$0.293^{+0.010}_{-0.007}$
vnei.H [solar]	1.0 (frozen)	1.0 (frozen)	1.0 (frozen)	1.0 (frozen)
vnei.He [solar]	1.0 (frozen)	1.0 (frozen)	1.0 (frozen)	1.0 (frozen)
vnei.C [solar]	1.0 (frozen)	1.0 (frozen)	1.0 (frozen)	1.0 (frozen)
vnei.N [solar]	1.0 (frozen)	1.0 (frozen)	1.0 (frozen)	1.0 (frozen)
vnei.O [solar]	$3.0^{+0.4}_{-0.3}$	$6.2^{+0.8}_{-0.6}$	$4.0^{+0.7}_{-0.5}$	1.0 (frozen)
vnei.Ne [solar]	1.0 (frozen)	1.0 (frozen)	1.0 (frozen)	1.0 (frozen)
vnei.Mg [solar]	$2.0^{+0.5}_{-0.5}$	$3.0^{+0.3}_{-0.3}$	$9.4^{+2.2}_{-2.3}$	1.0 (frozen)
vnei.Si [solar]	$54.5^{+17.5}_{-11.2}$	$27.7^{+18.9}_{-2.0}$	$96.8^{+30.9}_{-30}$	1.0 (frozen)
vnei.S [solar]	$273.9^{+94.4}_{-80.7}$	$37.5^{+58.8}_{-10.7}$	$187.1^{+84.7}_{-51.6}$	1.0 (frozen)
vnei.Ar [solar]	1.0 (frozen)	1.0 (frozen)	1.0 (frozen)	1.0 (frozen)
vnei.Ca [solar]	1.0 (frozen)	1.0 (frozen)	1.0 (frozen)	1.0 (frozen)
vnei.Fe [solar]	$1.3^{+0.6}_{-0.4}$	$6.0^{+2.05}_{-1.4}$	$5.3^{+3.4}_{-3.3}$	1.0 (frozen)
vnei.Ni [solar]	1.0 (frozen)	1.0 (frozen)	1.0 (frozen)	1.0 (frozen)
vnei.Tau [cm $^{-3}$ s]	$(9.9^{+1.9}_{-1.3}) \times 10^9$	$(4.0^{+1.3}_{-0.5}) \times 10^9$	$(3.7^{+1.1}_{-0.6}) \times 10^9$	$(2.9^{+0.9}_{-0.7}) \times 10^{10}$
vnei.norm	$(4.5^{+1.1}_{-0.7}) \times 10^{-5}$	$(7.7^{+4.6}_{-1.2}) \times 10^{-5}$	$(4.0^{+0.8}_{-1.5}) \times 10^{-5}$	$(6.0^{+0.29}_{-0.8}) \times 10^{-5}$
powerlaw.PhoIndex	2.720 (frozen)	-	-	$2.720^{+0.009}_{-0.007}$
powerlaw.norm	$(2.9^{+1.4}_{-1.3}) \times 10^{-6}$	-	-	$(3.318^{+0.014}_{-0.025}) \times 10^{-4}$
gaussian.LineE [keV]	$0.587^{+0.0012}_{-0.005}$	$0.5887^{+0.0020}_{-0.0019}$	$0.593^{+0.0017}_{-0.006}$	$0.610^{+0.004}_{-0.007}$
red. χ^2 (DoF)	1.455 (289)	1.197 (371)	1.049 (337)	1.130 (841)
flux [10^{-13} erg s $^{-1}$ cm $^{-2}$]	1.442 ± 0.020	$1.63^{+0.016}_{-0.04}$	2.92 ± 0.04	$11.04^{+0.026}_{-0.04}$

the consideration that the non-thermal component should show the same characteristics throughout the whole supernova remnant. Only the strength of the non-thermal emission should vary. The best fit of region 4 yielded a value of $2.720^{+0.009}_{-0.007}$ for the `powerlaw` photon index (`powerlaw.PhoIndex`). According to Sect. 3.4.3 this value is in agreement with literature values of young SNRs. In the fitted model a solar wind charge exchange line modeled by a Gaussian line with width 0 was included. This line probably results from a Fe or Ca transition. Its line energy is given by `gaussian.LineE` in Tab. 5.2.

In the `vnei` component the redshift was frozen to 0 and only the abundances of oxygen (`vnei.O`), magnesium (`vnei.Mg`), silicon (`vnei.Si`), sulfur (`vnei.S`), and iron (`vnei.Fe`) were left free, all other abundances (`vnei.H`, `vnei.He`, `vnei.C`, `vnei.N`, `vnei.Ne`, `vnei.Ar`, `vnei.Ca`, and `vnei.Ni`) were frozen to the solar value. This applies to regions 1, 2, and 3. For region 4 even these metal abundances were frozen to the solar value, meaning that all element abundances were considered to be solar. Since the `powerlaw` component was negligible for regions 2 and 3, it was removed when analyzing the spectra of these regions. For fitting region 1 the `powerlaw` photon index was set to 2.720. For all four regions a solar wind charge exchange line needs to be included, with only slightly different line energy. In Fig. 5.4 and Fig. 5.5 this line is depicted by the dashed lines.

Comparing the fit parameters shows, that the absorption column (`tbabs.nH`) changes only slightly in the four considered regions. The lowest value can be found in region 4, where the absorption column is about one fifth of the value in region 2, where the highest absorption column was determined. Since the values of the absorption columns of region 1 and region 3 are rather similar, one can conclude that region 1 is not affected by stronger absorption than the other regions as was suspected when defining the regions for spectral analysis. This means the reason why region 1 appears darker lies not in a higher absorption column in the line of sight to this region but might be a result of the intrinsic shape of the remnant.

The change in the plasma temperature (`vnei.kT`) of the thermal emission is more or less on the same level of significance. The coldest temperature was again derived in region 4, the highest in region 2, where the temperature is more than three times higher than in region 4. The values of region 2 and region 3 are in good agreement with literature values for young supernova remnants according to Sect. 3.4.1, whereas, the values of region 1 and region 4 are slightly below the literature values.

The metal abundances vary quite much from one region to another. In the regions 1, 2, and 3, which are dominated by the thermal component, sulfur is by far the most abundant element, followed by silicon. In general, most of the varied element abundances are strongly enhanced compared to the solar values in these regions. For a remnant of a thermonuclear supernova an enhancement of the abundance of these elements is expected since in the thermonuclear runaway process fusion was ignited again. And during the explosion the progenitor star gets completely disrupted, which leads to the ejection of all material of the progenitor. Therefore, an enhancement in metal abundances is expected. In the non-thermal dominated region 4 the element abundances are set to the solar value. Therefore, it is not possible to investigate the difference in metal abundances between the thermal and non-thermal dominated regions.

It is remarkable that the ionization timescale (`vnei.Tau`) of the thermal component is highest in region 4, followed by region 1. However, for all regions the ionization timescale

agrees with literature values according to Sect. 3.4.1. This means the assumption that the plasma is in non-equilibrium ionization holds.

Looking at the reduced χ^2 -value the best fit was achieved for region 3. However, for regions 2 and 4 very good fits were reached as well. The fit to the spectrum of region 1 is a little bit worse but nevertheless considered to be good.

The absorbed flux values in the energy range 0.3–10.0 keV (see Tab. 5.2) are in good agreement for regions 1, 2, and 3 where the values of the absorbed fluxes are $(1.442 \pm 0.020) \times 10^{-13} \text{ erg s}^{-1} \text{ cm}^{-2}$ for region 1, $(1.63_{-0.04}^{+0.016}) \times 10^{-13} \text{ erg s}^{-1} \text{ cm}^{-2}$ for region 2, and $(2.92 \pm 0.04) \times 10^{-13} \text{ erg s}^{-1} \text{ cm}^{-2}$ for region 3, respectively. The value of region 4 is with $(11.04_{-0.04}^{+0.026}) \times 10^{-13} \text{ erg s}^{-1} \text{ cm}^{-2}$ slightly higher, which can be explained by the fact that more hard photons were detected in this region.

5.7 Estimating the age of SNR 1006

The previously derived best-fit results can be utilized to estimate the age of the supernova remnant 1006. Assuming that the remnant has already entered the adiabatic phase of its evolution the Sedov-Taylor model holds, which was described in Sect. 3.3. In particular rewriting equation 3.5 yields a formula for the radius of the blast wave in units of parsec. To derive this equation one needs a value for α which can be obtained from calculations and yields a value of 1.15 (see, e.g., Truelove & McKee, 1999).

Furthermore, one can define an energy E_{51} which describes the explosion energy in units of 10^{51} erg, i.e.,

$$E_{51} = E_0 / (10^{51}) \quad (5.1)$$

with E_0 the explosion energy in units of erg. In addition, the age of the remnant can be expressed in units of 10^4 years, i.e.,

$$t_4 = t / (10^4 \cdot 365.25 \cdot 24 \cdot 3600) \quad (5.2)$$

with the age t in units of seconds. Converting the mass density ρ_0 into a particle density n_0 yields

$$n_0 = \frac{N}{V} = \frac{N}{M} \cdot \rho_0 \quad (5.3)$$

with the number of particles N in a volume V and the mass M of these particles. The mean number of particles and their mass can be estimated by assuming that 90% of the particles in the interstellar medium are given by hydrogen and 10% by helium. This assumption neglects the small amount of heavier elements. Since the particles are ionized the hydrogen atom is separated into two particles (one proton and one electron) with the mass of one proton m_p assuming that the mass of the electron is negligible. In the case of helium one yields three particles for one helium atom: one helium core (consisting of two protons and two neutrons) and two electrons. Considering the mass of the electrons as negligible the mass of these constituents is given by $2m_p$ and $2m_n$ with the mass of a neutron m_n . Therefore, the mean number of particles is given by

$$N = \underbrace{0.9 \cdot 2}_{90\% \text{ H}} + \underbrace{0.1 \cdot 3}_{10\% \text{ He}} = 2.1. \quad (5.4)$$

The mean particle mass can be calculated accordingly by

$$M = \underbrace{0.9 \cdot m_p}_{90\% \text{ H}} + \underbrace{0.1 \cdot (2m_p + 2m_n)}_{10\% \text{ He}} = 1.1 m_p + 0.2 m_n. \quad (5.5)$$

With the considerations above one can rewrite equation 3.5 into

$$\begin{aligned} R &= \alpha \cdot \left(\frac{E_0}{\rho_0} \right)^{1/5} \cdot t^{2/5} \\ &= 1.15 \cdot \left(\frac{10^{51} \cdot E_{51}}{n_0 \cdot M/N} \right)^{1/5} \cdot \left(10^4 \cdot 365.25 \cdot 24 \cdot 3600 \cdot t_4 \right)^{2/5} \\ &= 4.54 \cdot 10^{19} \cdot \left(\frac{E_{51}}{n_0} \right)^{1/5} \cdot t_4^{2/5}, \end{aligned} \quad (5.6)$$

where R is given in units of cm. Converting R into units of parsec yields

$$R = 14.72 \cdot \left(\frac{E_{51}}{n_0} \right)^{1/5} \cdot t_4^{2/5}. \quad (5.7)$$

When taking into account for instance heavier elements than H and He in the derivation one ends up with a slightly smaller prefactor of 14, i.e.,

$$R = 14 \cdot \left(\frac{E_{51}}{n_0} \right)^{1/5} \cdot t_4^{2/5}, \quad (5.8)$$

where E_{51} denotes the explosion energy in units of 10^{51} erg, n_0 represents the density of the uniform ambient medium in units of cm^{-3} , and t_4 describes the age in units of 10^4 years (Seward & Charles, 2010).

Furthermore, in order to obtain an equation for the age of the supernova remnant one can derive an equation for the temperature T immediately after the shock by assuming that the expansion velocity of the remnant equals the outer shock velocity, i.e.,

$$T = 1.0 \times 10^{10} \cdot \left(\frac{E_{51}}{n_0} \right) \cdot R^{-3}, \quad (5.9)$$

where the temperature T is given in units of K (Seward & Charles, 2010).

The radius R of the blast wave can be derived considering the situation depicted in Fig. 5.6. An extended source with radius R at distance d to the observer is seen under the viewing angle δ . Therefore, the radius R can be calculated via

$$R = d \cdot \tan \left(\frac{\delta}{2} \right). \quad (5.10)$$

The distance to SNR 1006 was determined to (2.17 ± 0.08) kpc (Long et al., 2003) and the viewing angle $\delta/2$ is $929.6''$. These values translate into a radius of the remnant of (9.8 ± 0.4) pc which is in good agreement with the value of 9.5 pc stated by Long et al. (2003).

Solving equation 5.9 for the term E_{51}/n_0 , i.e.,

$$\frac{E_{51}}{n_0} = \frac{T}{1.0 \times 10^{10}} \cdot R^3, \quad (5.11)$$

allows to replace this term in equation 5.8. After solving equation 5.8 for the age t_4 this yields

$$t_4 = \left(\frac{R}{14}\right)^{5/2} \cdot \left(\frac{T}{1.0 \times 10^{10}} \cdot R^3\right)^{-1/2} = 14^{-5/2} \cdot \left(\frac{T}{1.0 \times 10^{10}}\right)^{-1/2} \cdot R \quad (5.12)$$

The temperature T can be calculated from the plasma temperature `vnei.kT` of the best-fit results. First the mean value of the three regions dominated by the thermal emission (region 1, 2, and 3) was determined. Then this mean value and the plasma temperature derived for region 4, which is dominated by the non-thermal emission, were used to calculate an average value for the whole remnant. This average has a value of (0.44 ± 0.04) keV which translates into a temperature of $T = (5.2 \pm 0.5) \times 10^6$ K.

Inserting the derived values for the temperature T and the radius R results in an age t of (5.9 ± 0.4) kyr. Since the supernova of which SNR 1006 is the remainder was observed in the year 1006 AD, the real age of the remnant is approximately 1000 years, i.e., the estimated age is by a factor of ≈ 6 too high. On one side the determination of the temperature adds quite some uncertainty to the derived age. For the calculation of the temperature T only the four previously defined regions were considered. As can be already seen from these regions the plasma temperature `vnei.kT` varies from one region to the other. Not only between the regions dominated by the thermal and the non-thermal emission there is a clear difference in the plasma temperature derived by the spectral fits visible. Also for the three regions dominated by the thermal emission varying plasma temperature values were determined. This leads to the conclusion that the plasma temperature varies over the whole remnant. Therefore, instead of determining plasma temperatures for specific regions of the supernova remnant one should rather derive a plasma temperature for the region directly behind the blast wave where no emission from ejecta is present. Nevertheless, since the plasma temperature varies across the surface of the remnant this will still impose a rather high uncertainty to the estimated age.

In addition, SNR 1006 is a young supernova remnant which has either just entered the Sedov phase of its evolution or is at the transition to this phase right now. This means that strictly speaking the Sedov-Taylor model, on which the estimate of the age is based, might not be applicable. Since in the earliest stages of supernova remnant evolution the expansion velocity is the highest the radius of the remnant increases more than assumed by the Sedov-Taylor model. As can be seen from equation 5.12 a higher radius also results in a higher age value, i.e., for young supernova remnants that just entered the adiabatic phase of their evolution the Sedov-Taylor model will overestimate their age.

Although the estimated age and the expectations differ by a factor of ≈ 6 they are still on the same order of magnitude and, therefore, the determined age with the Sedov-Taylor model is considered as a good rough estimate for the real age.

5.8 Preparing the simulation

After analyzing the *XMM-Newton* data of SNR 1006, simulations for the *eROSITA* all-sky survey were performed in order to compare the well studied *XMM-Newton* data with expectations for the *eROSITA* mission. For running the simulations a file containing the basic characteristics of SNR 1006 is needed as an input. Section 6.1 gives a more detailed explanation of the used file format. The basic characteristics of an astronomical source like a supernova remnant include spectral information such as fit models and parameters, a flux value in a certain energy band, and the photon distribution provided by an image of the source. In order to obtain all these information for SNR 1006 it is necessary to make a few more considerations.

Looking at the spectra two energy ranges can be determined where either the thermal or the non-thermal component is dominating. In agreement with this fact, the input for the simulation will consist of two components to describe the supernova remnant: a thermal and a non-thermal component. The band dominated by the thermal component ranges from 0.3 keV up to 2.0 keV. For modelling this component the mean fit parameter values of region 1, 2, and 3 can be used. In the range from 3.0 keV up to 5.0 keV the spectrum of SNR 1006 is dominated by the non-thermal component, which can be described by the derived best fit model of region 4. Since the best-fit model of region 1 included a `powerlaw` component whereas the models of regions 2 and 3 did not, region 1 was also fitted without this `powerlaw` contribution. This allows to constrain mean fit parameters for the regions 1, 2, and 3. The resulting best fit parameters are listed in Tab. 5.3. For the sake of completeness also the parameters for the other regions are given. Although different absorption columns were determined for the different regions, for the simulation only one single value is used. For this value the mean absorption column of regions 1, 2, and 3 is calculated first. Afterwards the mean of this value and the value of the absorption column derived in region 4 is determined. The resulting absorption column used for the simulation is $0.259 \times 10^{22} \text{ cm}^{-2}$. Nevertheless, this value is about four times higher than the value given by the program `nh` at the source position. The flux value for the thermal component was derived in the 0.3–2.0 keV energy band of regions 1, 2, and 3 and the one for the non-thermal component in the 3.0–5.0 keV energy band of region 4. In order to get the photon distribution of these two components, mosaic images in both energy bands were created. Finally, with the flux, the mosaic images and the spectral models all necessary information to describe the source is known and can be used to create a so called SIMPUT file, which is used to deliver all necessary information of the source to the simulation software. A more detailed description of this file format is given in Sect. 6.1.

In the energy band of 0.3–2.0 keV for regions 1, 2, and 3, the flux values vary only slightly. In contrast, the flux value of region 4 in a hard energy band 3.0–5.0 keV changes by approximately one order of magnitude compared to the value in the range 0.3–10.0 keV. The flux value of region 4 in the hard band is now comparable to the values of the regions 1, 2, and 3 in the range 0.3–10.0 keV.

Table 5.3: Best fit parameters for all four regions like in Tab. 5.2. In order to allow to combine the models for region 1, 2, and 3 to a single one that can be used as an input for the simulation, the **powerlaw** component in region 1 was removed. In addition, the mean values of the regions 1, 2, and 3 are shown.

parameter	region 1	region 2	region 3	mean	region 4
tbabs.nH [10^{22} cm^{-2}]	$0.374^{+0.020}_{-0.024}$	$0.60^{+0.05}_{-0.018}$	$0.24^{+0.03}_{-0.06}$	0.259	0.259
vnei.kT [keV]	$0.433^{+0.025}_{-0.04}$	$0.74^{+0.09}_{-0.18}$	$0.6^{+0.20}_{-0.09}$	0.59	$0.293^{+0.010}_{-0.007}$
vnei.H [solar]	1.0 (frozen)	1.0 (frozen)	1.0 (frozen)	1.0 (frozen)	1.0 (frozen)
vnei.He [solar]	1.0 (frozen)	1.0 (frozen)	1.0 (frozen)	1.0 (frozen)	1.0 (frozen)
vnei.C [solar]	1.0 (frozen)	1.0 (frozen)	1.0 (frozen)	1.0 (frozen)	1.0 (frozen)
vnei.N [solar]	1.0 (frozen)	1.0 (frozen)	1.0 (frozen)	1.0 (frozen)	1.0 (frozen)
vnei.O [solar]	$3.1^{+0.4}_{-0.4}$	$6.2^{+0.8}_{-0.6}$	$4.0^{+0.7}_{-0.5}$	4.43	1.0 (frozen)
vnei.Ne [solar]	1.0 (frozen)	1.0 (frozen)	1.0 (frozen)	1.0 (frozen)	1.0 (frozen)
vnei.Mg [solar]	$2.3^{+0.5}_{-0.5}$	$3.0^{+0.3}_{-0.3}$	$9.4^{+2.2}_{-2.3}$	4.89	1.0 (frozen)
vnei.Si [solar]	$64.1^{+15.3}_{-13.2}$	$27.7^{+18.9}_{-2.0}$	$96.8^{+30.9}_{-30}$	62.86	1.0 (frozen)
vnei.S [solar]	$388.1^{+88.3}_{-76.8}$	$37.5^{+58.8}_{-10.7}$	$187.1^{+84.7}_{-51.6}$	204.23	1.0 (frozen)
vnei.Ar [solar]	1.0 (frozen)	1.0 (frozen)	1.0 (frozen)	1.0 (frozen)	1.0 (frozen)
vnei.Ca [solar]	1.0 (frozen)	1.0 (frozen)	1.0 (frozen)	1.0 (frozen)	1.0 (frozen)
vnei.Fe [solar]	$1.5^{+0.6}_{-0.5}$	$6.0^{+2.05}_{-1.4}$	$5.3^{+3.4}_{-3.3}$	4.26	1.0 (frozen)
vnei.Ni [solar]	1.0 (frozen)	1.0 (frozen)	1.0 (frozen)	1.0 (frozen)	1.0 (frozen)
vnei.Tau [$\text{cm}^{-3} \text{ s}$]	$(9.6^{+1.6}_{-1.2}) \times 10^9$	$(4.0^{+1.3}_{-0.5}) \times 10^9$	$(3.7^{+1.1}_{-0.6}) \times 10^9$	5.76×10^9	$(2.9^{+0.9}_{-0.7}) \times 10^{10}$
vnei.norm	$(5.2^{+1.0}_{-0.27}) \times 10^{-5}$	$(7.7^{+4.6}_{-1.2}) \times 10^{-5}$	$(4.0^{+0.8}_{-1.5}) \times 10^{-5}$	5.63×10^{-5}	$(6.0^{+0.29}_{-0.8}) \times 10^{-5}$
powerlaw.PhIndex	-	-	-	-	$2.720^{+0.009}_{-0.007}$
powerlaw.norm	-	-	-	-	$(3.318^{+0.014}_{-0.025}) \times 10^{-4}$
gaussian.LineE [keV]	$0.5871^{+0.0011}_{-0.003}$	$0.5887^{+0.0020}_{-0.0019}$	$0.593^{+0.0017}_{-0.006}$	-	$0.610^{+0.004}_{-0.007}$
red. χ^2 (DoF)	1.489 (290)	1.197 (371)	1.049 (337)	-	1.130 (841)
flux (0.3 – 10.0 keV) [$10^{-13} \text{ erg s}^{-1} \text{ cm}^{-2}$]	1.387 ± 0.020	$1.63^{+0.016}_{-0.04}$	2.92 ± 0.04	-	$11.04^{+0.026}_{-0.04}$
flux (0.3 – 2.0 keV) [$10^{-13} \text{ erg s}^{-1} \text{ cm}^{-2}$]	1.361 ± 0.019	$1.581^{+0.015}_{-0.030}$	2.884 ± 0.04	1.837	-
flux (3.0 – 5.0 keV) [$10^{-13} \text{ erg s}^{-1} \text{ cm}^{-2}$]	-	-	-	-	$1.0224^{+0.0024}_{-0.004}$

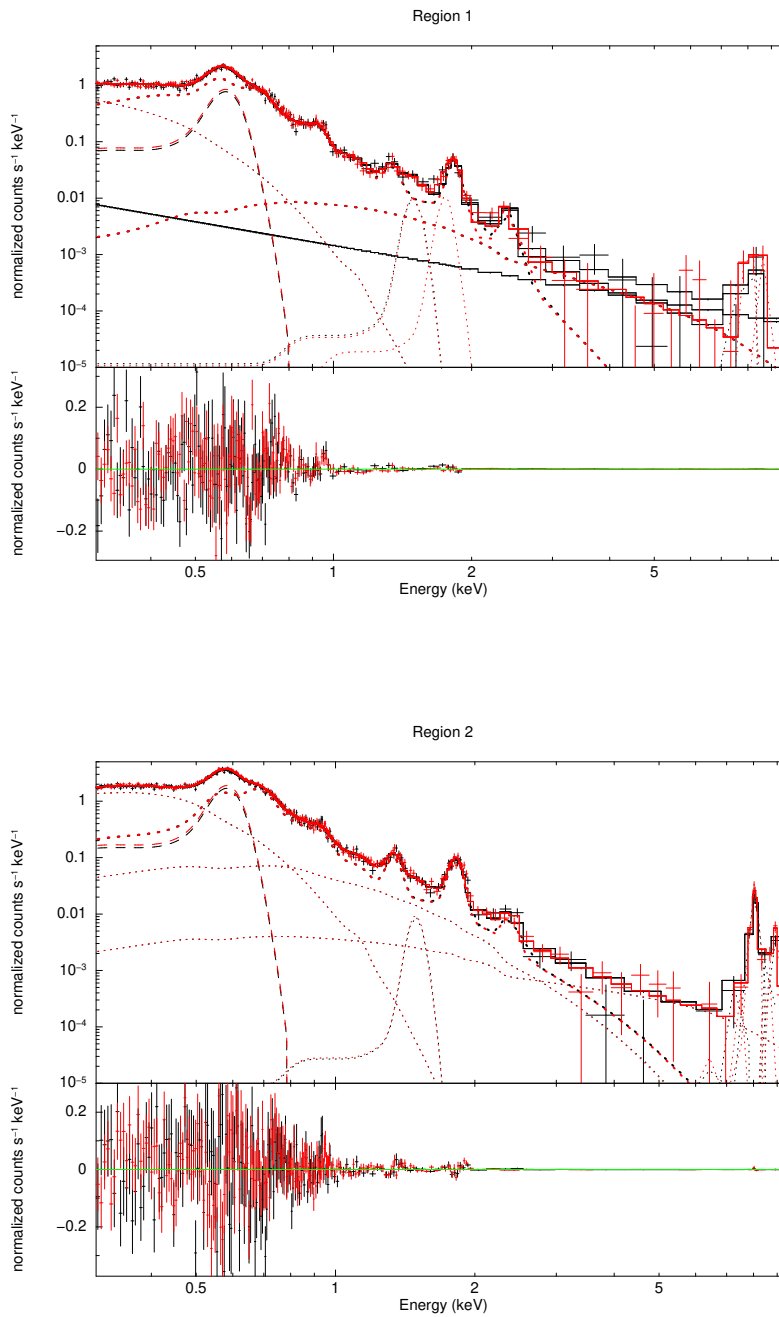


Figure 5.4: PN spectra of region 1 (top) and region 2 (bottom). Black shows data and model components from obsID 0555630101 and red from obsID 0555631001. The thick dotted lines represent source model components, whereas the thin ones denote additional background components. The dashed lines symbolize the SWCX component of the fit model. The black solid line in the upper panel depicts the modeled remaining particle background.

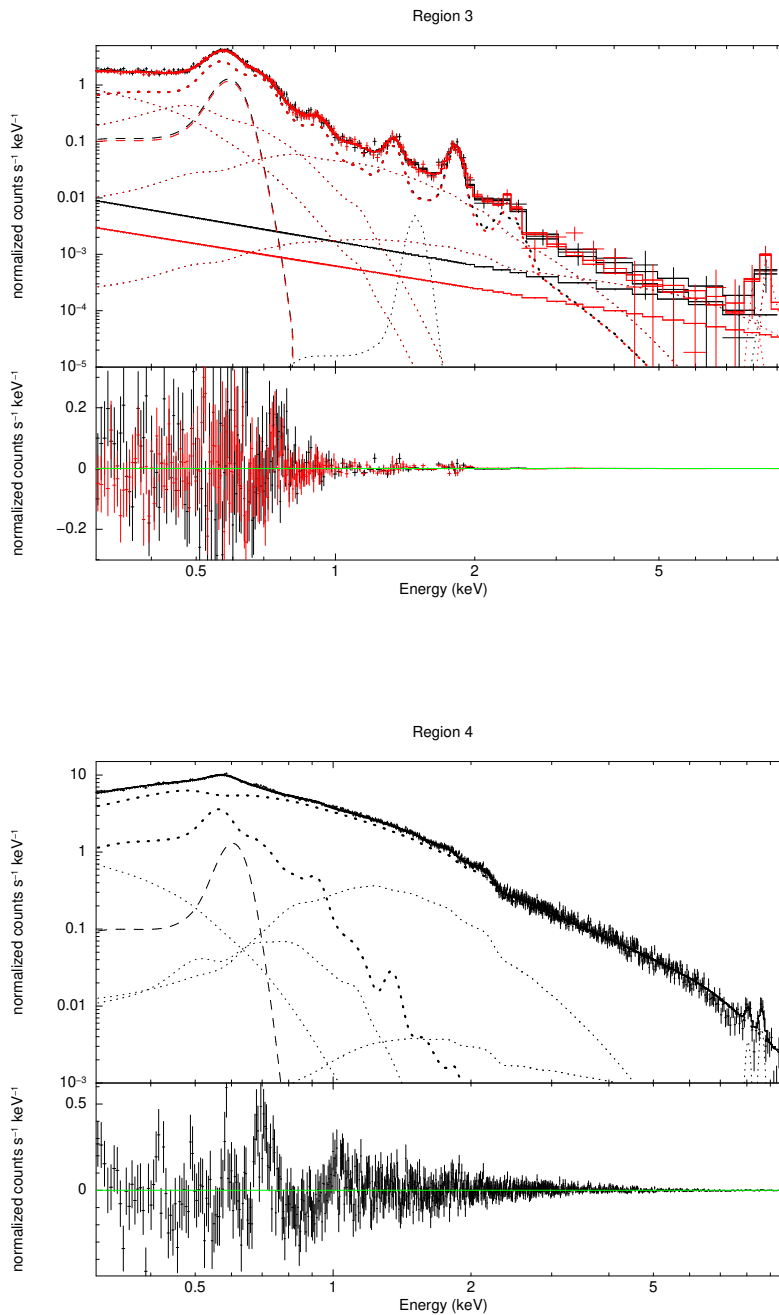


Figure 5.5: PN spectra of region 3 (top) and region 4 (bottom). In the upper panel black shows data and model components from obsID 0555630101 and red from obsID 0555631001. The solid lines depict the modeled remaining particle background of each observation. The lower panel shows data and model components from obsID 0653860101. The thick dotted lines represent source model components, whereas the thin ones denote additional background components. The dashed lines symbolize the SWCX component of the fit model.

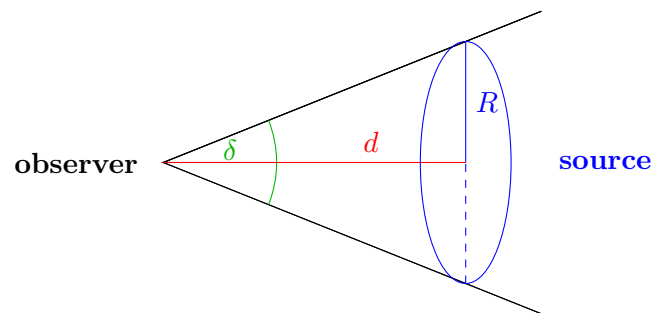


Figure 5.6: Viewing angle of an extended object with radius R at distance d from the observer.

6 Simulation and data extraction software for *eROSITA*

The following chapter contains information about the software used for the simulation and additionally the one used to extract and analyze the simulated data.

6.1 SIMPUT

The simulation software uses a so called SIMPUT file as an input. This is a standard format for source input files, which is used in simulations of astronomical observations. The name is an abbreviation for SIMulation inPUT. For a more detailed description see the definition document¹. The SIMPUT file format specification is based on the FITS standard (Wells et al., 1981; Ponz et al., 1994; Hanisch et al., 2001; Pence et al., 2010). SIMPUT files contain a catalog with one or multiple sources, which are described by specific properties such as their position, brightness, and energy spectrum, as well as optional characteristics such as time variability or spatial extent. The source catalog extension contains the following parameters:

SRC_ID	the ID of each source
SRC_NAME	the name of each source
RA, DEC	the coordinates of the source in the equatorial coordinate system
IMGROTA	rotation angle/polarization vector
IMGSCAL	scaling factor for extended sources
E_MIN, E_MAX	boundaries of the energy band, in which the flux is given
FLUX	the flux emitted by the source in the specified energy band
SPECTRUM	a link to the spectrum extension
IMAGE	a link to the image extension
TIMING	a link to the timing extension (lightcurve)

The parameters SRC_ID, RA, DEC, E_MIN, E_MAX, FLUX, and SPECTRUM are mandatory. The other parameters are optional. The spectrum extension describes the energy spectrum of the source. If more than one source is considered each row of the spectrum extension describes a single source. In the case of providing a mission-independent spectrum, the data are organized as a binary table with two mandatory columns giving an

¹<http://hea-www.harvard.edu/heasarc/formats/simput-1.1.0.pdf> (accessed on 2020 January 27)

energy grid and the photon flux density at the respective energies. If an extended source is studied the image extension describes the spatial flux distribution. One image extension corresponds to a single source. For point sources an image extension is not needed. Since supernova remnants are not expected to show time variability on timescales, which are important during the *eROSITA* all-sky survey, the timing parameter can be neglected in that case.

6.2 SIXTE

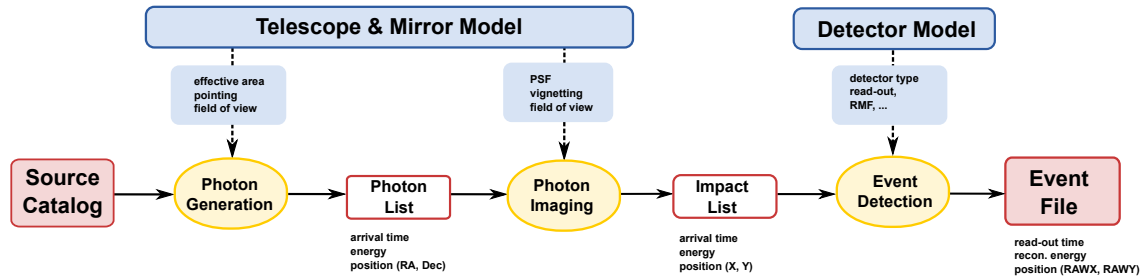


Figure 6.1: Flow chart illustrating the three major functional blocks of the SIXTE software (taken from Dauser et al., 2019).

In this work the Simulation of X-ray Telescopes (SIXTE) software package is used (Schmid, 2012; Dauser et al., 2019). It is a generic, mission-independent Monte Carlo simulation toolkit for X-ray astronomical instrumentation, which is based on a modular approach for source definition, description of the optics, and the detector type. Detailed information about the implementation and usage of the software can be found in the SIXTE manual².

Fig. 6.1 shows a flow chart with the three major functional blocks of the SIXTE simulation software. The first step is the generation of photons from the source catalog provided by the SIMPUT file. While the source list can cover a sky area, which is much larger than the part of the sky observed by the telescope, photons are only generated for sources within the telescope’s field of view. This saves computational time and results in a photon list containing the arrival time, the energy, and the sky position of the incoming photons. For the imaging process the PSF, vignetting, and the FOV of the telescope are taken into account. The output of the imaging step is an impact list, where information on the photon arrival time, energy, and position on the detector are stored. This impact list is used for the event detection. In this step, amongst others, the detector type, readout, and the redistribution matrix (RMF) are considered. The RMF describes the probability that a certain signal is measured for a given input photon energy (Dauser et al., 2019). Finally, event reconstruction takes place and the important information such as event time, reconstructed energy, and detector position of the event are written into an event file. This event file can then be used to derive source products such as an image or a spectrum of

²https://www.sternwarte.uni-erlangen.de/research/sixte/data/simulator_manual.pdf (accessed on 2020 January 27)

the simulated source. In the case of *eROSITA* seven event files are created, one for each telescope.

The SIXTE package provides some general and some mission specific tools. For instance, the tool `erosim` is a derivative of the general tool for performing simulations, `runsixt`, which is specialized to the setup of the *eROSITA* experiment. The most important parameters of `erosim` are:

XMLFile: There are seven XML files, one for each sub-instrument, describing the main characteristics of the telescopes and detectors. They contain information on the FOV diameter, the focal length, the Ancillary Response File (ARF) and RMF, the PSF, the pixel size, vignetting, the charge cloud size, and the readout mode.

Background: For inclusion of the particle background.

Attitude: The attitude file describes the pointing position of the telescopes as a function of time. If this file is not provided, SIXTE will perform a pointed observation instead of an all-sky survey observation.

RA, Dec: The position of the telescope pointing in the equatorial coordinate system.

Simput: The catalog of sources, which will be simulated.

MJDREF: The time in the event files will be given with respect to this reference Modified Julian Date (MJD). As the name foretells this dating convention is a modification of the Julian Date (JD) which numbers all days in a consecutive fashion starting with 4713 B.C. January 1 at noon. The Modified Julian Date begins at midnight and leaves out the first two digits of the Julian Date, i.e., it can be calculated via $MJD = JD - 2400000.5$ ³.

TSTART: This parameter denotes the start time of the observation.

Exposure: The exposure time of the simulated observation.

GTIFile: The Good Time Interval file is an optional parameter which contains time intervals for which the simulation should be performed. It overwrites TSTART and Exposure.

In order to convert the resulting event file into the *eROSITA*-specific calibrated event file format, the SIXTE tool `ero_cal_events` is used.

The visibility of an X-ray source at a particular position in the sky during the *eROSITA* all-sky survey can be determined with the tool `ero_vis`. The advantage of the created GTI file by this tool is that not the whole survey needs to be simulated but only the time intervals when the simulated source is within *eROSITA*'s FOV and can be detected. This saves computational time. The SIXTE tool `ero_vis` has the following parameters:

Attitude: The attitude file giving *eROSITA*'s pointing positions changing over time.

Simput: The source catalog file.

SrcRA, SrcDec: Source position in equatorial coordinates. These are overwritten by the source catalog file if it is given.

³<https://core2.gsfc.nasa.gov/time/> (accessed on 2020 May 4)

GTIfile: The name of the output GTI file.

TSTART: The starting time of the simulated observation.

Exposure: The exposure time of the simulated observation.

dt: The time step for the GTI calculation in seconds.

visibility_range: The diameter of the telescope's field of view.

With these tools one can perform simulations of *eROSITA* observations of sources defined in the SIMPUT file. For extracting source products like images or spectra from the simulation, the *eROSITA* Science Analysis Software System (eSASS) is used.

6.3 eSASS

The *eROSITA* Science Analysis Software System (eSASS) is a software package that comprises tasks for pipeline operation and for interactive data analysis. It is partly based on knowledge and code from the *ROSAT* data analysis software and the *XMM-Newton* Science Analysis System (XMM-SAS) (Brunner et al., 2018). Amongst others, its tasks include event calibration, map creation (e.g., exposure maps or sensitivity maps), source detection tools, and event manipulation tools such as creating images, spectra, or lightcurves⁴. Important tools for the work done in the scope of this thesis are `evtool`, which allows to produce images, and `srctool`, which is used for extracting spectra from the event files. For simulated event files a preparatory task needs to be done beforehand. This step makes use of the tool `radec2xy`, which calculates sky pixel coordinates via a tangential parallel projection. Images then can be created with the tool `evtool`, which takes one or multiple event files and an energy range as input. For producing spectra or lightcurves `srctool` is used. This tool requires one or multiple event files and the target coordinates as input parameters. Optional parameters are, for instance, a source or background extraction region, a source extent model for extended sources, and a list of operations to be carried out. Possible operations are, for instance, extracting spectra or lightcurves, or producing ARF and RMF files.

6.4 Data extraction without the use of eSASS

Since at first the energy calibration was not implemented for the *eROSITA* mission an energy shift was observed in the simulated spectra due to an incorrect conversion from PHA (Pulse Height Amplitude) values to PI (Pulse Invariant) values. A PHA file contains the data of an X-ray spectrum, typically in a form of number of counts observed in each spectral channel of the detector (Arnaud et al., 2009). Since the PHA does not state the proper reconstructed photon energy a reconstruction step is necessary, which depends on the response of the detector. This calibration step then yields a PI value (Dauser et al., 2019). Further information on the conversion from PHA to PI can be found in the SIXTE manual⁵. Unfortunately, a correct energy calibration for the *eROSITA* mission became

⁴<https://erosita.mpe.mpg.de/eR0doc/> (accessed on 2020 January 27)

⁵http://www.sternwarte.uni-erlangen.de/research/sixte/data/simulator_manual_v1.3.10.pdf (accessed on 2020 February 26)

only available after the evaluation of the simulations. Therefore, in the analysis of the simulations for *eROSITA* further tools of the SIXTE package were used for extracting images and spectra from simulated event files. This did not affect the results of the analysis.

Before images and spectra can be created it is necessary to add some information regarding the world coordinate system (WCS) to the header of the event files from the simulation. This allows to correctly perform projections, for instance from detector coordinates into sky coordinates. After that, images can be created using the tool `imgev` of the SIXTE software package. The tool takes an event file and some parameters regarding the WCS and projection as input. It is not possible to define a certain energy range in which the image is created. Therefore, for creating tricolor images one needs to filter the event files for the desired energy range using `fselect`.

Spectra are created using the tool `makespec`. It takes simulated event files as input and, in addition, allows to filter for a certain region. For simulated all-sky survey data it is necessary to filter for a region where the coordinates are given in sky coordinates (RA and DEC) and not in detector coordinates (RAWX and RAWY). This becomes apparent when considering the source moving through the telescope's field of view, i.e., changing its position on the detector but not on the sky. Therefore, it is also important that the right WCS information was set in advance. Furthermore, if not only a spectrum of a source region but also one of a background is extracted, one needs to set the "BACKFILE" and the "BACKSCAL" keywords accordingly in the header of the source spectrum. The "BACKFILE" keyword states the path to the background spectrum. The "BACKSCAL" keyword is a scaling factor that takes into account that the area of the source region differs from the area of the background region.

7 Simulations of SNR 1006 for *eROSITA*

7.1 The SIMPUT file of SNR 1006

As pointed out in Sect. 5, the spectrum of the supernova remnant 1006 consists of a thermal and a non-thermal component. According to this result the SIMPUT file used for the simulations of SNR 1006 for *eROSITA* includes two components as well. Both components have a center position of $RA = 225.7065$ deg and $Dec = -41.95$ deg. For the thermal component the energy band 0.3–2.0 keV is considered. To derive the photon distribution for the thermal component an image in this energy range was created, which is presented on the left of Fig. 7.1. For the spectral description, the mean values of the fit model parameters of the analysed regions 1, 2, and 3 were used, which are given in Tab. 5.3. In the analysis of the *XMM-Newton* data, a flux value of 1.838×10^{-13} erg s $^{-1}$ cm $^{-2}$ was determined for the thermal component. This flux value needs to be scaled to a value of 1.15×10^{-11} erg s $^{-1}$ cm $^{-2}$ since the area in which it was determined (regions 1, 2, and 3) is smaller than the area of the whole remnant. But in the SIMPUT file the total observed flux from the source in the reference energy band is stated, therefore the scaling is needed. The non-thermal component is evaluated in the energy band 3.0–5.0 keV. For describing the photon distribution, an image in this energy range was created, which can be seen in Fig. 7.1 on the right. For the spectral model the fit parameters of region 4 from the *XMM-Newton* data analysis were used. The flux is scaled from 1.022×10^{-13} erg s $^{-1}$ cm $^{-2}$, which was derived for the analysis of region 4, to a value of 6.23×10^{-12} erg s $^{-1}$ cm $^{-2}$ in order to account for the greater area of the whole remnant compared to the area of region 4. All this information is put together into a FITS file, which is used as input for the simulations. Since a supernova remnant is not expected to show any variations on timescales of the *eROSITA* all-sky survey, no further information is necessary to describe the object.

7.2 Simulation results after one complete scan of the sky

As already mentioned in Sect. 4.3, *eROSITA* completes a scan of the entire sky in six months. Therefore, a first simulation was performed for an exposure time of six months to get a feeling what is feasible with the *eROSITA* data of the first half year of all-sky survey measurements in prospect of supernova remnants. Fig. 7.2 shows a tricolor composite image of the SNR 1006 after six months of the all-sky survey. Like already in the analysis of the *XMM-Newton* data red denotes the energy band 0.3–0.8 keV, green the band 0.8–2.0 keV, and blue 2.0–4.5 keV. Inside the region of the remnant a total amount of 1765 counts was registered. For an exposure time of 906 s, this results in a count rate of 1.95 counts per second. As is obvious from Fig. 7.2, after six months of all-sky survey too few counts are registered to determine model parameters by spectral fitting. Due to this fact, no further analysis of the data was performed. Instead, simulations for four years of all-sky survey were carried out and analyzed.

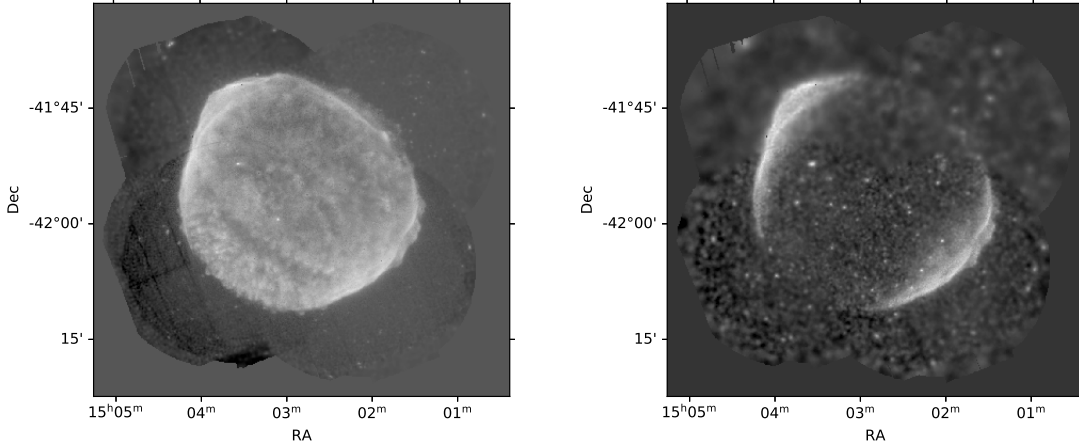


Figure 7.1: Composite images of the analysed *XMM-Newton* data in the energy band 0.3–2.0 keV (left) and 3.0–5.0 keV (right) to describe the photon distribution of the thermal and the non-thermal component, respectively.

7.3 Simulation results after four years of all-sky survey

A tricolor image of SNR 1006 after four years of all-sky survey is given in Fig. 7.3. As in Fig. 7.2, red denotes the energy band 0.3–0.8 keV, green the band 0.8–2.0 keV, and blue 2.0–4.5 keV. Over the whole remnant an amount of 14,938 counts was registered, which is in agreement with expectations for a factor 8 increase in exposure time. As expected, the count rate is with 1.96 counts per second almost the same. Since the source did not change its brightness one would expect to measure the same count rate although the simulated time range is higher. The higher amount of counts enables the extraction of spectra from the simulated data. In order to compare the results to the analysis of the *XMM-Newton* data, two regions were chosen, from which spectra were extracted. One region is located at the edge of the remnant, where the non-thermal component dominates. The other region covers the center of the remnant, where the thermal component dominates. Although the result of the all-sky simulation after four years is better than after six months in terms of registered counts, there are still less counts measured than in the *XMM-Newton* pointed observation data. In order to account for this fact, it is necessary to redefine the considered regions. In particular, the area of the regions needs to be enhanced to collect a reasonable amount of photons. The resulting regions are shown in Fig. 7.3 as well. In addition, the same figure also shows the region used for extracting a background spectrum, which is subtracted from the source spectra.

7.3.1 Spectral analysis

Contribution of the background

Before going into a detailed analysis of the simulated spectra of SNR 1006 after four years of *eROSITA* all-sky survey, it is worthwhile to have a look at the contribution of the background to the source spectra. Fig. 7.4 shows the source spectrum in red and

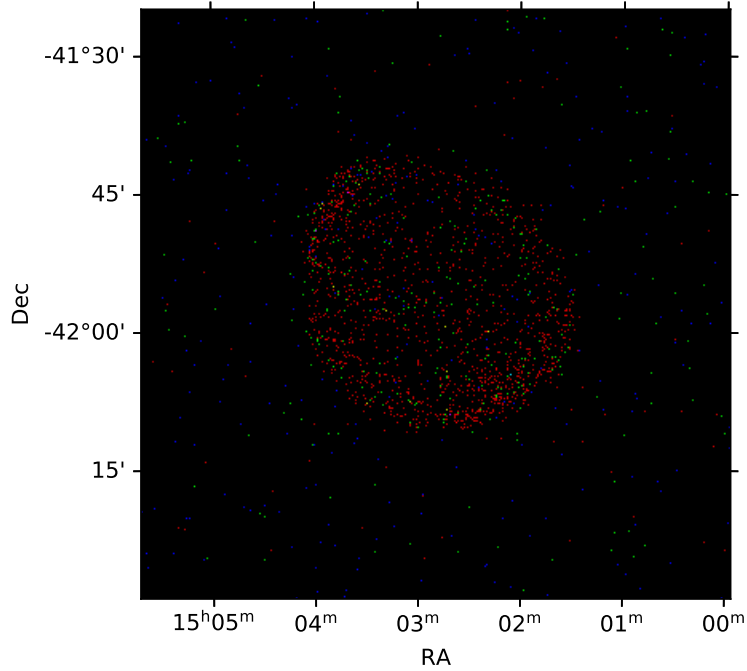


Figure 7.2: Simulated RGB image of SNR 1006 after six months of *eROSITA* all-sky survey. Red denotes the energy band 0.3–0.8 keV, green the band 0.8–2.0 keV, and blue 2.0–4.5 keV.

the background spectrum in black for region 1 (top) and region 2 (bottom), respectively. For simplicity only the data of the telescope module (TM) 7 are plotted. All spectra are extracted with the tool `makespec`. The source and background spectra of region 1 were binned to a minimum of 25 counts per channel, whereas the ones of region 2 were binned to a minimum of two counts per channel. It is obvious that the source spectra are dominated by the background for energies above ≈ 2 keV. This means that the main remaining component of the source spectra is the thermal component. This becomes even more clear when looking at the spectrum of region 2 (at the bottom of Fig. 7.4), which was extracted from a region where the non-thermal emission should dominate. Since this region is smaller than region 1, the overall amount of counts is smaller as well compared to region 1. In addition, the non-thermal part of the spectrum is masked by the background contribution. Only some thermal emission remains. This also becomes plausible when comparing the effective areas of *eROSITA* and *XMM-Newton*. Fig. 7.5 shows this comparison for the combined effective area of all *eROSITA* telescopes in red and the effective area of the *XMM* EPIC PN detector in black. In order to achieve a more reasonable comparison a pointed *eROSITA* observation was simulated and the effective area was calculated for a central circular region on the detector with the same size for both instruments. In the energy range ≈ 0.5 keV up to ≈ 2 keV the combined effective area of the *eROSITA* telescopes is higher than the one of the *XMM* EPIC PN detector. But above

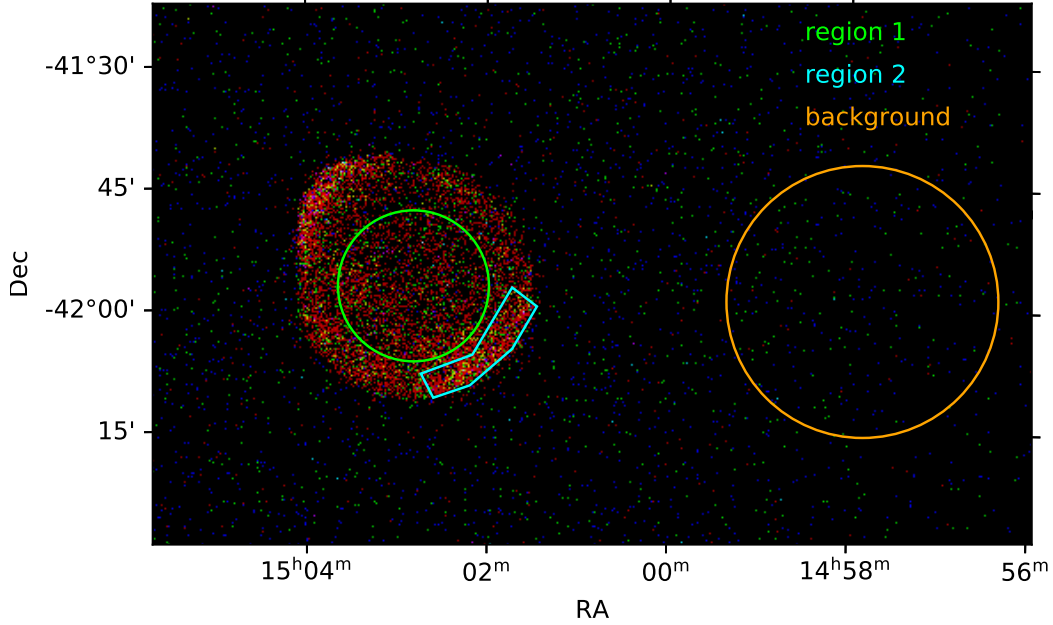


Figure 7.3: Simulated RGB image of SNR 1006 after four years of *eROSITA* all-sky survey. Red denotes the energy band 0.3–0.8 keV, green the band 0.8–2.0 keV, and blue 2.0–4.5 keV. Furthermore, the regions are plotted in which the source spectra for the thermal and the non-thermal dominated components were extracted. In orange, the region in which the background spectrum was extracted is shown.

this energy range the effective area of *XMM EPIC PN* is higher than *eROSITA*'s one, i.e., *XMM-Newton* is able to collect more photons of energies above ≈ 2 keV, which results in a better signal to noise ratio for higher energies compared to the *eROSITA* mission. However, one has to take into account that the effective area depends on the position of the source on the detector. Therefore, the effective area from a survey observation of *eROSITA* might deviate from the one of a simulated pointed observation. Nevertheless, Fig. 7.5 illustrates that the background will be stronger for energies above ≈ 2 keV for the *eROSITA* instrument than it is for *XMM-Newton EPIC PN*.

Spectral analysis of region 1

Region 1 covers the center of the remnant, where the thermal emission dominates. Fig. 7.6 shows the background subtracted spectra of all telescope modules. The spectra were binned to a minimum of 25 counts per channel in order to allow the use of the χ^2 -statistic.

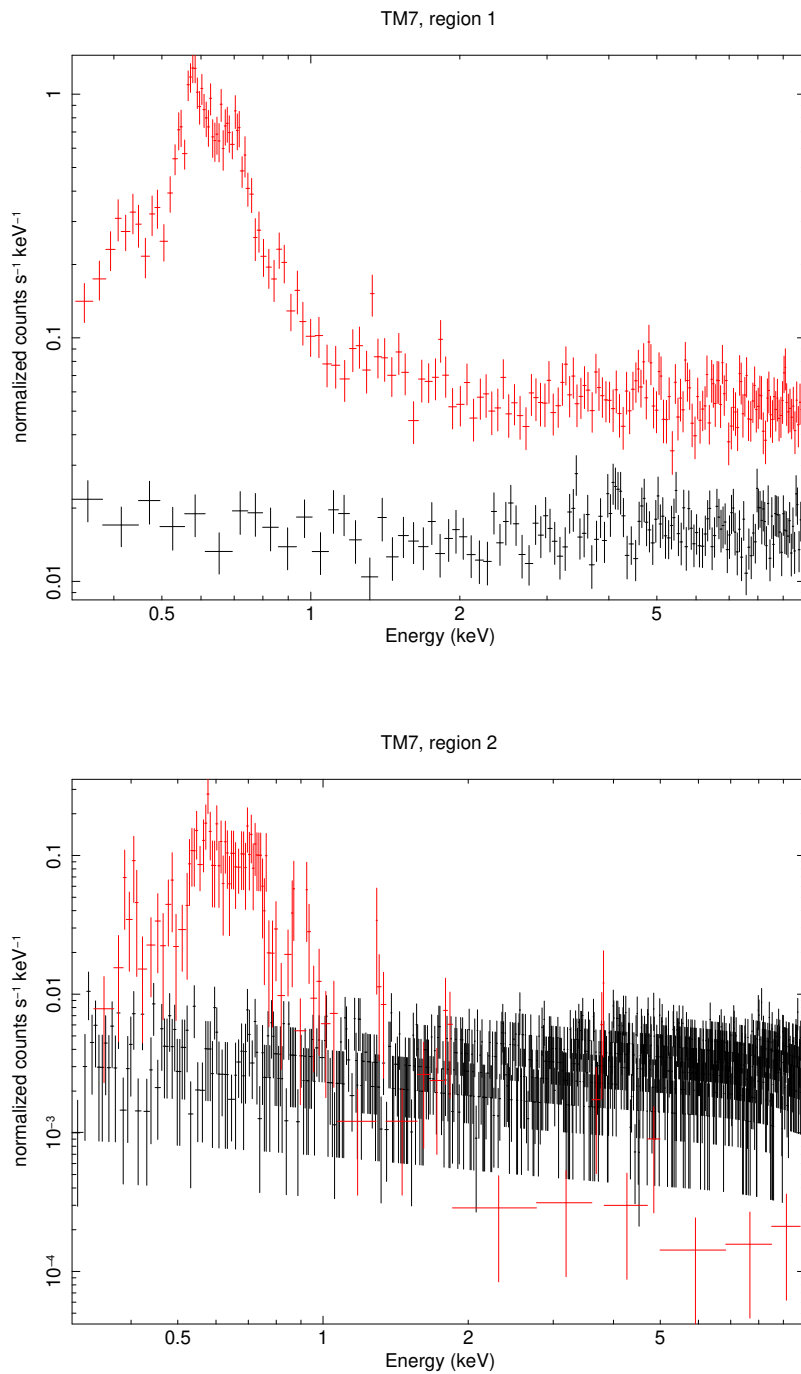


Figure 7.4: Simulated spectra of SNR 1006 of region 1 (top) and region 2 (bottom) after four years of *eROSITA* all-sky survey. Only the data of TM7 are shown. Red denotes the source spectrum and black the background spectrum. The spectra of region 1 are rebinned to a minimum number of 25 counts per bin, whereas the spectra of region 2 are rebinned to a minimum value of two counts per bin.

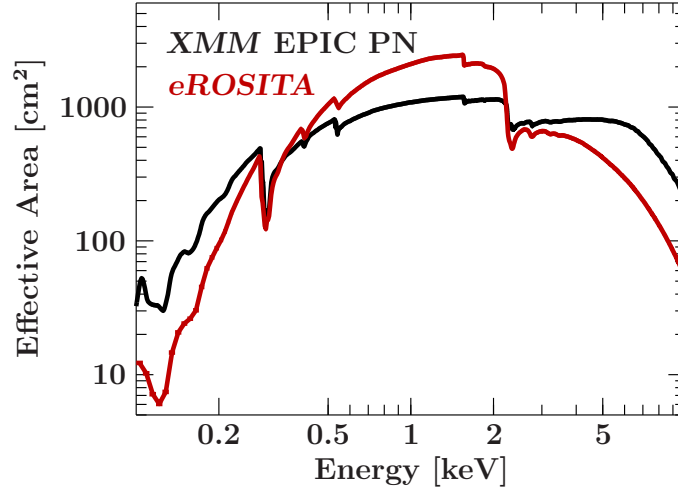


Figure 7.5: Comparison of the effective areas of all *eROSITA* telescopes combined in red and the *XMM-Newton* EPIC PN detector in black.

All spectra were fitted simultaneously in the energy range 0.3–10.0 keV. In the simulations the thermal and the non-thermal component are overlaid as can be seen in Fig. 7.1. For instance, an image of the source in the 3.0–5.0 keV band was used to define the region where the non-thermal component dominates. But the rims of the remnant are not only bright in this energy range but also in the 0.3–2.0 keV band, which was used for defining the region of the thermal component. Due to this, the whole remnant was simulated to be a superposition of the thermal and non-thermal component. To account for this superposition, the spectrum of the central region 1 needs to be modeled by a combination of the best-fit model of the thermal as well as of the non-thermal component, i.e., the source model is given by $\text{tbabs} \cdot (\text{vnei} + \text{vnei} + \text{powerlaw})$. Since a background spectrum was subtracted from each source spectrum it is not necessary to model the background in addition to the source. For fitting the spectra the absorption column density was frozen to $0.259 \times 10^{22} \text{ cm}^{-2}$ which is the average of the best-fit values of the absorption column densities of the different regions of the *XMM-Newton* data analysis. The parameters of the first *vnei* component were frozen to the mean values of region 1, 2, and 3 from the *XMM-Newton* data analysis, which can be found in Tab. 5.3, i.e., O, Mg, Si, S, and Fe are enhanced compared to the solar value. The parameters of the second *vnei* component were frozen to the values of region 4 from the *XMM-Newton* data analysis, i.e., solar metal abundances were used. The *powerlaw* photon index was frozen to 2.720. Only the normalizations of the single model components were left free, all other parameters were frozen. The resulting values for the normalizations as well as the reduced χ^2 are given in Tab. 7.1. The overall shape fits quite well. Nevertheless, the value of the normalization of the second *vnei* component cannot be determined well, only an upper limit can be given. This indicates that this component is not necessary to describe the spectra. However, the normalizations of the first *vnei* component and the *powerlaw* component are on a similar order of magnitude, i.e., a single *vnei* and a *powerlaw* component are necessary to describe the spectra of region 1.

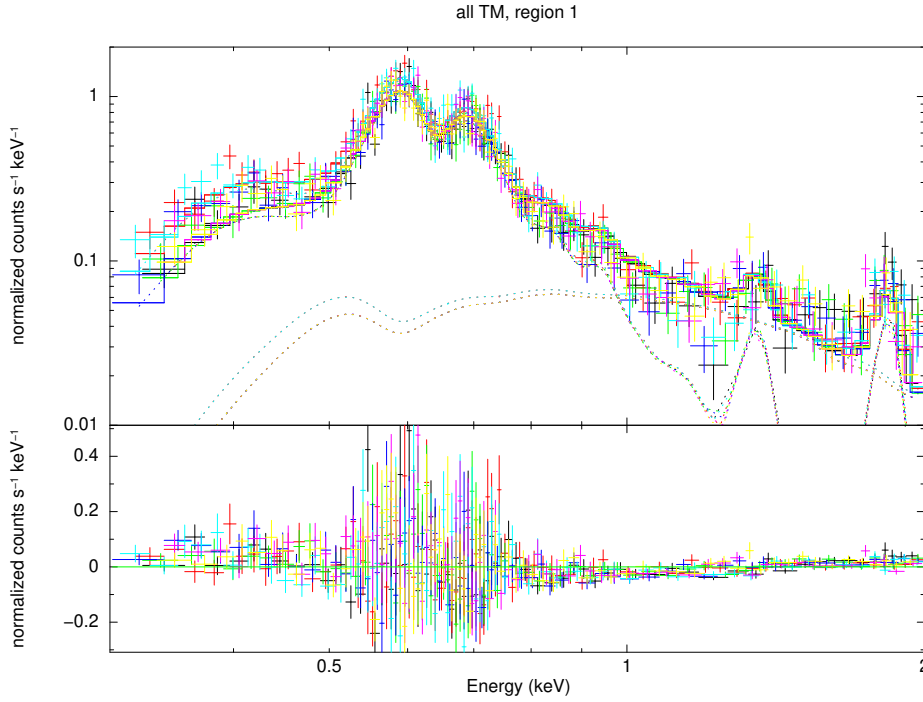


Figure 7.6: Simulated background subtracted source spectra of SNR 1006 of region 1 after four years of *eROSITA* all-sky survey. The data of all TM are shown. The color scheme is as follows: TM1 is shown in black, TM2 in red, TM3 in green, TM4 in blue, TM5 in cyan, TM6 in magenta, and TM7 in yellow. The dotted lines show the powerlaw and the first vnei component.

Looking at the absorbed flux values derived in the 0.3–10.0 keV and the 0.3–2.0 keV band these are on the same order of magnitude for region 1. Compared to the mean flux value of regions 1, 2, and 3 of the *XMM-Newton* data analysis, the flux values from the simulation are higher by approximately one order of magnitude. At least to some extent this can be explained by the fact that the region used for the analysis of the simulated spectra is bigger by a factor of ≈ 23 than the one used in the *XMM* data analysis. This means since integrated flux values are determined the value of the simulations should be higher by the same factor than the mean flux value derived in the *XMM-Newton* data analysis (see Tab. 5.3). However, the flux values derived from the simulation are only higher by a factor of ≈ 10.8 than the mean flux values of region 1, 2, and 3 determined in the *XMM* data analysis. The missing factor of ≈ 2.1 might result from the fact that the simulation describes a superposition of the thermal and the non-thermal component. Also the fact that less hard photons are detected with *eROSITA* than with *XMM-Newton* might influence the value of the flux. An additional factor of uncertainty might be added by the background which was modeled by the simulation software. Finally, the tool for extracting spectra, `makespec`, might also create some bias if it neglects some effects, which

Table 7.1: Best-fit results in the 0.3–10.0 keV band of the simulated all-sky survey spectra for both considered regions. Only the normalizations were left free.

parameter	region 1	region 2
vnei.norm	$(1.66 \pm 0.04) \times 10^{-4}$	$(1.85^{+0.09}_{-0.21}) \times 10^{-5}$
vnei.norm	$< 5.4 \times 10^{-6}$	$< 1.6 \times 10^{-5}$
powerlaw.norm	$(3.74 \pm 0.19) \times 10^{-4}$	$< 1.2 \times 10^{-7}$
red. χ^2 (DoF)	8.095 (1389)	12.542 (618)
flux (0.3–10.0 keV) [10^{-13} erg s $^{-1}$ cm $^{-2}$]	21.38 ± 0.30	1.54 ± 0.09
flux (0.3–2.0 keV) [10^{-13} erg s $^{-1}$ cm $^{-2}$]	$17.86^{+0.29}_{-0.25}$	$1.51^{+0.08}_{-0.9}$

Table 7.2: Best-fit results of the simulated all-sky survey spectra for region 1. In the first case the spectra were fitted simultaneously in the energy range 0.3–10.0 keV and in the second one in the energy band 0.3–2.0 keV. Only the normalizations were left free.

parameter	0.3–10.0 keV	0.3–2.0 keV
vnei.norm	$(1.66 \pm 0.04) \times 10^{-4}$	$(1.71 \pm 0.03) \times 10^{-4}$
vnei.norm	$< 5.4 \times 10^{-6}$	$< 7.03 \times 10^{-6}$
powerlaw.norm	$(3.74 \pm 0.19) \times 10^{-4}$	$(3.08 \pm 0.19) \times 10^{-4}$
red. χ^2 (DoF)	8.095 (1389)	1.369 (532)
flux (0.3–10.0 keV) [10^{-12} erg s $^{-1}$ cm $^{-2}$]	2.138 ± 0.030	2.051 ± 0.029
flux (0.3–2.0 keV) [10^{-12} erg s $^{-1}$ cm $^{-2}$]	$1.786^{+0.029}_{-0.025}$	1.750 ± 0.025

are relevant for survey observations or for extended sources, like vignetting, the PSF, or a correct calculation of the ARF.

Since the background dominates the spectra for energies above ≈ 2 keV, the spectra were also fitted simultaneously in the 0.3–2.0 keV band to draw a comparison to the fit of the whole energy range. The best-fit parameters can be found in Tab. 7.2. This table also shows the best-fit parameters derived for the fit to the energy band 0.3–10.0 keV. There are only slight changes in the parameter values between the two fits. Still the second vnei component is not necessary to describe the data. However, the reduced χ^2 -value is significantly improved compared to the fit to the whole energy band. This indicates that the spectra are well described by the source model in the 0.3–2.0 keV range. It also suggests that the contribution of the background above 2 keV significantly influences the spectral shape and causes the fit to be worse for the whole energy range than restricted to a soft energy band. Nevertheless, the determined fit parameters show a similar confidence level.

Spectral analysis of region 2

Region 2 was chosen to represent a region of the remnant dominated by the non-thermal component following the intention of region 4 of the *XMM-Newton* data analysis. However, as can already be seen in Fig. 7.3 this region is as well dominated by soft photons rather

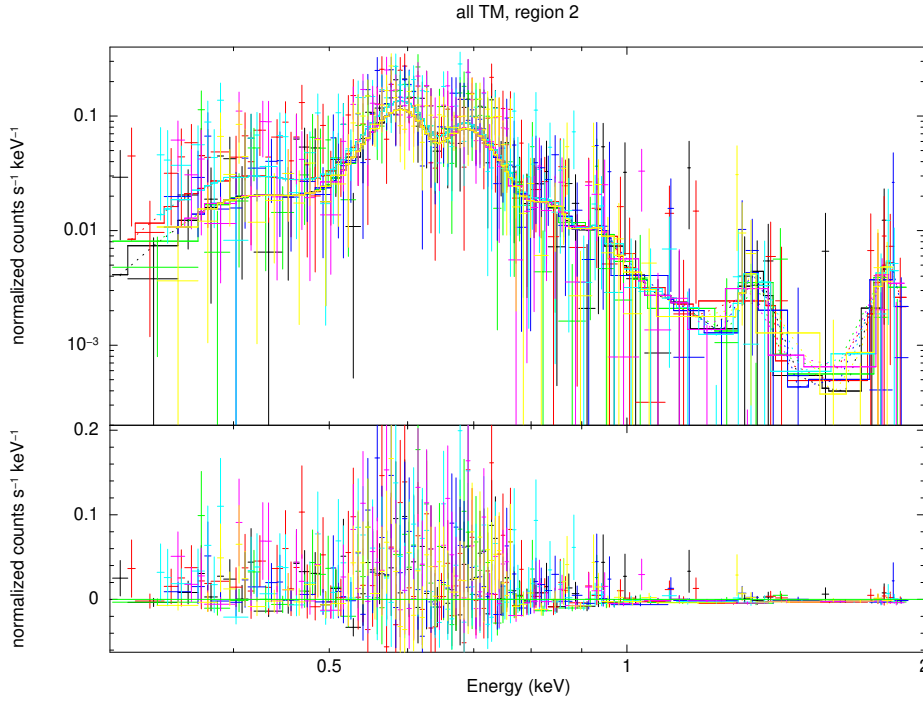


Figure 7.7: Simulated spectra of SNR 1006 of region 2 after four years of *eROSITA* all-sky survey. The data of all TM are shown. The same color coding of the telescope modules is applied as in Fig. 7.6.

than hard ones which is a result of *eROSITA*'s ARF. As already mentioned the size of the region was enhanced compared to the region defined in the *XMM-Newton* data analysis in order to collect an appropriate amount of photons. The same fit model as for region 1 was applied. The source spectra were binned to a minimum of two counts per channel and fitted simultaneously in the 0.3 – 10.0 keV range. To be strict, this rebinning factor does not allow to use the χ^2 -statistic but due to the still small amount of registered photons no better rebinning was possible without a complete loss of the spectral shape. The background subtracted spectra of all telescope modules are shown in Fig. 7.7 together with the best-fit model. The best-fit parameters are listed in Tab. 7.1. The shape of the spectra of region 1 and region 2 is similar, although it is visible that the amount of measured counts in region 2 is less than the one in region 1. The value of the reduced χ^2 of the best-fit for region 2 is even higher than the one of the best-fit of region 1. However, it is not expected to describe the real goodness of the fit since strictly the χ^2 -statistic is not applicable in this case. Only the normalization of the first `vnei` component could be determined well. For the normalizations of the second `vnei` component and the `powerlaw` component only upper limits could be derived. This is in contrast to the case of region 4 of the *XMM-Newton* data analysis, which was dominated by the non-thermal component and where the `powerlaw` component was the strongest compared to the other regions. A possible

explanation why this is not the case for the simulated spectra might be *eROSITA*'s ARF. The effect of the `powerlaw` component is stronger at higher energies than at lower ones. I.e., since the background dominates the simulated spectra for energies above ≈ 2 keV, this component is not as clearly visible as in the *XMM-Newton* spectra. In conclusion due to the poor signal to noise ratio in region 2, the spectra can be modeled with a single `vnei` component.

The absorbed flux values in the 0.3–10.0 keV and in the 0.3–2.0 keV energy bands are consistent with each other. Compared to the flux values of region 1, the values of region 2 are approximately one order of magnitude lower. This is reasonable since the area of region 2 is also smaller than the one of region 1, meaning that the integrated flux of region 2 is smaller as well than the one of region 1. However, the area of region 1 is only by a factor of ≈ 5 bigger than the one of region 2, i.e., a factor of about 2.8 is missing. This difference might result from the fact that the best-fit of region 2 is worse than the one of region 1. In addition, the surface brightness distribution varies between both regions, which does not allow to compare derived flux values easily by scaling with the ratio of the areas of the regions. Compared to the absorbed flux value of region 4 of the *XMM-Newton* data analysis (see Tab. 5.3) the value of region 2 is ≈ 7 times smaller, although its area is ≈ 4.4 times bigger. This difference might result from the fact that less higher energetic photons are registered with the *eROSITA* instrument than with *XMM-Newton*. A second possible explanation lies in the superposition of the thermal and the non-thermal component in the simulations. The non-thermal component was defined for the simulations in the energy range 3.0–5.0 keV, which is dominated by the background in the simulated spectra, i.e., the contribution of the non-thermal emission cannot be fully recovered in the simulated spectra. Consequently, the spectra of region 2 are also dominated by the thermal component. This seems to be in agreement with the derived flux value of region 2, which is comparable to the mean value of the regions in the *XMM-Newton* data analysis, which were dominated by the thermal component (see Tab. 5.3). Nevertheless, the area of region 2 is about 4.5 times higher than the mean of regions 1, 2, and 3 of the *XMM* data analysis, i.e., the integrated flux value should be also higher, which is not the case. But this might be again connected to the fact that the background dominates the simulated spectra for higher energies. Additionally, since again the flux is lower than expected from the *XMM-Newton* data analysis there might be an issue with the extraction tool for the spectra. Furthermore, the surface brightness distribution changes across the remnant which complicates the comparison between different regions and regions of different sizes.

In order to investigate the influence of the background above ≈ 2 keV on the spectra of region 2, a fit in the energy band 0.3–2.0 keV was performed. The resulting best-fit values can be found in Tab. 7.3. Obviously, the parameter values do not change significantly between the fit to the whole energy range and the fit to the restricted one. Additionally, the size of the confidence intervals is on the same order of magnitude as well. The value of the reduced χ^2 is significantly improved for the restricted energy band. However, one should consider that this value does not represent the real goodness of the fit since strictly speaking the χ^2 -statistic is not applicable due to the small rebinning factor.

Comparison of the extraction tools

Finally, a correct energy calibration for the *eROSITA* mission was implemented, which enabled the use of the *eSASS* software. Therefore, it became possible to compare spectra

Table 7.3: Best-fit results of the simulated all-sky survey spectra for region 2. In the first case the spectra were fitted in the energy band 0.3–10.0 keV and in the second one in the energy range 0.3–2.0 keV. Only the normalizations were left free.

parameter	0.3 – 10.0 keV	0.3 – 2.0 keV
vnei.norm	$(1.85^{+0.09}_{-0.21}) \times 10^{-5}$	$(1.91 \pm 0.09) \times 10^{-5}$
vnei.norm	$< 1.6 \times 10^{-5}$	$< 3.636 \times 10^{-6}$
powerlaw.norm	$< 1.2 \times 10^{-7}$	$< 2.35 \times 10^{-7}$
red. χ^2 (DoF)	12.542 (618)	1.247 (545)
flux (0.3–10.0 keV) [10^{-13} erg s $^{-1}$ cm $^{-2}$]	1.54 ± 0.09	1.61 ± 0.08
flux (0.3–2.0 keV) [10^{-13} erg s $^{-1}$ cm $^{-2}$]	$1.51^{+0.08}_{-0.9}$	1.59 ± 0.08

extracted with the tools `makespec` and `srctool`. Fig. 7.8 depicts the case for the background subtracted spectra of region 1 and telescope module 1. For a better comparison the same background file was used for both spectra. In black the spectrum extracted with `makespec` is depicted and in red the one extracted with `srctool`. Both spectra were binned to a minimum of two counts per channel. A rebinning with a minimum of 25 counts per channel could not be achieved for the spectrum extracted with `srctool` without losing information on the spectral shape. This might be explained by the smaller net count rate of only (0.165 ± 0.011) counts per second in contrast to (0.6239 ± 0.0026) counts per second for the spectrum extracted with the tool `makespec`. Furthermore, also the exposure time differs. For the spectrum extracted with `srctool` an exposure time of 2682 s is given, whereas for the spectrum extracted with `makespec` an exposure time of 7611 s is noted. This is a result of `srctool` taking into account effects like vignetting and, therefore, calculating a corrected effective exposure time. Nevertheless, the overall shape of the spectra seems to match although there are minor differences. Fig. 7.9 shows the same situation for a rescaled x-axis and the best-fit model. Like in the spectral analysis of regions 1 and 2 the source was modeled with `tbabs` · (`vnei` + `vnei` + `powerlaw`) and only the normalizations were left free. The spectra of both extraction tools were fitted simultaneously in the 0.3–10.0 keV band. The red. χ^2 value is 2.110 for 964 degrees of freedom (DoF). However, strictly speaking the χ^2 -statistic is not applicable and this value does not represent the real goodness of the fit. In Tab. 7.4 the values of the normalizations are given. The values of the first `vnei` component are in good agreement. The normalizations of the second `vnei` component cannot be determined well, only upper limits can be given. The same applies to the normalization of the `powerlaw` component of the spectrum extracted with `srctool`. There only an upper limit can be determined as well. In contrast, the normalization of the `powerlaw` component of the spectrum extracted with `makespec` can be determined well. These results suggest that the spectrum extracted with `makespec` can be modeled well with a single `vnei` component plus an additional `powerlaw` component, whereas the spectrum extracted with `srctool` can be modeled well with only a single `vnei` component.

As expected the flux values derived for the spectrum extracted with `makespec` are in good agreement with the values derived for region 1 (see Tab. 7.1). The flux values derived from the spectrum extracted with `srctool` are in both, the energy band 0.3–10.0 keV as well as the energy band 0.3–2.0 keV, higher than the values derived for `makespec`. To both

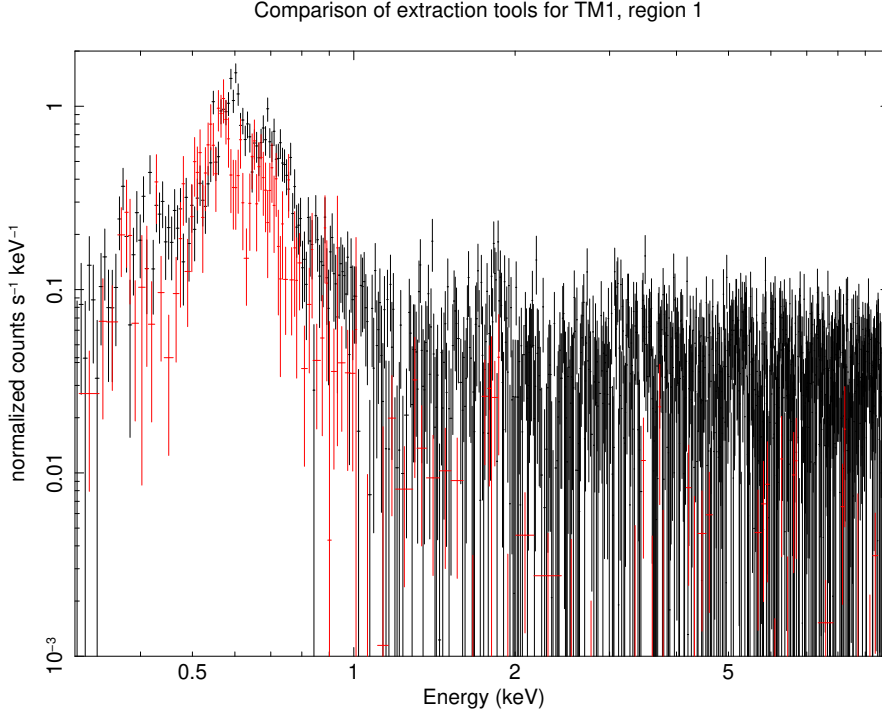


Figure 7.8: Comparison of the extraction tools `makespec` (black) and `srctool` (red). In this case, the spectra of region 1 of TM1 are utilized for the comparison.

extraction tools applies that the flux values in both energy bands are comparable. This is in agreement with the observation that the background dominates the spectra above ≈ 2 keV. Since for the spectrum extracted with `makespec` only one normalization of the model components could not be determined well, the confidence intervals of the flux value are quite narrow. Whereas for the spectrum extracted with `srctool` two normalizations could not be determined well, resulting in wider confidence intervals.

One possible reason for the differences in the spectra is the use of a different ARF file. These files are displayed in Fig. 7.10 for the case of TM1. In black the effective area used by `makespec` and in red the one used by `srctool` are shown. It is clearly visible that they deviate by approximately one order of magnitude. The SIXTE tool `makespec` uses a measured ARF, which is also used by the simulation software. This file does not take into account the PSF or the extent of the source, for instance. In contrast, the ARF file used by `srctool` is also calculated and created by this tool and, therefore, includes these effects. In particular, the eSASS tool `srctool` takes vignetting into account which becomes especially important for survey observations. The effective area of off-axis sources is smaller than the one of on-axis sources. Since in the case of survey observations the source changes its position on the detector, its effective area decreases compared to the case of pointed observations. The ARF used by `makespec` describes the effective area of an on-axis point source and consequently the effective area is higher than the one calculated

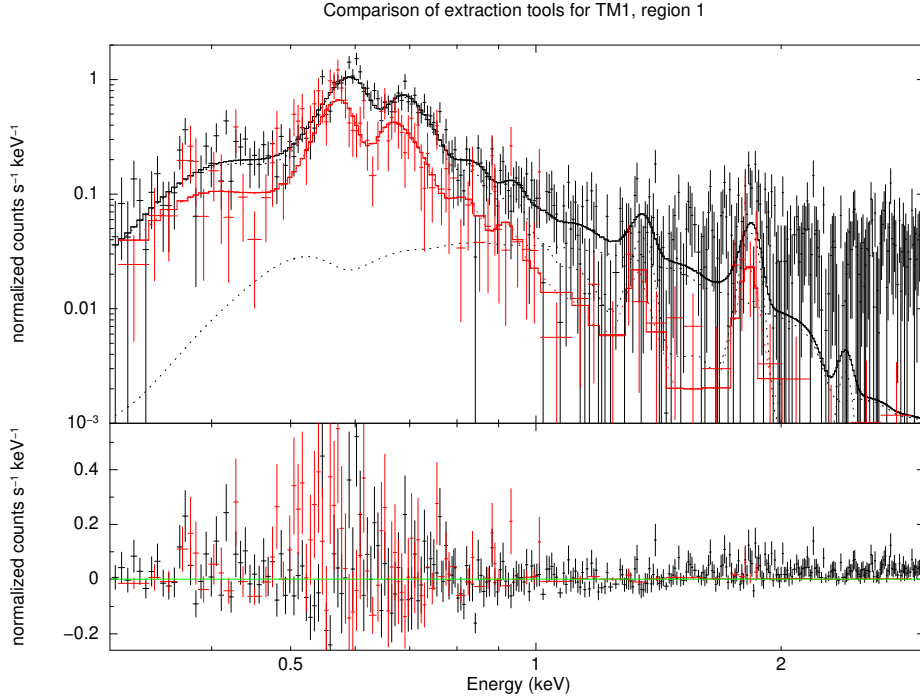


Figure 7.9: Comparison of the extraction tools `makespec` (black) and `srctool` (red) with best-fit models. Like in Fig. 7.8, the spectra of region 1 of TM1 are utilized for the comparison. Only the normalizations of the fit model components were left free. The dotted line represents the `powerlaw` component.

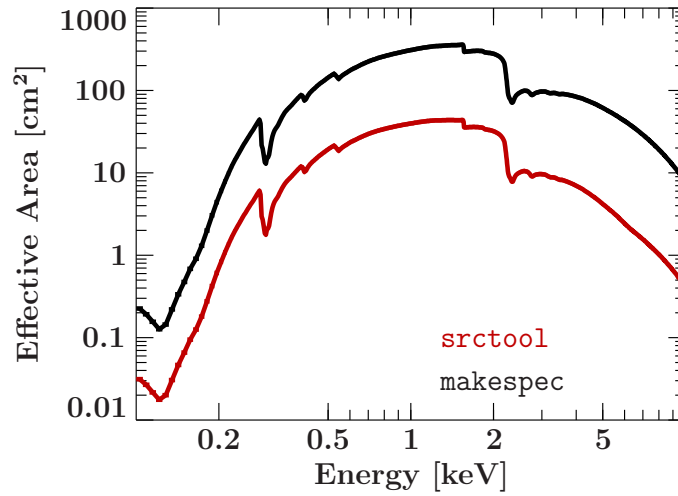
by `srctool` which considers the survey situation. The use of different ARF files influences in particular the normalizations of the spectra.

A second possible reason for the differences in the spectra is the vignetting effect. It does not only influence the effective exposure time and the effective area but can also have direct implications on the spectrum. Since this effect is energy dependent the spectral shape will vary from one extraction tool to the other as the *SIXTE* tool `makespec` does not account for vignetting.

Finally, the absorbed flux value of region 1 of the spectra extracted with `makespec` was approximately 2.1 times less than expected from the *XMM-Newton* data analysis when taking into account the different sizes of the regions. Comparing the value derived for the spectrum extracted with `srctool` with the expectations results in the conclusion that this value is now too high by a factor of ≈ 2.5 . However, since the surface brightness distribution varies over the area of the remnant and the source was simulated as a superposition of the thermal and the non-thermal component, both flux values, the one derived from the spectrum extracted with `makespec` and the one determined from the spectrum extracted with `srctool`, appear reasonable.

Table 7.4: Best-fit results of the comparison of the extraction tools. Only the normalizations were left free.

parameter	makespec	srctool
vnei.norm	$(1.64^{+0.08}_{-0.09}) \times 10^{-4}$	$(7.0^{+0.7}_{-1.0}) \times 10^{-4}$
vnei.norm	$< 5 \times 10^{-5}$	$< 7 \times 10^{-4}$
powerlaw.norm	$(2.2 \pm 0.5) \times 10^{-4}$	$< 2.4 \times 10^{-4}$
flux (0.3–10.0 keV) [10^{-12} erg s $^{-1}$ cm $^{-2}$]	1.83 ± 0.08	$5.9^{+0.6}_{-0.7}$
flux (0.3–2.0 keV) [10^{-12} erg s $^{-1}$ cm $^{-2}$]	1.61 ± 0.07	$5.8^{+0.6}_{-0.7}$

Figure 7.10: Comparison of the effective areas of telescope module 1 resulting from the *srctool* extraction tool in red and the *makespec* tool in black.

7.3.2 Summary of the simulations

To summarize the results from the *eROSITA* all-sky survey simulations, after the first complete all-sky survey with a duration of six months only a small amount of counts will be registered. This would not allow to extract reasonable spectra. Therefore, four years were simulated, the full planned time for the all-sky survey phase. After that time the extraction of reasonable spectra is possible. Two regions were defined, which were expected to be either dominated by the thermal or the non-thermal component. However, it turned out that due to the simulation of a superposition of both components and the effective area of *eROSITA* the non-thermal component is not as strong as it was in the *XMM-Newton* data analysis. Nevertheless, in the region dominated by the thermal component reasonable integrated absorbed flux values could be derived. In contrast, in the region, which was expected to be dominated by the non-thermal component, no good fit could be achieved and the derived flux values are more consistent with the ones from the regions dominated by the thermal component than the region dominated by the non-thermal component of the *XMM-Newton* data analysis. When only considering an energy range of 0.3–2.0 keV for the fit good values for the reduced χ^2 can be reached. However, for region 2 this

statistic is strictly speaking not applicable due to a rebinning to less than 25 counts per channel.

One possibility to improve this behavior is to revise the modelling of the source, i.e., the superposition of the thermal and the non-thermal component. For instance, by defining more than two energy bands, in which the source is described in the SIMPUT file, and by avoiding that more than one source component can be applied to a single position. Moreover, the surface brightness distribution varies across the remnant, i.e., a simple scaling with ratios between different areas does not result in a perfect modelling of the source and should be revised as well.

Finally, the SIXTE tool `makespec` and the eSASS tool `srctool` were compared, which are both intended for the extraction of spectra. The shape of spectra extracted with these tools looks similar although minor deviations are visible. One reason for this different behavior was that the ARF files of the spectra are not identical. Another reason was that the SIXTE tool `makespec` does not take into account vignetting which is of particular importance for survey observations. However, the flux values derived with both extraction tools seem reasonable considering that also the surface brightness distribution changes across the remnant and complicates a direct comparison between different regions and in particular regions of different sizes.

8 Analysis of *eROSITA* data of SNR N132D

8.1 Description of SNR N132D

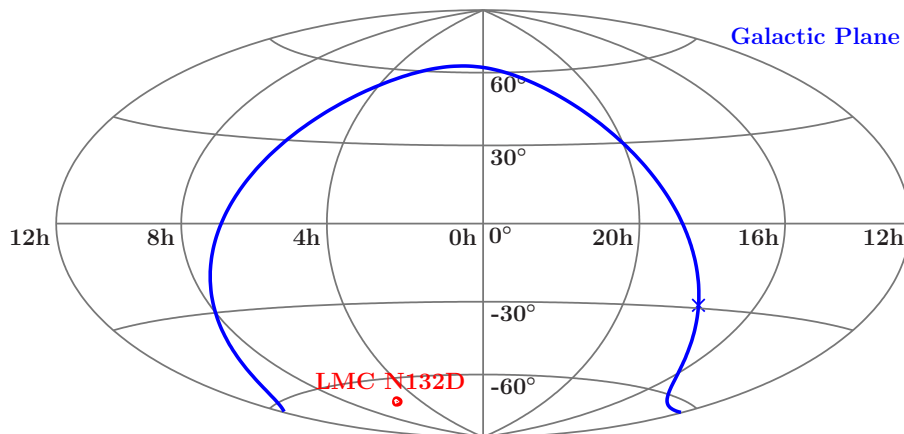


Figure 8.1: Location of SNR LMC N132D on the sky in an equatorial coordinate system. In addition, the Galactic plane is shown in blue.

The supernova remnant N132D is located in the bar of the Large Magellanic Cloud (LMC) (Danziger & Dennefeld, 1976; Lasker, 1978) at the coordinates $RA = 05^{\text{h}} 25^{\text{m}} 02.20^{\text{s}}$ and $Dec = -69^{\circ} 38' 39.0''$ ¹. Its position on the sky is also visualized in Fig. 8.1. It was identified as a supernova remnant by Westerlund & Mathewson (1966). SNR N132D is the brightest supernova remnant in the LMC and belongs to the class of oxygen-rich remnants (Danziger & Dennefeld, 1976; Lasker, 1978). Its progenitor was a massive star with an extensive oxygen-rich mantle, which underwent a core collapse supernova (Blair et al., 2000). Fig. 8.2 shows a tricolor composite X-ray image of SNR N132D taken with *eROSITA*. The shape of the remnant is irregular and resembles a horseshoe. It has a diameter from east to west of about $6'$ and from north to south of about $2'$. It exhibits a circular shape in the south and jet-like structures in the northeast. The circular shape of enhanced thermal X-rays in the south indicates the presence of a dense ambient medium there. Whereas the blown-out morphology in the north suggests a low-density ambient ISM (Bamba et al., 2018). Furthermore, many clumps of X-ray emitting O-ejecta were detected in X-ray observations (Borkowski et al., 2007) that match the optical ejecta morphology (Maggi et al., 2016). Imaging capabilities of better spatial resolution allow to detect bright knots and thin filaments along the shell (Xiao & Chen, 2008). In addition, the shell seems to be a source of both X-ray and synchrotron radio emission (Dickel &

¹<http://simbad.u-strasbg.fr/simbad/sim-basic?Ident=lmc+n132d&submit=SIMBAD+search> (accessed on 2020 April 3)

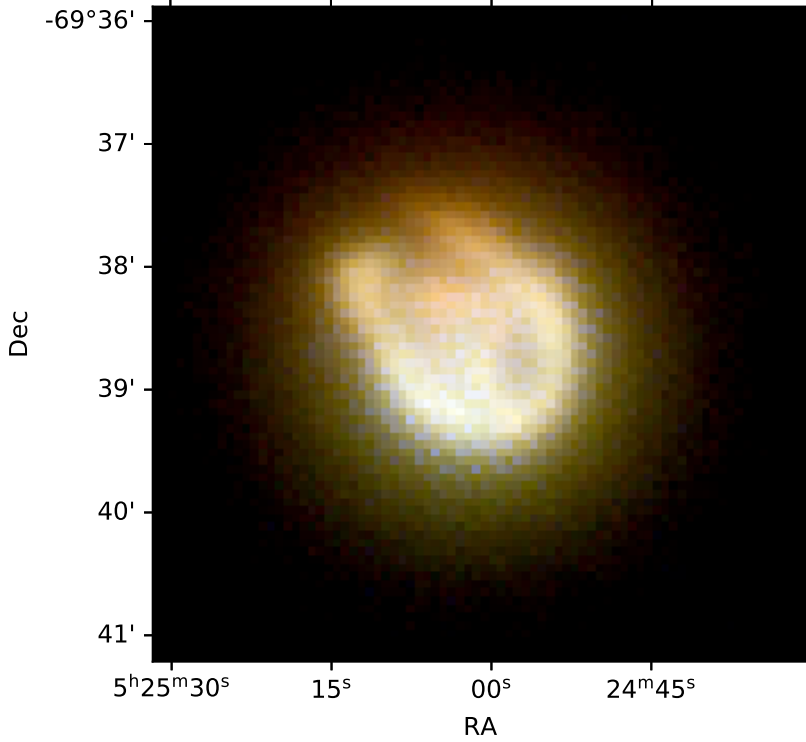


Figure 8.2: RGB image of *eROSITA* data of SNR N132D. Red denotes the energy band 0.3–0.8 keV, green the band 0.8–2.0 keV, and blue 2.0–4.5 keV.

Milne, 1995). Moreover, IR emission from swept-up, shock-heated dust grains was also observed (Tappe et al., 2006). SNR N132D exhibits radiation from GeV and very-high-energy (VHE) γ -rays as well (Ackermann et al., 2016; H. E. S. S. Collaboration et al., 2015), which makes it an energetic cosmic ray accelerator (Bamba et al., 2018). The fact that SNR N132D exhibits GeV and TeV γ -rays indicates that it is a young remnant. In contrast, the spectra of middle-age SNRs are dominated by thermal X-rays and GeV γ -rays. In the case of SNR N132D the shell-like structure is created by a low-temperature component, whereas a recombining component remains in the center of the remnant where a significant Fe Ly α emission line was detected leading to the conclusion that an over-ionized, recombining component is present. These results indicate that the remnant is in a transition stage from a shell-like young SNR to an old one with mixed morphology (Bamba et al., 2018). Vogt & Dopita (2011) determined its age to ≈ 2500 years, i.e., the remnant is assumed to be in the Sedov phase of its evolution.

SNR N132D offers good conditions to study the properties of supernova remnants and to investigate their evolution. Since it is located in the LMC, its distance is well determined and the extinction is low (Xiao & Chen, 2008). Additionally, SNR N132D exhibits several

bright lines while the flux is relatively constant. Therefore, it is often used as a calibration source.

8.2 Observational details and data reduction

During the Calibration and Performance Verification phase (CalPV phase) *eROSITA* observed the supernova remnant N132D several times. In the following the longest of these observations (obsID 700179) is investigated. The observation was performed on 2019 November 22 with a duration of 72 ks. In the course of this thesis the data processing versions 941 and 945 of this observation were studied. Fig. 8.3 shows a tricolor image extracted with the tool `evtool` from the *eROSITA* data of all seven telescopes. As in the *XMM-Newton* data analysis and the *eROSITA* simulations, the soft energy band, symbolized by the red color, is defined in the 0.3–0.8 keV energy range, the intermediate band in green ranges from 0.8 keV to 2.0 keV, and the hard band in blue is given by 2.0–4.5 keV. In the image the supernova remnant can be seen on the left. On the right-hand side of the image the region from which the background spectrum was extracted is shown. The circle around the remnant illustrates the region used for the extraction of the source spectrum. All spectra in this data analysis were extracted with the tool `srctool` of the eSASS package, which was described in Sect. 6.3.

Fig. 8.4 depicts the background subtracted spectra of all seven *eROSITA* telescope modules (TMs) which were binned to a minimum of 50 counts per channel. Obviously, the spectra of TM1–TM4 and TM6 are all in good agreement with each other. However, the spectra of TM5 and TM7 deviate, especially below 0.5 keV, where they show a higher count rate. This is caused by light leakage in these telescopes.

8.3 Light leak in TM5 and TM7

8.3.1 Investigation of the amount of background counts

Unwanted sun light is entering the detectors of TM5 and TM7 leading to an increase in the background. To verify this as the reason for the deviation in the spectra of TM5 and TM7 with respect to the spectra of the other telescopes, the number of background counts in a certain region of the background was determined for all seven telescopes. For simplicity, the same region as used for the extraction of the background spectra was chosen. The results are listed in Tab. 8.1.

The amount of background counts was determined in two energy bands. The amount of counts in the 0.2–10.0 keV energy range provides insights into the strength of the background in general. The amount of counts in the energy range 0.2–0.5 keV allows to draw conclusions on the background behavior in a soft energy range. A combination of both can be used to verify the origin of the spectral behavior as light leakage. As can be seen in Tab. 8.1 TM1, TM2, TM3, and TM4 exhibit a similar low amount of background counts. The value of TM6 is slightly higher but not as high as the values of TM5 and TM7, which show a significantly higher background in both energy bands. The number of background counts is generally higher in the data processing version 945. This can be explained by a change in the exposure times of both data processing versions. For version 941 a corrected effective exposure time of 55 ks is noted and for version 945 it is 59 ks

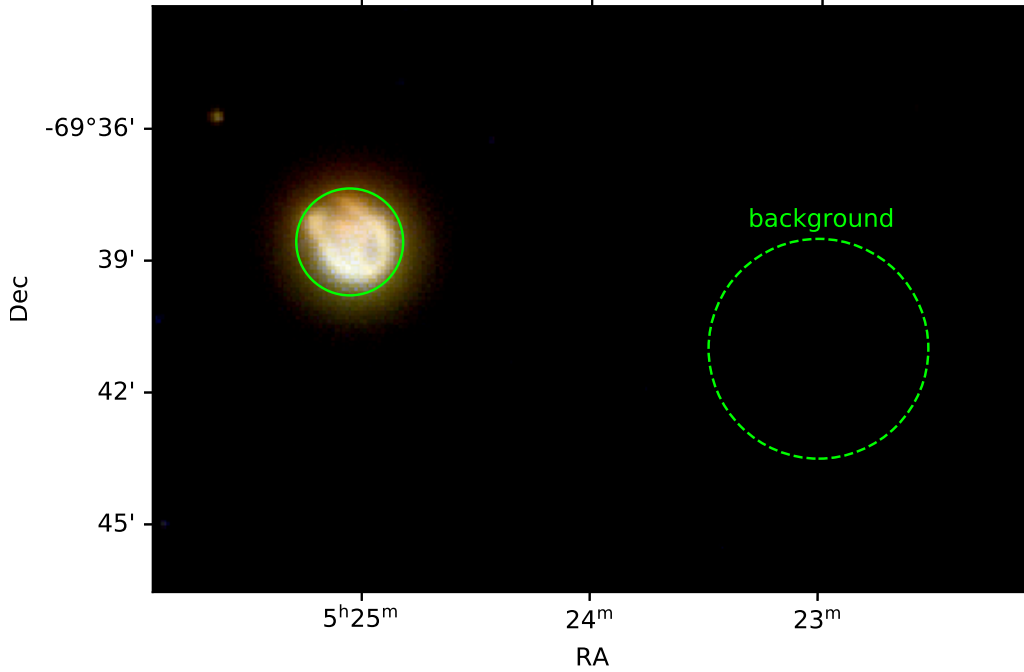


Figure 8.3: RGB image of SNR N132D (processing version 945). Red denotes the energy band 0.3–0.8 keV, green the band 0.8–2.0 keV, and blue 2.0–4.5 keV. Furthermore, the regions from which the source spectrum and the background spectrum were extracted are plotted.

corresponding to an increase of approximately 4 ks. If a higher fraction of the observation of SNR N132D is usable, i.e., the effective exposure time is increased, then also a higher number of background counts will be registered.

For the processing version 941 of the data the lowest amount of background counts is determined in TM3, whereas TM7 shows the highest. This applies to both energy bands. In the case of processing version 945 TM2 shows the lowest amount of background counts in the 0.2–10.0 keV range and TM3 in the soft energy band. Again, TM7 exhibits the highest number of background counts in both energy bands. Taking the ratio of the number of background counts in TM7 and TM3 allows to investigate the strongest deviation between all telescope modules for processing version 941. In the 0.2–10.0 keV band the ratio TM7/TM3 is approximately 1.11 ± 0.03 , meaning that the background of TM7 is enhanced by 11% with respect to that of TM3. In the soft band from 0.2 keV to 0.5 keV, the ratio is even higher. Here, TM7/TM3 is approximately 1.55 ± 0.09 , meaning that the background is enhanced by even more than one half of the amount of the background of TM3. For the data processing version 945 the situation is similar. In order to investigate the strongest

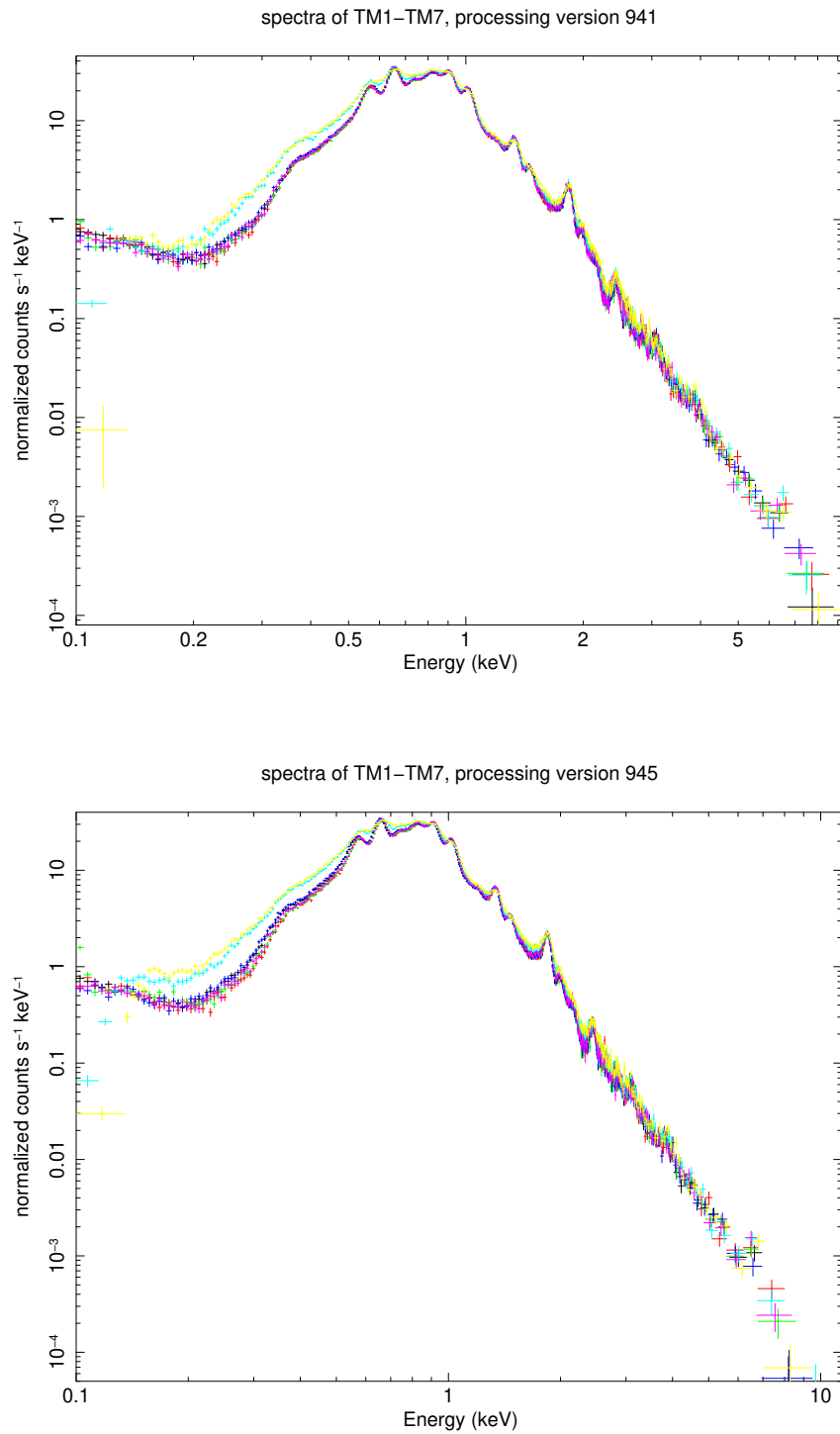


Figure 8.4: Spectra of SNR N132D of all seven *eROSITA* telescopes (TM1: black, TM2: red, TM3: green, TM4: blue, TM5: cyan, TM6: magenta, TM7: yellow). The data of processing version 941 are shown at the top and the data of processing version 945 at the bottom.

Table 8.1: Amount of counts in the background region for each telescope module (TM) in two energy bands for both processing versions of the data.

TM	processing version 941		processing version 945	
	0.2 – 10.0 keV	0.2 – 0.5 keV	0.2 – 10.0 keV	0.2 – 0.5 keV
TM1	4142 ± 65	534 ± 24	4448 ± 67	610 ± 25
TM2	4137 ± 65	563 ± 24	4322 ± 66	588 ± 25
TM3	4010 ± 64	519 ± 23	4337 ± 66	570 ± 24
TM4	4198 ± 65	524 ± 23	4526 ± 68	576 ± 24
TM5	4410 ± 67	750 ± 28	4691 ± 69	796 ± 29
TM6	4299 ± 66	637 ± 26	4625 ± 69	693 ± 27
TM7	4435 ± 67	805 ± 29	4803 ± 70	897 ± 30

Table 8.2: Ratios of the telescope module with the highest amount of background counts and the one with the lowest amount of background counts for both data processing versions in two energy bands.

ratio	0.2 – 10.0 keV	0.2 – 0.5 keV
	processing version 941	
TM7/TM3	1.11 ± 0.03	1.55 ± 0.09
	processing version 945	
TM7/TM2	1.11 ± 0.03	1.53 ± 0.09

deviation between all telescope modules the ratio TM7/TM2 is determined. For the 0.2–10.0 keV energy band this ratio yields 1.11 ± 0.03 , i.e., the background of TM7 is also enhanced by 11% compared to that of TM2. For the soft band from 0.2 keV to 0.5 keV the same ratio is calculated although here TM3 exhibits the lowest amount of background counts. For processing version 945 the ratio TM7/TM2 yields a value of approximately 1.53 ± 0.09 in the soft energy band, i.e., the background of TM7 is again enhanced by even more than one half of the amount of background of TM2. The results of these considerations are also summarized in Tab. 8.2. To conclude, the strongest deviation between all telescopes is an enhancement of background counts by approximately 10% in the range 0.2–10.0 keV, whereas the increase in the 0.2–0.5 keV band is more than 50%, i.e., the soft energy band shows a significantly stronger deviation in the background counts.

Table 8.3: Mean values of the background counts of TM1–TM4 as well as the ratios between TM5, TM6, and TM7, respectively, with these mean values for both data processing versions in two energy bands.

	processing version 941		processing version 945	
	0.2 – 10.0 keV	0.2 – 0.5 keV	0.2 – 10.0 keV	0.2 – 0.5 keV
mean TM1 – TM4	4122 ± 33	535 ± 12	4408 ± 34	586 ± 13
TM5/mean	1.070 ± 0.019	1.40 ± 0.07	1.064 ± 0.018	1.36 ± 0.06
TM6/mean	1.044 ± 0.018	1.19 ± 0.06	1.049 ± 0.018	1.18 ± 0.06
TM7/mean	1.076 ± 0.019	1.50 ± 0.07	1.090 ± 0.018	1.53 ± 0.07

To draw further conclusions on the background behavior of the individual telescope modules, a mean value of the number of counts in the background region is calculated for TM1–TM4. Furthermore, this will answer the question whether the enhanced background of TM6 is stronger in the soft energy regime as well. An overview of the determined mean values and ratios is provided in Tab. 8.3. For the data processing version 941 a mean value of (4122 ± 33) background counts was determined for TM1–TM4 in the energy band 0.2–10.0 keV and a value of (535 ± 12) counts for 0.2–0.5 keV. In the energy range 0.2–10.0 keV the value of TM5 is enhanced by $(7.0 \pm 1.9)\%$ compared to the mean value. For TM6 the factor is $(4.4 \pm 1.8)\%$ which is slightly smaller, whereas TM7 shows the greatest enhancement with a factor of $(7.6 \pm 1.9)\%$. In the soft energy band the increase is even higher for all three telescope modules. Here, TM5 has an increased background by a factor of $(40 \pm 7)\%$ compared to the mean of TM1–TM4. For TM6 the factor is $(19 \pm 6)\%$ which is significantly smaller. The highest value is again reached for TM7 with an increase by $(50 \pm 7)\%$. In summary, for the processing version 941 TM5 and TM7 exhibit an enhancement in the background counts which is significantly stronger in the soft band. In contrast, for TM6 the increase in the number of background counts is stronger in the soft energy regime as well but not as pronounced as for TM5 and TM7.

For the data processing version 945 the mean values of TM1–TM4 yield (4408 ± 34) and (586 ± 13) counts in the bands 0.2–10.0 keV and 0.2–0.5 keV, respectively. For TM5 this results in an enhancement of $(6.4 \pm 1.8)\%$ in the range 0.2–10.0 keV. TM6 shows an increase of $(4.9 \pm 1.8)\%$, whereas the background of TM7 is enhanced by $(9.0 \pm 1.8)\%$. Again the increase is stronger in the energy range 0.2–0.5 keV for all three telescope modules. For TM5 the background is increased by $(36 \pm 6)\%$. For TM6 the value is $(18 \pm 6)\%$ and for TM7 $(53 \pm 7)\%$. In summary, for the data processing version 945 the increase in background counts is stronger for TM5, TM6, and TM7 in the soft energy band than in the range 0.2–10.0 keV. However, the enhancement for TM6 is not as pronounced as for the other two telescope modules. The factors by which the amount of background counts are increased vary only slightly from one processing version to another. Therefore, the background is not only in general higher in TM5 and TM7 than in the other telescope modules, but especially below 0.5 keV, which explains the higher count rates in the spectra of TM5 and TM7 below 0.5 keV compared to those of the other telescopes. To conclude, the deviations in the spectra indeed originate from a light leak in TM5 and TM7. If TM6 is also affected by light leakage this effect is at least not as pronounced as it is for TM5 and TM7.

8.3.2 Influence on the background spectra

The different strength of the background can even be seen in the background spectra of the individual telescope modules. Fig. 8.5 shows a comparison between the background spectra of the telescope module with the lowest background, TM3, in black and the telescope module with the highest background, TM7, in red. At the top the results of the processing version 941 are shown and at the bottom the ones for the processing version 945. All spectra were binned to a minimum of 50 counts per channel. A strong deviation in the spectra of TM3 and TM7 below 0.2 keV is clearly visible. Additionally, up to ≈ 0.6 keV TM7 shows an enhanced background contribution compared to TM3. Above this energy the background contamination is on a similar level. This means that the background contribution of TM7 is not only on a constant higher level than the one of TM3 but it

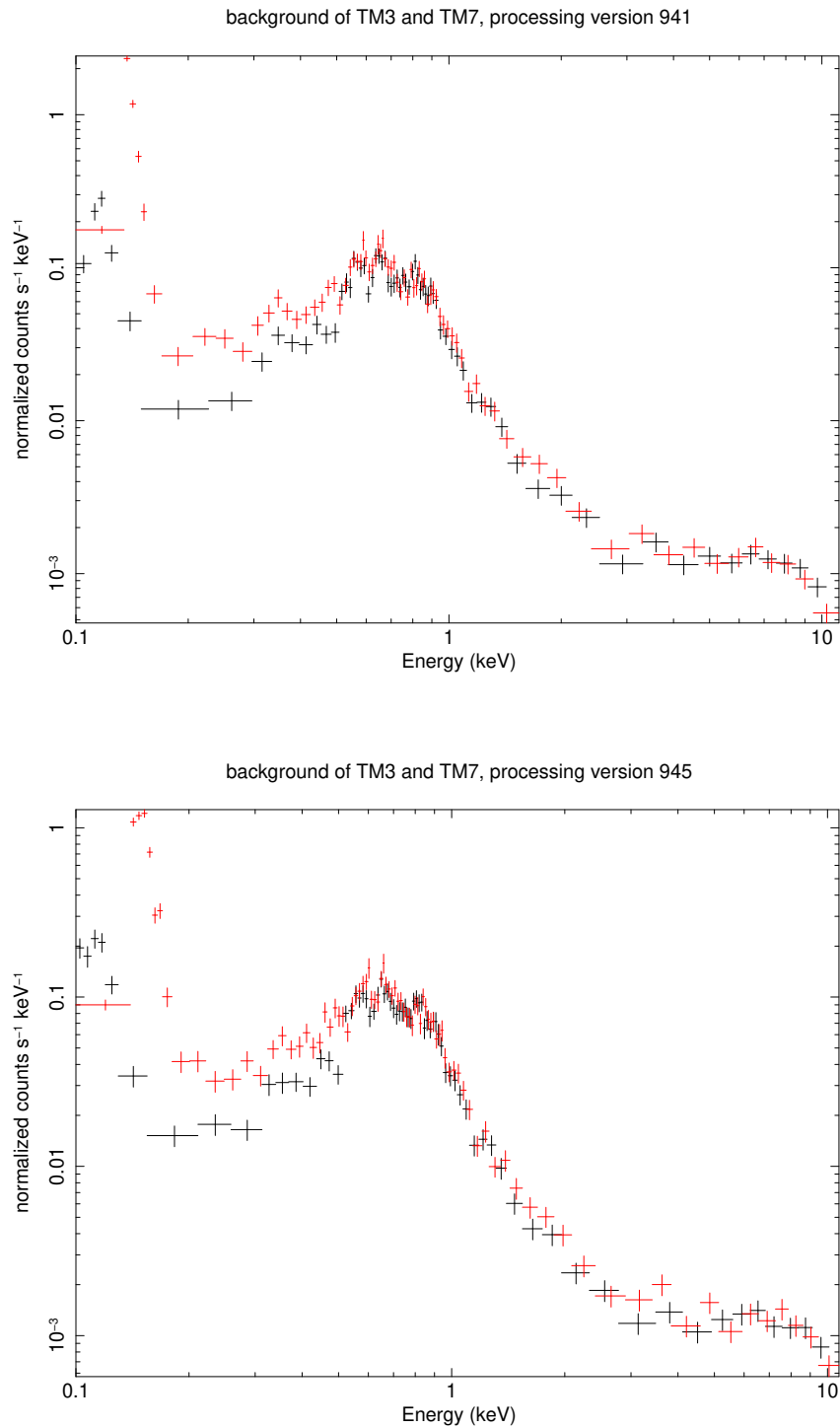


Figure 8.5: Background spectra of TM3 in black and TM7 in red (top: processing version 941, bottom: processing version 945). All spectra are rebinned to a minimum number of 50 counts per channel.

Table 8.4: Count rate in counts per second of the background subtracted source spectra for each telescope module in the energy range 0.2–0.5 keV for both data processing versions.

TM	processing version 941	processing version 945
TM1	1.012 ± 0.005	1.039 ± 0.005
TM2	0.993 ± 0.005	0.922 ± 0.004
TM3	0.990 ± 0.005	0.938 ± 0.004
TM4	1.048 ± 0.005	1.082 ± 0.005
TM5	1.470 ± 0.005	1.534 ± 0.006
TM6	1.025 ± 0.005	0.972 ± 0.005
TM7	1.549 ± 0.005	1.639 ± 0.006

Table 8.5: Mean values of the count rate of TM1, TM2, TM3, TM4, and TM6 in counts per second as well as the ratios between TM5, TM6, and TM7, respectively, with these mean values for both data processing versions in the energy band 0.2–0.5 keV.

	processing version 941	processing version 945
mean	1.014 ± 0.005	0.991 ± 0.011
TM5/mean	1.450 ± 0.008	1.548 ± 0.013
TM7/mean	1.528 ± 0.009	1.654 ± 0.013

is especially enhanced for lower energies indicating a light leak in TM7. The background spectra of TM1, TM2, TM4, and TM6 look similar to the one of TM3, whereas the background spectrum of TM5 exhibits the same trend as the one of TM7 but slightly less strong.

8.3.3 Estimating the influence of the light leak on the flux

In order to estimate the influence of the light leak on flux values determined for each telescope module individually, the count rate in the background subtracted source spectra is determined in the energy range 0.2–0.5 keV. The resulting values can be found in Tab. 8.4. Obviously, the count rates of TM1, TM2, TM3, TM4, and TM6 are similar to each other, whereas the count rates of TM5 and TM7 deviate significantly from the others. To predict the excess in flux, which will result from the light leak in TM5 and TM7, the count rates of TM5 and TM7 are compared to those of the other telescope modules. Therefore, a mean count rate value for TM1, TM2, TM3, TM4, and TM6 is calculated. For the processing version 941 the value of this mean count rate is (1.014 ± 0.005) counts per second. The ratio between the count rate of TM5 and this mean count rate is determined to be 1.450 ± 0.008 , which means that the count rate of TM5 is about 45% higher than the mean value of the telescope modules without light leakage. For TM7 this effect is even stronger. Here, the ratio between the count rate of TM7 and the mean count rate of the unaffected telescope modules is 1.528 ± 0.009 , which means the count rate of TM7 is over 50% higher than the mean value of the telescopes which do not experience light leakage. The results are also summarized in Tab. 8.5.

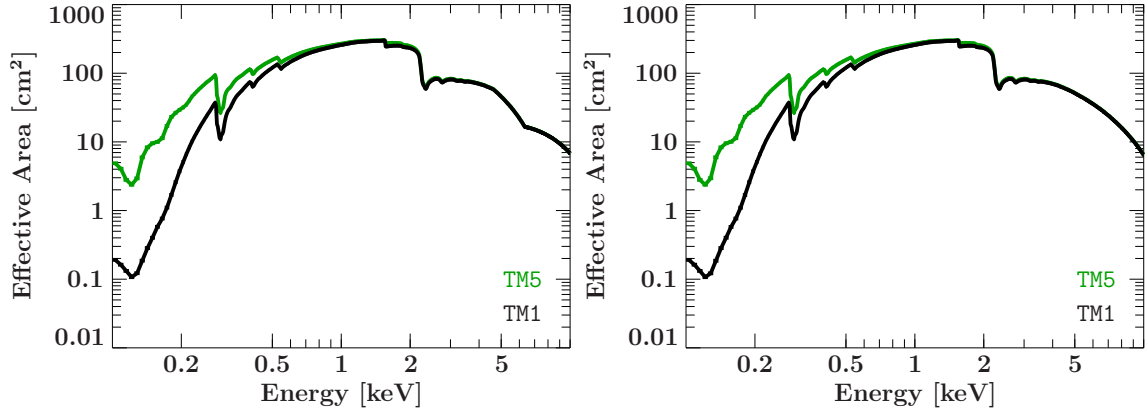


Figure 8.6: Comparison of the effective areas used for TM1 (black) and TM5 (green) for the processing version 941 (left) and the processing version 945 (right). The effective areas of TM2, TM3, TM4, and TM6 are identical with the one of TM1, whereas the effective area of TM7 is identical with the one of TM5.

For the data processing version 945 this deviation is even stronger. Here, the mean count rate of TM1, TM2, TM3, TM4, and TM6 yields a value of (0.991 ± 0.011) counts per second, which is slightly less than the one determined for processing version 941. The ratio between the count rate of TM5 and this mean count rate is determined to be 1.548 ± 0.013 , which means that the count rate of TM5 is about 55% higher than the mean value of the telescope modules without light leakage. For TM7 this effect is again even more pronounced. Here, the ratio between the count rate of TM7 and the mean count rate of the unaffected telescope modules is 1.654 ± 0.013 , which means the count rate of TM7 is over 65% higher than the mean value of the telescopes which do not experience light leakage. These values are even higher than in the processing version 941. To conclude, the light leak in TM5 and TM7 has a significant effect on the count rate measured with these two telescope modules in the energy range 0.2–0.5 keV. This also translates to enhanced flux values derived for these telescope modules. Therefore, one needs to be careful when analyzing spectra measured with TM5 and TM7 of the *eROSITA* mission.

8.3.4 Possible reason for the light leakage

One possible reason why TM5 and TM7 are affected by light leakage is that these telescope modules do not possess on-chip filters for blocking optical light, whereas the others do. This is also reflected in the effective area. As can be seen in Fig. 8.6 the effective area of TM5 is increased below ≈ 0.6 keV compared to the one of TM1. This applies to both data processing versions. The effective areas of TM2, TM3, TM4, and TM6 are identical to the one of TM1, which is shown in black in Fig. 8.6, whereas the one of TM7 is identical to the one of TM5, which is shown in green in Fig. 8.6, i.e., also shows an increase below ≈ 0.6 keV. Therefore, the implementation of on-chip filters reduced the effective area for soft photons.

As already apparent from Fig. 8.6 there is a difference in the effective areas of both data processing versions which is even more clear from Fig. 8.7. Here, the ARF of TM1 of the data processing version 941 is shown in red and the one of the data processing version

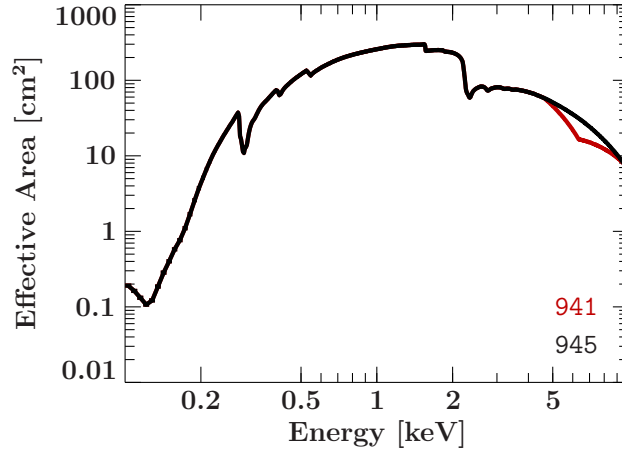


Figure 8.7: Comparison of the ARFs of TM1 of the two processing versions. The data processing version 941 is depicted in red and the processing version 945 in black.

945 in black. The effective area of the processing version 941 exhibits a dip around 6 keV. However, this is the only deviation between the two ARF files.

8.4 Spectral analysis of the individual telescope modules

8.4.1 Contribution of the background

To account for the different spectral behavior and to further investigate potential differences between the *eROSITA* telescope modules, the spectra were not analyzed simultaneously but individually and in groups of two, respectively. Beforehand, the influence of the background on the source spectrum is studied. In Sect. 7.3.1 it was shown that the simulated spectra of SNR 1006 for four years of all-sky survey observations were dominated by the background contribution for energies above ≈ 2 keV. To explore if this is also the case for a pointed observation of SNR N132D, the source spectra and background spectra of TM3 and TM7 for the processing version 941 and the ones of TM2 and TM7 for the processing version 945 are depicted in Fig. 8.8 and Fig. 8.9, respectively. Note that the background spectra are scaled in order to account for the different sizes of the source and background areas. From these figures it is visible that the background contribution dominates the spectra only above ≈ 6 keV. This applies to both the telescope module with the lowest background contribution, TM3 and TM2, respectively, and the telescope module with the highest background contribution, TM7. Therefore, restricting a spectral fit to a soft energy band would not improve the fit in the case of SNR N132D. Since the effective exposure time of this pointed observation is higher than the one of the simulated all-sky survey spectra of SNR 1006, more photons are registered improving the signal to noise ratio and, therefore, reducing the contribution of the background to the spectra.

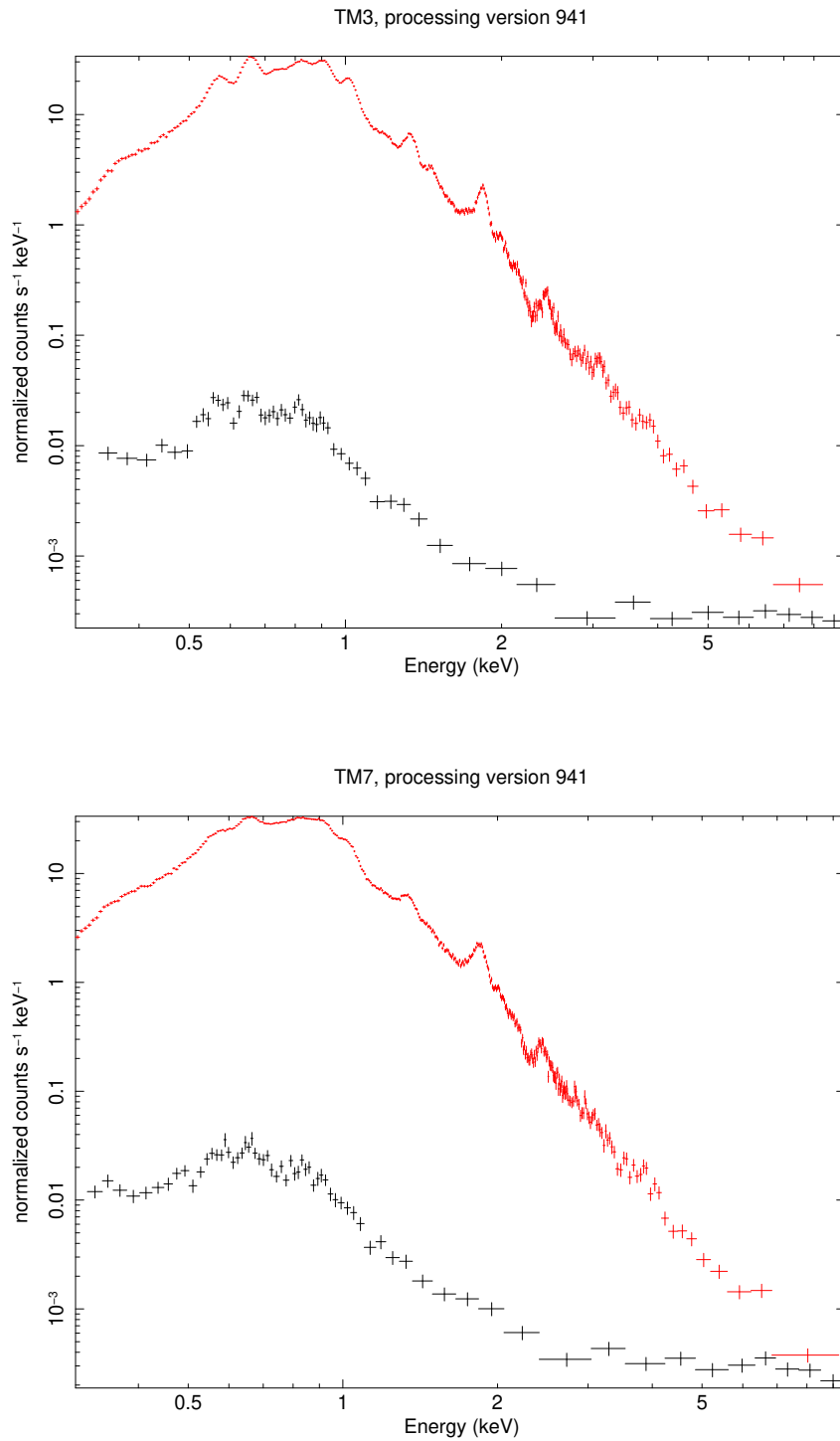


Figure 8.8: Contribution of the background to the spectra of TM3 (top) and TM7 (bottom). Both describe the case of processing version 941. The source spectra are depicted in red and the background spectra in black. Note that the background spectra were scaled to account for the different sizes of source and background area.

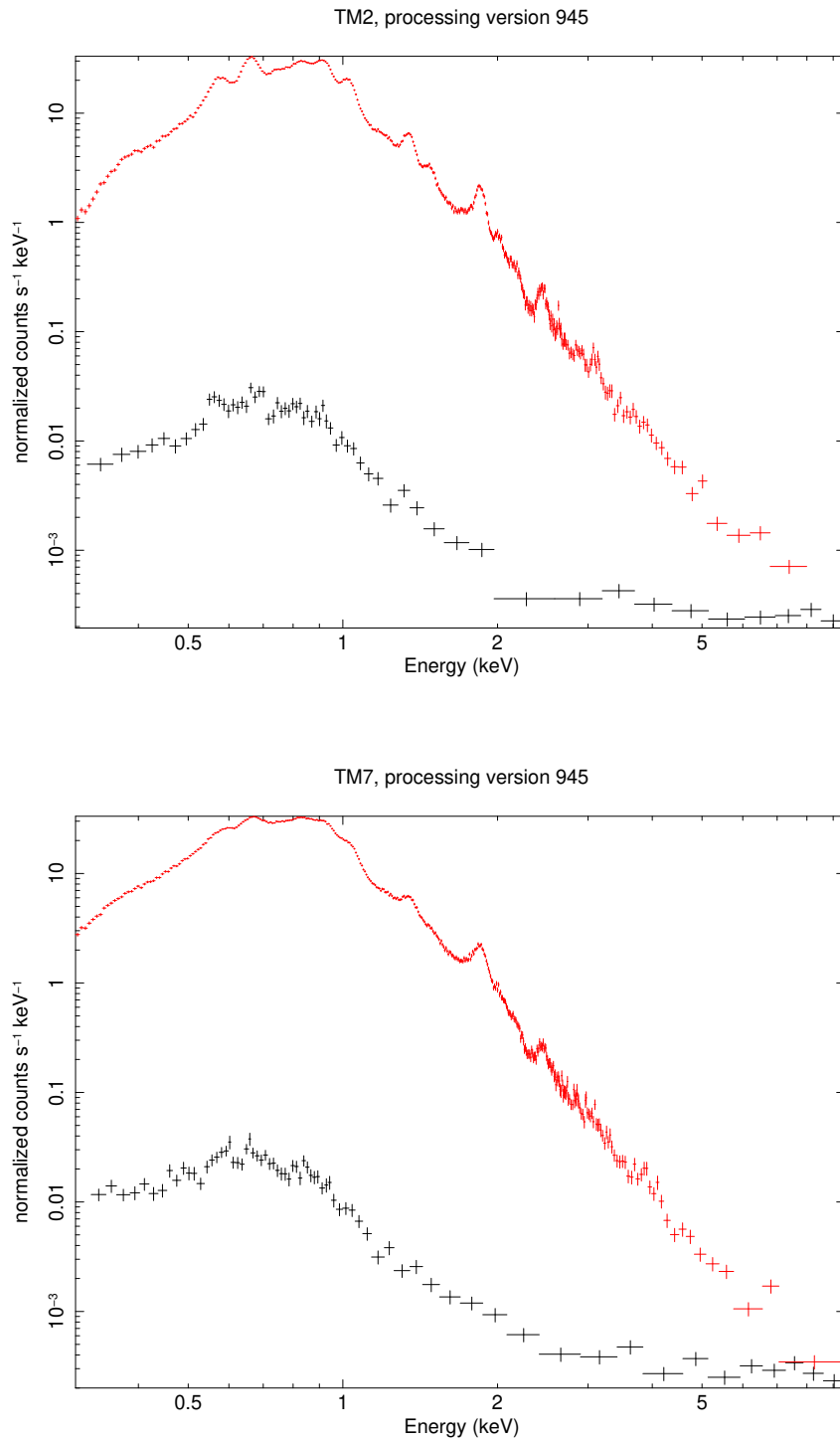


Figure 8.9: Contribution of the background to the spectra of TM2 (top) and TM7 (bottom). Both describe the case of processing version 945. The source spectra are depicted in red and the background spectra in black. Note that the background spectra were scaled to account for the different sizes of source and background area.

8.4.2 Spectral analysis

The spectra of all seven telescope modules were extracted using the eSASS tool `srctool` and rebinned to a minimum of 50 counts per channel. As is already apparent from Fig. 8.4 the spectra of the individual TMs are not identical. The most striking discrepancy can be seen for the spectra of TM5 and TM7, which do not possess an on-chip filter, with respect to the spectra of the other five telescope modules, which do have this kind of filter. Nevertheless, a closer look at the spectra of the TMs with an on-chip filter revealed that these also exhibit some deviations. Therefore, groups of up to two telescope modules were formed whose spectra were fit simultaneously as the differences in the spectra within one of these groups were almost negligible. In particular, TM1 and TM4 were fit simultaneously as well as TM2 and TM3, whereas TM6 was fit individually since its spectrum deviated from all the others. In addition, the two telescope modules exposed to light leakage, TM5 and TM7, were fit simultaneously although differences between their spectra are visible.

A fit model of the form `tbvarabs · tbabs · (vnei + vnei + powerlaw)` was chosen for the fits of all background subtracted spectra. Similar to the `tbabs` model the `tbvarabs` model belongs to the group of Tuebingen-Boulder ISM absorption models. These include X-ray absorption by the gas-phase ISM, the grain-phase ISM, as well as the molecules in the ISM. In contrast to the `tbabs` model which allows the user only to vary the hydrogen column, the `tbvarabs` model allows the user to additionally vary the elemental abundances and the redshift².

The `tbabs` component of the fit model accounts for the X-ray absorption by the Galactic interstellar medium between the LMC and the observer, whereas the `tbvarabs` component describes the absorption inside the LMC itself. Therefore, the value of the hydrogen column of the `tbabs` component was frozen to $6.22 \times 10^{20} \text{ cm}^{-2}$, which was determined with the help of the program `nh` at the position of the remnant. In contrast, the equivalent hydrogen column of the `tbvarabs` component (`tbvarabs.nH`) was allowed to vary. However, the metal abundances of this model component were frozen to the value of the metallicity of the LMC which is 0.5 solar. Furthermore, a molecular hydrogen column of $0.2 \times 10^{22} \text{ cm}^{-2}$ was assumed. The grain density was frozen to 1 g cm^{-3} and the grain minimum and maximum sizes to $0.025 \mu\text{m}$ and $0.25 \mu\text{m}$, respectively. The powerlaw index of grain sizes was set to 3.5 and the grain depletion fractions of all elements were frozen to 1. The redshift of the `tbvarabs` component was frozen to 0.

The first `vnei` component represents the non-equilibrium ionization collisional plasma of the ambient interstellar medium of the remnant, whereas the second `vnei` component describes the non-equilibrium ionization collisional plasma of the ejected material by the supernova. Therefore, the metal abundances of the first `vnei` component were frozen to the metallicity of the Large Magellanic Cloud, i.e., to 0.5 solar. Only the plasma temperature (`vnei.kT`), the ionization timescale (`vnei.Tau`), the redshift (`vnei.Redshift`), and the normalization (`vnei.norm`) of this first component were allowed to vary. For the second `vnei` component, which describes the ejecta, the same parameters were free as already for the first `vnei` component. In addition to that also the abundances of oxygen (`vnei.O`), neon (`vnei.Ne`), magnesium (`vnei.Mg`), silicon (`vnei.Si`), sulfur (`vnei.S`), iron (`vnei.Fe`), and nickel (`vnei.Ni`) were allowed to vary. The abundances of carbon, nitrogen, argon, and calcium were frozen to 0.5 solar.

²<https://heasarc.gsfc.nasa.gov/xanadu/xspec/manual/node265.html> (accessed on 2020 May 1)

The `powerlaw` component represents non-thermal emission from the supernova remnant. Here, both parameters were allowed to vary, the photon index (`powerlaw.PhoIndex`) and the normalization (`powerlaw.norm`).

In the case of fitting two spectra simultaneously all parameters of the second spectrum were tied to the ones of the first spectrum. All spectra were fitted in the energy range 0.3–10.0 keV. For the spectral analysis only the spectra of the data processing version 945 were considered. The best-fit parameters for all telescope modules can be found in Tab. 8.6. The background subtracted source spectra of TM1 (black) and TM4 (red) with the best-fit model are depicted in the upper panel of Fig. 8.10, whereas the lower panel of Fig. 8.10 shows the same for TM2 (black) and TM3 (red). The background subtracted source spectrum of TM6 is given in the upper panel of Fig. 8.11 together with the best-fit model. Finally, the background subtracted source spectra of TM5 (black) and TM7 (red) together with the best-fit model are presented in the lower panel of Fig. 8.11.

As can already be seen from the residuals in Fig. 8.11 the spectra of TM5 and TM7 also deviate from each other. This suggests that the effect of the light leak varies between both telescopes and also leads to the worst reduced χ^2 value of all four best-fits to the data of SNR N132D (see Tab. 8.6). However, also for the best-fits to the other telescope modules no good fit could be reached. The smallest reduced χ^2 value was achieved for TM1 and TM4.

In general, the best-fit parameters of TM1 and TM4 as well as TM2 and TM3 as well as TM6 are quite similar although some parameters deviate significantly. In contrast, most of the best-fit parameters derived for TM5 and TM7 are significantly different compared to the ones of the telescope modules with an on-chip filter. Therefore, it will be investigated for which parameters the individual telescope modules are consistent with each other and for which parameters not.

Consistent best-fit parameters

Some of the best-fit parameters are consistent for TM1, TM2, TM3, TM4, and TM6 but deviate for TM5 and TM7. Nevertheless, the equivalent hydrogen column `tbvarabs.nH` is one of the parameters that are consistent for all telescope modules because it does not vary strongly between all best-fit results and is in the range of $\approx 6 \times 10^{22} \text{ cm}^{-2}$ up to $\approx 8 \times 10^{22} \text{ cm}^{-2}$.

Considering the `vnei` component describing the ejecta the plasma temperature (`vnei.kT`) is also quite similar for all telescope modules with a value around 0.75 keV. The same applies to the ionization timescale (`vnei.Tau`) of the ejecta component which is on the same order of magnitude for all telescope modules. It ranges from $\approx 3 \times 10^{11} \text{ s cm}^{-3}$ (TM5, TM7) via $\approx 5.5 \times 10^{11} \text{ s cm}^{-3}$ (TM1, TM4, TM6) up to $\approx 7 \times 10^{11} \text{ s cm}^{-3}$ (TM2, TM3). Additionally, the normalization of this component (`vnei.norm`) is also on the same order of magnitude for all telescope modules, namely $\approx 5 \times 10^{-2}$.

The `powerlaw` photon index (`powerlaw.PhoIndex`) of all telescope modules is also rather similar and ranges from ≈ 3 to ≈ 3.5 . Finally, the normalization of the `powerlaw` component (`powerlaw.norm`) lies between $\approx 2 \times 10^{-3}$ and $\approx 7 \times 10^{-3}$, i.e., it is also on the same order of magnitude for all telescope modules.

Furthermore, the absorbed flux values derived in the energy band 0.3–10.0 keV are all rather similar to each other with a value of $\approx 1.28 \times 10^{10} \text{ erg s}^{-1} \text{ cm}^{-2}$. The lowest flux was determined for TM2 and TM3, whereas the highest flux was measured for TM5 and

Table 8.6: Best-fit parameters of the spectral fits of the SNR N132D (processing version 945). The single telescope modules were either fitted individually or simultaneously in pairs of two. The absorbed flux was derived in the energy band 0.3–10.0 keV.

parameter	TM1, TM4	TM2, TM3	TM6	TM5, TM7
tbvarabs.nH [10^{22} cm^{-2}]	$(6.18 \pm 0.04) \times 10^{-2}$	$(8.14^{+0.05}_{-0.024}) \times 10^{-2}$	$(7.14^{+0.06}_{-0.05}) \times 10^{-2}$	$(6.44^{+0.027}_{-0.04}) \times 10^{-2}$
vnei.kT [keV]	2.74 ± 0.06	$3.00^{+0.12}_{-0.06}$	$2.32^{+0.06}_{-0.07}$	$0.2868^{+0.0008}_{-0.00016}$
vnei.Tau [s cm^{-3}]	$(5.01^{+0.04}_{-0.027}) \times 10^9$	$(4.52^{+0.04}_{-0.028}) \times 10^9$	$(5.42 \pm 0.05) \times 10^9$	$(1.146^{+0.007}_{-0.011}) \times 10^{11}$
vnei.Redshift	$(4.22^{+0.10}_{-0.006}) \times 10^{-3}$	$(-6.764^{+0.011}_{-0.021}) \times 10^{-3}$	$(-6.78^{+0.028}_{-0.06}) \times 10^{-3}$	$(-2.9627^{+0.0018}_{-0.0007}) \times 10^{-2}$
vnei.norm	$(6.613 \pm 0.023) \times 10^{-3}$	$(6.18^{+0.015}_{-0.04}) \times 10^{-3}$	$(6.55^{+0.026}_{-0.04}) \times 10^{-3}$	$(2.293^{+0.010}_{-0.007}) \times 10^{-2}$
vnei.kT [keV]	$0.7540^{+0.0009}_{-0.000013}$	$0.7353^{+0.0010}_{-0.0018}$	$0.7550^{+0.0015}_{-0.0010}$	$0.7952^{+0.0012}_{-0.0022}$
vnei.O [solar]	$2.350^{+0.017}_{-0.019}$	$2.659^{+0.015}_{-0.023}$	$2.74^{+0.017}_{-0.05}$	1.391 ± 0.012
vnei.Ne [solar]	$1.774^{+0.016}_{-0.013}$	$1.801^{+0.024}_{-0.012}$	$1.828^{+0.026}_{-0.018}$	$0.414^{+0.007}_{-0.005}$
vnei.Mg [solar]	$0.710^{+0.007}_{-0.014}$	$0.719^{+0.019}_{-0.007}$	$0.766^{+0.017}_{-0.016}$	$0.330^{+0.007}_{-0.006}$
vnei.Si [solar]	$0.529^{+0.010}_{-0.014}$	$0.579^{+0.017}_{-0.010}$	$0.600^{+0.021}_{-0.016}$	$0.340^{+0.008}_{-0.007}$
vnei.S [solar]	1.11 ± 0.06	$1.14^{+0.08}_{-0.05}$	$1.31^{+0.08}_{-0.11}$	0.78 ± 0.04
vnei.Fe [solar]	$0.3985^{+0.0016}_{-0.0011}$	$0.4270^{+0.0012}_{-0.0017}$	$0.4404^{+0.0025}_{-0.0017}$	$0.2588^{+0.0009}_{-0.0010}$
vnei.Ni [solar]	0.61 ± 0.04	$1.90^{+0.05}_{-0.030}$	$0.95^{+0.06}_{-0.05}$	$1.417^{+0.020}_{-0.023}$
vnei.Tau [s cm^{-3}]	$(5.73^{+0.05}_{-0.07}) \times 10^{11}$	$(7.11^{+0.08}_{-0.13}) \times 10^{11}$	$(5.31 \pm 0.07) \times 10^{11}$	$(3.056^{+0.028}_{-0.029}) \times 10^{11}$
vnei.Redshift	$(5.00^{+0.05}_{-0.10}) \times 10^{-3}$	$(-5.436^{+0.012}_{-0.025}) \times 10^{-3}$	$(-1.95^{+0.021}_{-0.08}) \times 10^{-3}$	$(4.515^{+0.00014}_{-0.006}) \times 10^{-3}$
vnei.norm	$(5.420 \pm 0.010) \times 10^{-2}$	$(5.058^{+0.010}_{-0.008}) \times 10^{-2}$	$(4.814^{+0.013}_{-0.012}) \times 10^{-2}$	$(7.667^{+0.013}_{-0.014}) \times 10^{-2}$
powerlaw.PhIndex	3.45 ± 0.04	$3.52^{+0.019}_{-0.05}$	3.23 ± 0.05	$2.934^{+0.014}_{-0.012}$
powerlaw.norm	$(2.19^{+0.05}_{-0.07}) \times 10^{-3}$	$(2.99 \pm 0.06) \times 10^{-3}$	$(2.84^{+0.12}_{-0.07}) \times 10^{-3}$	$(6.83^{+0.06}_{-0.07}) \times 10^{-3}$
red. χ^2 (DoF)	3.971 (703)	4.673 (706)	5.590 (344)	11.274 (723)
flux [$10^{-10} \text{ erg s}^{-1} \text{ cm}^{-2}$]	$1.2888^{+0.0021}_{-0.0018}$	1.2674 ± 0.0018	$1.2803^{+0.0024}_{-0.0027}$	1.3128 ± 0.0019

TM7. The small enhancement of flux for the two telescope modules without an on-chip filter might be caused by the light leakage which these telescope modules are experiencing. Nevertheless, the increase in flux is very small compared to other best-fit results.

As all of these parameters exhibit a similar value for all telescope modules one can consider those to describe real properties of the supernova remnant or in the case of the equivalent hydrogen column `tbvarabs.nH` as a real property of the ambient medium inside the LMC. The value of the ionization timescale of the ejecta component indicates that the plasma has not yet reached ionization equilibrium according to Sect. 3.4.1. Therefore, it justifies the use of a non-equilibrium ionization collisional plasma model. Additionally, the `powerlaw` photon index is in agreement with theoretical expectations of a young supernova remnant according to Sect. 3.4.3.

Moreover, some of the best-fit parameters show a consistency for the telescope modules with an on-chip filter but deviate for the two telescope modules without an on-chip filter. The first one of these parameters is the plasma temperature of the ambient LMC medium (`vnei.kT`) which is on the order 2.3 keV up to 3 keV for the telescope modules with on-chip filter, whereas for the telescope modules without an on-chip filter it is significantly smaller with a value of ≈ 0.3 keV. The ionization timescale (`vnei.Tau`) of this component shows the same behavior. For the five telescope modules which possess an on-chip filter it ranges between $\approx 4.5 \times 10^9$ s cm⁻³ and $\approx 5.5 \times 10^9$ s cm⁻³. In contrast, the one of the telescope modules without an on-chip filter is approximately 1.1×10^{11} s cm⁻³ which is more than one order of magnitude higher. The normalization of this component has a rather similar value for TM1–TM4 and TM6 and is around 6×10^{-3} . Contrary, the normalization of TM5 and TM7 has a value of $\approx 2 \times 10^{-2}$ which is higher. The metal abundances of this component were all frozen to 0.5 solar, i.e., no comparison for these parameters can be drawn.

Also a rather similar oxygen abundance (`vnei.O`) for TM1–TM4 and TM6 was determined for the component describing the ejecta. For these telescope modules oxygen is the most abundant element with an abundance of ≈ 2.5 solar. For TM5 and TM7 this value is significantly smaller and lies around 1.4 solar. Nevertheless, for all telescope modules the O abundance is significantly enhanced compared to the LMC metallicity of 0.5 solar. The neon abundance (`vnei.Ne`) is also significantly enhanced compared to the LMC metallicity for the telescope modules with an on-chip filter. For these telescope modules the value lies around 1.8 solar. For TM1, TM4, and TM6 this is the second highest abundance value. With a value of ≈ 0.4 solar the neon abundance of TM5 and TM7 is slightly below the LMC metallicity. A similar situation exists for the magnesium abundance (`vnei.Mg`). The telescope modules with an on-chip filter all show a slightly enhanced abundance value around 0.7 solar, whereas the value of TM5 and TM7 is 0.33 solar and therefore slightly below the LMC metallicity. A similar behavior can be observed for the silicon abundance (`vnei.Si`). Here also the value of the telescope modules which possess an on-chip filter is only slightly enhanced compared to the LMC metallicity, whereas the value of the two telescope modules which do not have an on-chip filter is slightly below the LMC metallicity. The sulfur abundance (`vnei.S`) of the ejecta component is again enhanced for all telescope modules. For TM1, TM4, TM2, TM3, and TM6 the sulfur abundance is on a solar level. In contrast, the value of TM5 and TM7 is ≈ 0.8 and sub-solar but higher than the LMC metallicity. Contrary, the iron abundance (`vnei.Fe`) is below the LMC metallicity of 0.5 solar for all telescope modules. With an abundance value of ≈ 0.4 the telescope

modules with an on-chip filter show only a slightly reduced Fe abundance, whereas the value of TM5 and TM7 is ≈ 0.26 which is even smaller.

The consistency of these best-fit parameters between the telescope modules with an on-chip filter and the discrepancy to those without an on-chip filter suggests that either the effect of the light leakage has a major influence on these fit parameters or there are calibration issues for TM5 and TM7. As the effect of the light leakage above 0.5 keV is not as pronounced as in the soft energy band below 0.5 keV it is not expected that the light leak will influence all of the above metal abundance so drastically. This points towards issues with the calibration of TM5 and TM7.

However, the fact that the oxygen abundance is so strongly enhanced compared to the LMC metallicity for all telescope modules indicates that this is a real property of SNR N132D. The same applies to the sulfur abundance which is also enhanced for all telescope modules compared to the LMC metallicity which also suggests that this is a real physical property of the supernova remnant.

Inconsistent best-fit parameters

Only a few fit parameters show an inconsistency for all telescope modules. The first one to note here is the redshift of this first `vnei` component which describes the ambient LMC medium. It even varies between the five telescope modules with an on-chip filter. Only for TM1 and TM4 a positive redshift was determined, whereas for all other telescopes a negative one was derived. However, neglecting the sign the redshift is on the same order of magnitude for all telescope modules with on-chip filter. The redshift derived for the two telescope modules without an on-chip filter is slightly stronger.

Additionally, the nickel abundance (`vnei.Ni`) of the second `vnei` component which describes the ejecta varies quite strongly from one telescope module to another. The smallest value was determined for TM1 and TM4, where the nickel abundance lies around 0.6 solar. This is followed by the abundance of TM6 with a value of 0.95 solar. The value of TM5 and TM7 is 1.4 solar which is even higher but not as high as the value of TM2 and TM3, which show a Ni abundance of 1.9 solar. Finally, the redshift of the second `vnei` component (`vnei.Redshift`) also varies from one telescope module to another. This time, TM1 and TM4 as well as TM5 and TM7 exhibit a positive redshift, whereas TM2 and TM3 as well as TM6 show a negative one. This means the redshift of both `vnei` components is positive for TM1 and TM4. In contrast, for TM2 and TM3 as well as for TM6 the redshift of both components is negative. Only TM5 and TM7 show a component with a negative redshift and one with a positive redshift. However, the absolute value of the ejecta redshift is on the same order of magnitude for all telescope modules.

The fact that these fit parameters are inconsistent for all telescope modules again points towards still existing calibration issues with all telescope modules of the *eROSITA* instrument and not only for TM5 and TM7. In particular the different redshift values of both `vnei` components which also show a change in their signs from one telescope module to another indicate that spectral lines are shifted in opposite directions for different telescope modules which means that the calibration of the instrument still needs improvement. Additionally, the goodness of the fits represented by the reduced χ^2 values is not acceptable and might be improved by a better calibration of the individual telescope modules. Especially for the two telescope modules which are facing light leakage no good fit could be achieved.

Conclusion of the spectral analysis

Although the best-fit parameter values show a `powerlaw` photon index which is in agreement with theoretical expectations (see Sect. 3.4.1) and suggest an oxygen-rich remnant with plasma which has still not yet reached ionization equilibrium, one cannot trust these results. On the one hand-side the quality of the fits is not good and also the differences in the spectra of the individual telescope modules indicate that there are still issues with the calibration of the instrument. In particular one would expect to derive similar values for the best-fit parameters for all telescope modules. In addition, the redshift values of both `vnei` components point to an incorrect calibration of the instrument. Furthermore, the effect of light leakage has a severe impact on the spectra of TM5 and TM7. However, the impact of this effect differs from TM5 to TM7 as can be seen in the lower panel of Fig. 8.11. Here, one can clearly see that the residuals of TM5 in black and TM7 in red deviate from each other indicating that the influence of the light leak on the spectral shape varies between both telescope modules and that fitting these telescope modules individually would be recommended. In conclusion, the best-fit results cannot be thought to represent the physical properties of the supernova remnant since the calibration of the instrument needs improvement and is still ongoing.

8.5 Estimating the age of the LMC SNR N132D

Following the approach presented in Sect. 5.7 for the case of the Galactic SNR 1006 an age will be estimated for SNR LMC N132D in the following. In order to derive the physical radius of this remnant its distance and the viewing angle are needed. The distance to the LMC is well studied (de Grijs et al., 2014) and was determined to a value of $d = (49.97 \pm 1.30)$ kpc (Pietrzyński et al., 2013). The viewing angle $\delta/2$ of N132D is approximately $72.9''$. According to equation 5.8 this corresponds to a physical radius of the supernova remnant of $R = (17.7 \pm 0.5)$ pc. For the determination of the viewing angle the source region as displayed in Fig. 8.3 was utilized. Since the shape of the remnant is not circular this value will overestimate the real physical extent of SNR N132D.

In addition to the physical radius of the remnant its temperature is needed to estimate its age. The temperature can be calculated from the mean plasma temperature `vnei.kT` of the ejecta component. The mean value of the best-fit results for all telescope modules (see Tab. 8.6) is $kT = (0.7599_{-0.0008}^{+0.0006})$ keV. This translates into a temperature $T = (8.817_{-0.009}^{+0.007}) \times 10^6$ K.

Inserting the values for the physical radius R and the temperature T into equation 5.12 yields an age of $t = (8.11 \pm 0.22)$ kyr. This value is higher than the age of ≈ 2500 years which was determined by Vogt & Dopita (2011). Compared to the case of SNR 1006, the difference between the estimated age and the expectations is smaller for SNR N132D although it is still a factor of ≈ 3.3 too high. As already discussed in Sect. 5.7 one possible explanation for the higher estimated age might be the age of SNR LMC N132D. This remnant is also still quite young which means the Sedov-Taylor model will overestimate its age. Additionally, due to its irregular shape a further source of uncertainty is added by the determination of the viewing angle. In order to derive a value for the viewing angle the source region as depicted in Fig. 8.3 was utilized. This region possibly overestimates the viewing angle which results in a higher estimate for the age of SNR N132D. Nevertheless,

the value derived with the Sedov-Taylor model is still on the same order of magnitude as the value stated by Vogt & Dopita (2011). Therefore, the derived value for the age is considered a good rough estimate.

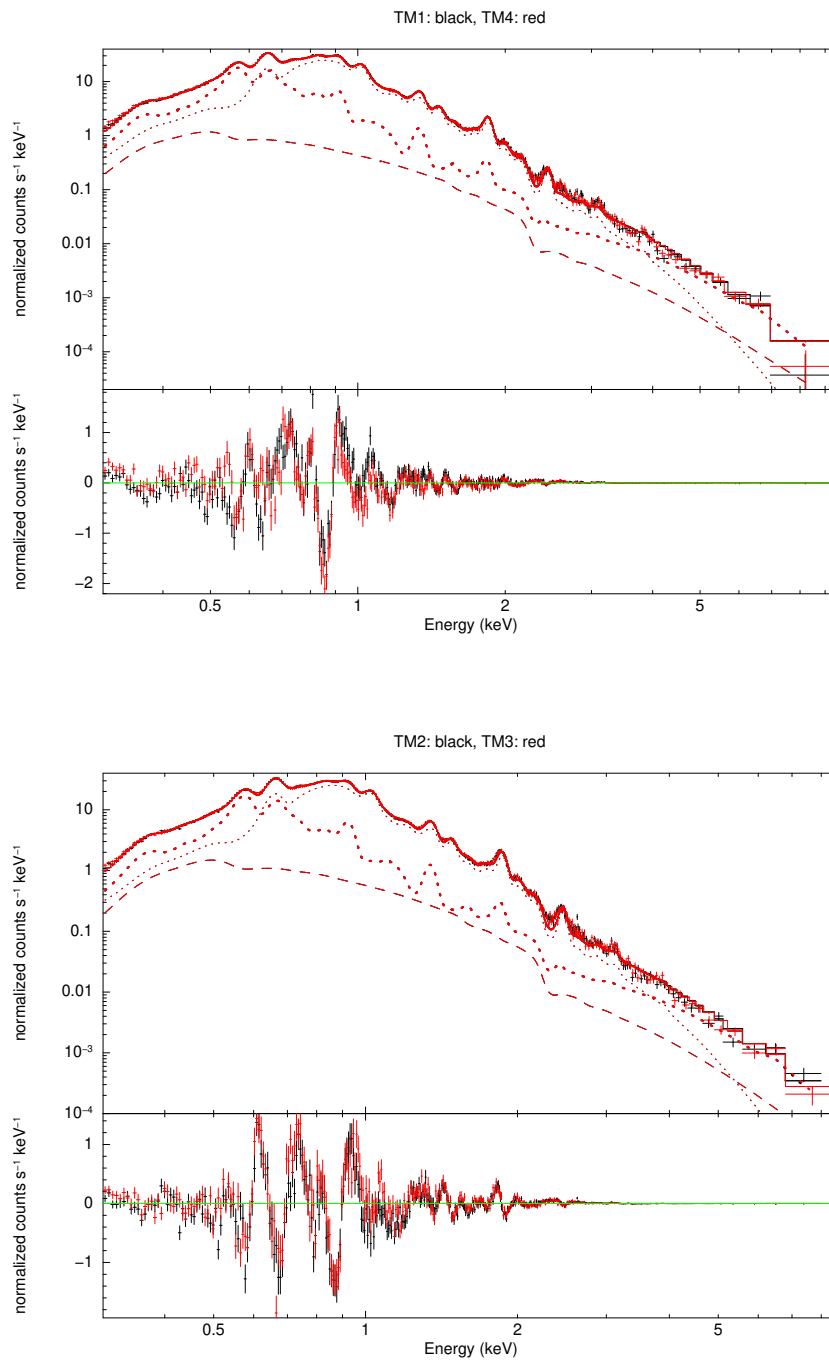


Figure 8.10: Background subtracted source spectra and best-fit model. The upper panel shows the data of TM1 in black and the one of TM4 in red. The lower panel shows the data of TM2 in black and the one of TM3 in red. The dotted lines in both panels symbolize the $vnei$ components. The thin one represents the ejecta component and the thicker one the ambient LMC medium component. The dashed line denotes the `powerlaw` component.

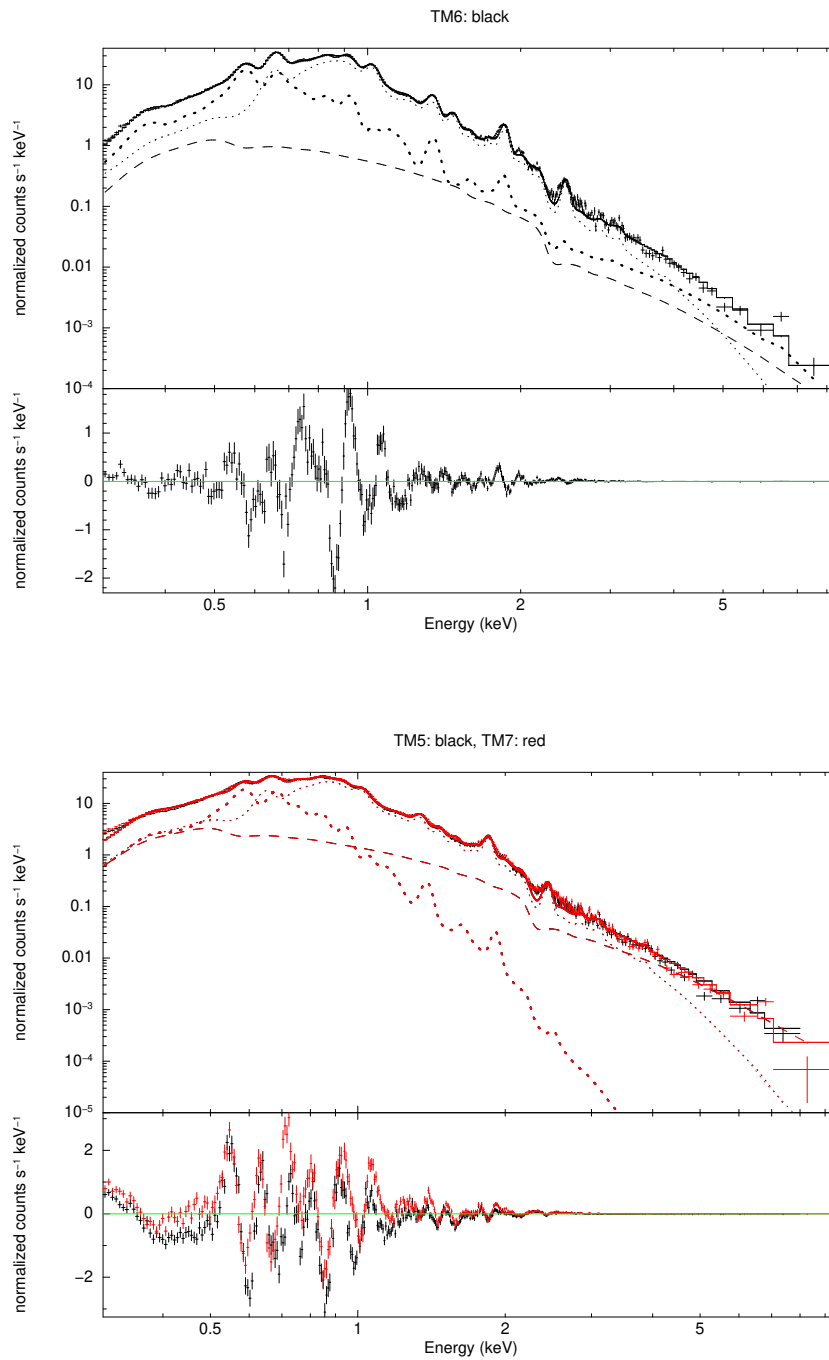


Figure 8.11: Background subtracted source spectra and best-fit model. The upper panel shows the data of TM6. The lower panel shows the data of TM5 in black and the one of TM7 in red. The dotted lines symbolize the $vnei$ components. The thin one represents the ejecta component and the thicker one the ambient LMC medium component. The dashed line denotes the `powerlaw` component.

9 Conclusion and outlook

9.1 The Galactic SNR 1006

9.1.1 Analysis of *XMM-Newton* data

The aim of the first part of this thesis was to predict the capabilities of the *eROSITA* all-sky survey regarding supernova remnants. In order to derive the basic properties of such a source, *XMM-Newton* data of the Galactic SNR 1006 was analyzed. Since the structure of the remnant varies over its surface and the remnant is in particular showing thermal emission at its center and non-thermal emission at its north-eastern and the south-western limbs four regions were defined for the analysis. The source spectra were modeled with a `vnei` component to account for the thermal emission and a `powerlaw` component describing the non-thermal emission. In addition, a solar wind charge exchange line was added to the fit model. Two of the regions dominated by the thermal emission did not show a necessity to include the `powerlaw` component into the fit model. The spectra of all four regions could be fitted reasonably well. In the three regions dominated by the thermal emission the most abundant element was determined to be sulfur followed by silicon. Also oxygen, magnesium, and iron were enhanced compared to the solar value. For the fit model of the fourth region all metal abundances of the `vnei` component were frozen to the solar value. With an ionization timescale $< 3 \times 10^{11} \text{ cm}^{-3}$ the remnant's plasma has still not yet reached ionization equilibrium, i.e., the use of a non-equilibrium ionization plasma model is justified. The `powerlaw` photon index yielded a value of $2.720^{+0.009}_{-0.007}$ in the region dominated by the non-thermal emission. This value is compatible with theoretical expectations. The absorbed flux values in the energy range 0.3–10.0 keV are on the order of $\approx 2 \times 10^{-13} \text{ erg s}^{-1} \text{ cm}^{-2}$ for the regions dominated by the thermal emission and $\approx 11 \times 10^{-13} \text{ erg s}^{-1} \text{ cm}^{-2}$ for the region dominated by the non-thermal emission.

Finally, the age of SNR 1006 was estimated using the Sedov-Taylor model. The calculations yielded a value of $(5.9 \pm 0.4) \text{ kyr}$ which is higher than the real age of SNR 1006. To some extent this can be explained by the fact that the Sedov-Taylor model is expected to overestimate the age of young supernova remnants. In addition, the derived values for the viewing angle and the plasma temperature also add further uncertainties to the estimate. Therefore, the determined value for the age is considered a good rough estimate of the real age of SNR 1006.

9.1.2 Results of the simulation for the *eROSITA* all-sky survey

The results of the *XMM-Newton* data analysis of SNR 1006 were used to create a SIMPUT file which provides the basic information on the characteristic properties of the remnant to the simulation software. The simulation results showed that after one complete scan of the sky by *eROSITA* (i.e., six months of all-sky survey) too few photons from the source were registered to allow a reasonable analysis of the data. Therefore, the simulations

were extended to cover the full planned four years of the all-sky survey phase. After this time range the extraction of reasonable spectra was possible. However, the background contribution dominated for energies above ≈ 2 keV. For the simulated data two regions were defined. One of them covered the center of the remnant which is expected to be dominated by the thermal emission and the other one was located at the south-western rim which is assumed to be dominated by the non-thermal emission. For the extraction of the spectra the SIXTE tool `makespec` was used. Since the supernova remnant was simulated as a superposition of the thermal and the non-thermal component a combination of the fit models of all four regions analyzed in the *XMM-Newton* data analysis was applied. All parameters were frozen to the values of the *XMM* data analysis, only the normalizations of the fit model components were allowed to vary. For both regions in the energy range 0.3–10.0 keV no good fits could be achieved. This could be improved by restricting the considered energy range to the band 0.3–2.0 keV as the background contribution dominated for energies above ≈ 2 keV. The region covering the center of the remnant was found to be best described by a single `vnei` component and a `powerlaw` component. The derived absorbed flux value is on the order of $\approx 2 \times 10^{-12}$ erg s $^{-1}$ cm $^{-2}$ for an energy range 0.3–10.0 keV and slightly below this value for the soft energy band 0.3–2.0 keV. This flux value is approximately one order of magnitude higher than the one derived in the *XMM-Newton* data analysis for the regions dominated by thermal emission. To a certain extent this can be explained by a greater source area for the simulated data. However, also the fact of a less sensitive effective area for higher energies or the background modeled by the simulation software might add some uncertainty to the derived absorbed flux value.

In the beginning the second region was expected to represent a region of the remnant dominated by the non-thermal emission. However, it turned out that this region is as well dominated by thermal emission and can be described by a single `vnei` component. The flux value derived for this region is $\approx 1.5 \times 10^{-13}$ erg s $^{-1}$ cm $^{-2}$ for the energy ranges 0.3–10.0 keV and 0.3–2.0 keV. This value is smaller than the one derived in the *XMM-Newton* data analysis for the region dominated by the non-thermal emission although the area of the region of the simulation is higher. On the one hand-side this can be explained by the fact that *eROSITA* is less sensitive to harder photons than *XMM-Newton* leading to a reduced flux. In addition, the possible explanations discussed for the case of the first region apply here as well. Furthermore, the surface brightness changes over the remnant, which makes the comparison of different regions even more complicated.

A comparison of the spectrum extraction tools provided by SIXTE and eSASS revealed that spectra extracted with both tools are not identical. One reason might be the use of a different ARF file. The effective area calculated by `srctool` takes effects like vignetting and the PSF into account, which are very important for survey observations where the position of the source on the detector changes with time. Additionally, `srctool` calculates a corrected effective exposure time which is smaller than the one derived by `makespec`. This might also lead to some difference in the resulting spectra. However, the derived absorbed flux values for both extraction tools are on the same order of magnitude and both appear reasonable.

9.2 The LMC SNR N132D

9.2.1 Light leak in TM5 and TM7

In the second part of this thesis data of the LMC SNR N132D taken during *eROSITA*'s CalPV phase were analyzed. Already from the background subtracted spectra of all seven telescope modules it was visible that the behavior of TM5 and TM7 deviates from the one of the other telescope modules. The reason is that these two telescope modules experience light leakage. This effect was first analyzed by comparing the amount of background counts in the energy range 0.2–10.0 keV and in a soft energy band ranging from 0.2 keV up to 0.5 keV. The amount of background counts of TM1–TM4 was on a similar low level, whereas the amounts of TM5, TM6, and TM7 showed an enhancement. To quantify this enhancement the amount of background counts of the latter three telescope modules was compared to the mean value of the amount of background counts of TM1–TM4. The conclusion of this comparison was that the background of TM5 and TM7 is enhanced by $< 10\%$ compared to this mean value in the energy range 0.2–10.0 keV for both considered data processing versions. In contrast, for TM6 the enhancement is smaller with a value of $\approx 5\%$ in the same energy range. For all three telescope modules the increase in the background counts is stronger in the soft energy band 0.2–0.5 keV. Here, the background of TM5 is enhanced by a factor of $\approx 40\%$ compared to the mean value of TM1, TM2, TM3, and TM4. For TM6 the increase is $\approx 20\%$ which is again smaller, whereas TM7 shows the highest increase with a background more than 50% higher than the mean of TM1–TM4. To summarize, TM5 and TM7 exhibit a strong enhancement in the amount of background counts compared to the mean value of TM1–TM4 in the soft energy band, whereas the increase in the energy range 0.2–10.0 keV is not as pronounced as in the soft energy band. Due to this fact, TM5 and TM7 are considered to be strongly affected by light leakage. Although TM6 also shows an enhancement in the amount of background counts this increase is not as strong as for TM5 and TM7 and therefore this telescope module is not considered to be affected by light leakage.

To estimate the influence of the light leak in TM5 and TM7 on flux values derived in the soft energy band from 0.2 keV up to 0.5 keV the background subtracted count rates were determined for all seven telescope modules. The count rates of TM1–TM4 and TM6 were quite similar, whereas the ones of TM5 and TM7 deviated from the others. Therefore, a mean count rate was calculated for TM1, TM2, TM3, TM4, and TM6. Taking the ratio of the count rates of TM5 and TM7, respectively, with this mean count rate yielded an enhancement in the count rate of TM5 between 45% (processing version 941) and 55% (processing version 945). For TM7 these ratios are even higher. Here, the increase in the count rate ranges between 53% (processing version 941) and 65% (processing version 945). Therefore, flux values derived in the soft energy band 0.2–0.5 keV will be strongly enhanced for TM5 and TM7 meaning that one has to be careful when analyzing spectra measured with TM5 and TM7 of the *eROSITA* mission.

One possible reason why TM5 and TM7 are affected by light leakage but not the other telescope modules is that TM5 and TM7 do not possess an on-chip filter for blocking optical light, whereas TM1, TM2, TM3, TM4, and TM6 do. This is also reflected in the effective area of the individual telescope modules which is higher for TM5 and TM7 below ≈ 0.6 keV.

9.2.2 Spectral analysis of the individual telescope modules

In contrast to the simulated spectra of SNR 1006 the spectra of SNR N132D were not dominated by the background above ≈ 2 keV due to the higher exposure time and the higher signal to noise ratio. Therefore, the spectra of the LMC SNR N132D could be investigated in the energy range 0.3–10.0 keV. The spectra of the seven telescope modules were either fitted simultaneously or in pairs accounting for their different spectral behavior. The fit model contained one `vnei` component for the ambient LMC medium, another one for the ejecta, and a `powerlaw` component to account for non-thermal emission from the remnant. Unfortunately, it was not possible to achieve a good fit for any of the considered combinations of the telescope modules. Nevertheless, some of the fit parameters were consistent for all best-fits. These include the equivalent hydrogen column of the absorption (`tbvarabs.nH`) which ranges between $\approx 6 \times 10^{22} \text{ cm}^{-2}$ and $\approx 8 \times 10^{22} \text{ cm}^{-2}$, the plasma temperature (`vnei.kT`) of the ejecta component which has a value of ≈ 0.75 keV, the ionization timescale (`vnei.Tau`) of the same component which is on the order of $\approx 5.5 \times 10^{11} \text{ s cm}^{-3}$, and the normalization (`vnei.norm`) of the ejecta component which is approximately 5×10^{-2} . Also consistent for all telescope modules are the `powerlaw` photon index (`powerlaw.PhoInd`) which ranges from ≈ 3 to ≈ 3.5 and the normalization of this component (`powerlaw.norm`) which lies between $\approx 2 \times 10^{-3}$ and $\approx 7 \times 10^{-3}$. Furthermore, the absorbed flux values derived in the energy band 0.3–10.0 keV were all rather similar to each other with a value of $\approx 1.28 \times 10^{10} \text{ erg s}^{-1} \text{ cm}^{-2}$. This indicates that the effect of the light leakage on the flux in the energy band 0.3–10.0 keV is not as pronounced as it was estimated for the soft energy band 0.2–0.5 keV.

Apart from these best-fit parameters which were consistent for all telescope modules there were some which showed a consistency for the telescope modules which possess an on-chip filter (TM1, TM2, TM3, TM4, and TM6) but a discrepancy for the two telescope modules which do not have an on-chip filter (TM5 and TM7). One of these is the plasma temperature (`vnei.kT`) of the component describing the ambient LMC medium which was on the order 2.3 keV up to 3 keV for the telescope modules with on-chip filter, whereas for the telescope modules without an on-chip filter it had a value of ≈ 0.3 keV which is significantly smaller. Also the ionization timescale (`vnei.Tau`) showed a similar behavior. For the telescope modules with an on-chip filter it was $< 5.5 \times 10^9 \text{ s cm}^{-3}$, whereas for the telescope modules 5 and 7 it was more than one order of magnitude higher. The same applies to the normalization of this component (`vnei.norm`) which was around 6×10^{-3} for TM1, TM2, TM3, TM4, and TM6. Contrary, the normalization of TM5 and TM7 was higher and had a value of $\approx 2 \times 10^{-2}$. Additionally, most of the varied metal abundances showed a similar behavior. The abundances of oxygen, neon, magnesium, silicon, sulfur, and iron had similar values for the telescope modules with an on-chip filter but deviated for the two telescope modules without an on-chip filter. Nevertheless, the O and S abundances were enhanced for all telescope modules compared to the LMC metallicity. In addition, all telescope modules showed a Fe abundance below the LMC metallicity. In contrast, the abundances of Ne, Mg, and Si were enhanced compared to the LMC metallicity for TM1, TM2, TM3, TM4, and TM6 but below the LMC metallicity for TM5 and TM7.

However, not all best-fit parameters exhibited a consistency for the telescope modules with an on-chip filter. For instance, the values of the redshift (`vnei.Redshift`) of both components varied even between TM1, TM2, TM3, TM4, and TM6. The value of the component describing the ambient LMC medium had a positive sign for TM1 and TM4

but a negative one for the other telescope modules. For the component representing the ejecta the redshift was positive for TM1 and TM4 as well as for TM5 and TM7 but negative for TM2 and TM3 as well as TM6. Furthermore, also the nickel abundance ($v_{\text{nei.Ni}}$) of the ejecta component deviated among all telescope modules. For TM1 and TM4 the value was only slightly enhanced compared to the LMC metallicity and the lowest for all telescope modules. For TM6 the nickel abundance had almost a solar value. TM5 and TM7 showed an even higher value but for TM2 and TM3 the highest value was determined with almost two times the solar value.

One can consider all best-fit parameters that are consistent for all telescope modules to describe a real property of the supernova remnant. In contrast, the parameters that are consistent only for the telescope modules with an on-chip filter but differ for the ones without an on-chip filter indicate issues with the calibration of TM5 and TM7 or an influence of the light leakage affecting these telescope modules. Nevertheless, for some of these best-fit parameters at least the tendency for an abundance value above or below the LMC metallicity is consistent and also points to the real properties of the remnant. However, the redshift values and the nickel abundance values suggest that there additionally are calibration issues for all telescope modules and not only these which are facing the light leak. Therefore, further improvement of the calibration of all telescope modules of the *eROSITA* instrument and further investigation of the effect of the light leakage in TM5 and TM7 is necessary.

9.2.3 Estimating the age of the LMC SNR N132D

Finally, the age of the supernova remnant N132D was estimated using the viewing angle and the mean of the plasma temperatures determined by the spectral fits to the telescope modules. The estimate yielded an age of $t = (8.11 \pm 0.22)$ kyr which is higher than the age of ≈ 2500 years which was determined by Vogt & Dopita (2011). Nevertheless, since the Sedov-Taylor model is expected to overestimate the age of young SNRs and the irregular shape of SNR N132D adds a further source of uncertainty to the estimation, the derived value is considered a good rough estimate.

9.3 Outlook

The simulations performed for the supernova remnant 1006 revealed that after the first complete scan of the sky by *eROSITA* it is possible to detect its extended emission by looking at an image of this area of the sky. However, it is not possible to extract reasonable spectra after the first six months of all-sky survey observations. In contrast, after the planned end of the all-sky survey phase, which takes four years, it is possible to extract spectra from the source region of a supernova remnant. Nevertheless, the simulations showed that the spectra of a supernova remnant will most likely be dominated by the background above ≈ 2 keV since the fully corrected exposure time is still quite low. In particular, this will influence the measured contribution of a non-thermal emission component from the supernova remnant. In addition, due to the contamination by the background above ≈ 2 keV a restriction of the considered energy range of a spectral fit to a soft energy band is recommended in order to improve the fit.

The analysis of *eROSITA* data of the LMC SNR N132D revealed that the light leak of TM5 and TM7 influences their spectral shape and in this way determined best-fit parameters. Therefore, it is necessary to investigate the effect of the light leakage further. In addition, also the calibration of all seven telescope modules of the *eROSITA* instrument needs further improvement. For none of the telescope modules an acceptable fit could be achieved. Although for some of the best-fit parameters a consistency could be observed between the values of the telescope modules with an on-chip filter there were also best-fit parameters which did not exhibit a consistency for any of the telescope modules. As soon as these calibration issues are solved the full capabilities of the *eROSITA* mission regarding supernova remnants as extended sources can be deployed.

References

- Acero F., Aharonian F., Akhperjanian A.G., et al., 2010, *Astronomy & Astrophysics* 516, A62
- Acero F., Ballet J., Decourchelle A., 2007, *Astronomy & Astrophysics* 475, 883
- Ackermann M., Albert A., Atwood W.B., et al., 2016, *Astronomy & Astrophysics* 586, A71
- Aharonian F., Akhperjanian A., Barrio J., et al., 2001, *Astronomy & Astrophysics* 370, 112
- Aharonian F.A., Akhperjanian A.G., Aye K.M., et al., 2004, *Nature* 432, 75
- Ahmad I., Greene J.P., Moore E.F., et al., 2006, *Physical Review C* 74, 065803
- Arefiev V., Pavlinsky M., Lapshov I., et al., 2008, In: *Space Telescopes and Instrumentation 2008: Ultraviolet to Gamma Ray*, Vol. 7011. Society of Photo-Optical Instrumentation Engineers (SPIE) Conference Series, p. 70110L
- Arnaud K.A., 1996, In: *Astronomical Data Analysis Software and Systems V*, Vol. 101. Astronomical Society of the Pacific Conference Series, Jacoby, George H. and Barnes, Jeannette, p. 17
- Arnaud K.A., George I.M., Tennant A., 2009, *The OGIP Spectral File Format*, OGIP/92-007, HEASARC, https://heasarc.gsfc.nasa.gov/docs/heasarc/ofwg/docs/spectra/ogip_92_007/ogip_92_007.html
- Arnett D., 1996, *Supernovae and Nucleosynthesis: An Investigation of the History of Matter from the Big Bang to the Present*
- Asvarov A.I., Guseinov O.H., Kasumov F.K., Dogel' V.A., 1990, *Astronomy & Astrophysics* 229, 196
- Axford W.I., Leer E., Skadron G., 1977, In: *International Cosmic Ray Conference*, Vol. 11. International Cosmic Ray Conference, p. 132
- Bamba A., Ohira Y., Yamazaki R., et al., 2018, *The Astrophysical Journal* 854, 71
- Becker R.H., Szymkowiak A.E., Boldt E.A., et al., 1980, *Astrophysical Journal* 240, L33
- Bell A.R., 1978, *Monthly Notices of the Royal Astronomical Society* 182, 147
- Berezhko E.G., Ellison D.C., 1999, *The Astrophysical Journal* 526, 385
- Berezhko E.G., Völk H.J., 2007, *The Astrophysical Journal* 661, L175
- Blair W.P., Morse J.A., Raymond J.C., et al., 2000, *The Astrophysical Journal* 537, 667
- Blandford R., Eichler D., 1987, *Physics Reports* 154, 1
- Blandford R.D., Ostriker J.P., 1978, *Astrophysical Journal* 221, L29
- Blasi P., 2002, *Astroparticle Physics* 16, 429
- Bleeker J.A.M., Willingale R., van der Heyden K., et al., 2001, *Astronomy & Astrophysics* 365, L225
- Blondin J.M., Ellison D.C., 2001, *The Astrophysical Journal* 560, 244
- Bookbinder J., 2010, arXiv e-prints arXiv:1001.2329
- Borkowski K.J., Hendrick S.P., Reynolds S.P., 2007, *The Astrophysical Journal* 671, L45
- Borkowski K.J., Lyerly W.J., Reynolds S.P., 2001, *The Astrophysical Journal* 548, 820
- Borkowski K.J., Szymkowiak A.E., 1997, *The Astrophysical Journal* 477, L49
- Bradt H., 2004, *Astronomy Methods: A Physical Approach to Astronomical Observations*, Cambridge University Press
- Brunner H., Boller T., Coutinho D., et al., 2018, In: *Proceedings of the SPIE*, Vol. 10699. Society of Photo-Optical Instrumentation Engineers (SPIE) Conference Series, p. 106995G
- Burwitz V., Predehl P., Friedrich P., et al., 2014, In: *Proceedings of the SPIE*, Vol. 9144. Society of Photo-Optical Instrumentation Engineers (SPIE) Conference Series, p. 91441X
- Carter J.A., Read A.M., 2007, *Astronomy & Astrophysics* 464, 1155
- Chevalier R.A., 1982, *The Astrophysical Journal* 258, 790
- Clayton D.D., Silk J., 1969, *Astrophysical Journal*, 158, L43
- Danziger I.J., Dennefeld M., 1976, *Astrophysical Journal* 207, 394

- Dauser T., Falkner S., Lorenz M., et al., 2019, *Astronomy & Astrophysics* 630, A66
- de Grijs R., Wicker J.E., Bono G., 2014, *The Astronomical Journal* 147, 122
- Decourchelle A., Ellison D.C., Ballet J., 2000, *The Astrophysical Journal* 543, L57
- den Herder J.W., Brinkman A.C., Kahn S.M., et al., 2001, *Astronomy & Astrophysics* 365, L7
- Dickel J.R., Milne D.K., 1995, *Astronomical Journal* 109, 200
- Diehl R., Timmes F.X., 1998, *The Publications of the Astronomical Society of the Pacific* 110, 637
- ESA: XMM-Newton SOC 2019, XMM-Newton Users Handbook, Issue 2.17
- Filippenko A.V., 1997, *Annual Review of Astronomy & Astrophysics* 35, 309
- Friedrich P., Bräuninger H., Budau B., et al., 2008, In: *Space Telescopes and Instrumentation 2008: Ultraviolet to Gamma Ray*, Vol. 7011. Society of Photo-Optical Instrumentation Engineers (SPIE) Conference Series, p. 70112T
- Friedrich P., Rohé C., Gaida R., et al., 2014, In: *Proceedings of the SPIE*, Vol. 9144. Society of Photo-Optical Instrumentation Engineers (SPIE) Conference Series, p. 91444R
- Gabriel A.H., Jordan C., 1969, *Monthly Notices of the Royal Astronomical Society* 145, 241
- Gaensler B.M., Slane P.O., 2006, *Annual Review of Astronomy & Astrophysics* 44, 17
- Gardner F.F., Milne D.K., 1965, *Astronomical Journal* 70, 754
- Ginzburg V.L., Syrovatskii S.I., 1965, *Annual Review of Astronomy & Astrophysics* 3, 297
- Ginzburg V.L., Syrovatskij S.I., 1967, In: van Woerden H. (ed.) *Radio Astronomy and the Galactic System*, Vol. 31. IAU Symposium, p. 411
- Green D.A., 2019, *Journal of Astrophysics and Astronomy* 40, 36
- H. E. S. S. Collaboration Abramowski A., Aharonian F., et al., 2015, *Science* 347, 406
- Hanisch R.J., Farris A., Greisen E.W., et al., 2001, *Astronomy & Astrophysics* 376, 359
- Helder E.A., Vink J., Bykov A.M., et al., 2012, *Space Science Reviews* 173, 369
- Hell N., 2017, Ph.D. thesis, Friedrich-Alexander-Universität Erlangen-Nürnberg
- Hinton J.A., Hofmann W., 2009, *Annual Review of Astronomy & Astrophysics* 47, 523
- Irrgang A., 2018, *Principles of Stellar Evolution and Nucleosynthesis*, Lecture held at FAU
- Itoh H., 1977, *Publications of the Astronomical Society of Japan* 29, 813
- Jansen F., Lumb D., Altieri B., et al., 2001, *Astronomy & Astrophysics* 365, L1
- Kaastra J.S., Paerels F.B.S., Durret F., et al., 2008, *Space Science Reviews* 134, 155
- Kaspi V.M., 1998, *Advances in Space Research* 21, 167
- Koyama K., Petre R., Gotthelf E.V., et al., 1995, *Nature* 378, 255
- Krauss F., 2016, Ph.D. thesis, Friedrich-Alexander-Universität Erlangen-Nürnberg
- Kreikenbohm A., 2013, *Master's thesis*, Universität Würzburg
- Laming J.M., 2001, *The Astrophysical Journal* 563, 828
- Lasker B.M., 1978, *Astrophysical Journal* 223, 109
- Liedahl D.A., 1999, *The X-Ray Spectral Properties of Photoionized Plasma and Transient Plasmas*, Vol. 520, p. 189
- Long K.S., Reynolds S.P., Raymond J.C., et al., 2003, *The Astrophysical Journal* 586, 1162
- Maggi P., Haberl F., Kavanagh P.J., et al., 2016, *Astronomy & Astrophysics* 585, A162
- Mason K.O., Breeveld A., Much R., et al., 2001, *Astronomy & Astrophysics* 365, L36
- McKee C.F., Ostriker J.P., 1977, *Astrophysical Journal* 218, 148
- Meidinger N., Andritschke R., Bornemann W., et al., 2014, In: *Proceedings of the SPIE*, Vol. 9144. Society of Photo-Optical Instrumentation Engineers (SPIE) Conference Series, p. 91441W
- Meidinger N., Andritschke R., Elbs J., et al., 2011, In: *Proceedings of the SPIE*, Vol. 8145. Society of Photo-Optical Instrumentation Engineers (SPIE) Conference Series, p. 814502
- Meidinger N., Andritschke R., Elbs J., et al., 2008, In: *Space Telescopes and Instrumentation 2008: Ultraviolet to Gamma Ray*, Vol. 7011. Society of Photo-Optical Instrumentation Engineers (SPIE) Conference Series, p. 70110J
- Merloni A., Predehl P., Becker W., et al., 2012, arXiv e-prints arXiv:1209.3114
- Mewe R., 1999, *Atomic Physics of Hot Plasmas*, Vol. 520, p. 109
- Mewe R., Schrijver J., 1978, *Astronomy & Astrophysics* 65, 115

- Miceli M., Bocchino F., Decourchelle A., et al., 2012, *Astronomy & Astrophysics* 546, A66
- Miceli M., Bocchino F., Iakubovskiy D., et al., 2009, *Astronomy & Astrophysics* 501, 239
- Minkowski R., 1941, *Publications of the Astronomical Society of the Pacific* 53, 224
- Nagataki S., Hashimoto M.a., Sato K., et al., 1998, *The Astrophysical Journal* 492, L45
- Oort J.H., 1951, In: *Problems of Cosmical Aerodynamics.*, p. 118
- Pavlinisky M., Akimov V., Levin V., et al., 2016, In: *Proceedings of the SPIE*, Vol. 9905. Society of Photo-Optical Instrumentation Engineers (SPIE) Conference Series, p. 99051J
- Pavlinisky M., Akimov V., Levin V., et al., 2011, In: *Proceedings of the SPIE*, Vol. 8147. Society of Photo-Optical Instrumentation Engineers (SPIE) Conference Series, p. 814706
- Pavlinisky M., Arefiev V., Churazov E., et al., 2007, In: *Optics for EUV, X-Ray, and Gamma-Ray Astronomy III*, Vol. 6688. Society of Photo-Optical Instrumentation Engineers (SPIE) Conference Series, p. 66880L
- Pavlinisky M., Levin V., Akimov V., et al., 2018, In: *Proceedings of the SPIE*, Vol. 10699. Society of Photo-Optical Instrumentation Engineers (SPIE) Conference Series, p. 106991Y
- Pence W.D., Chiappetti L., Page C.G., et al., 2010, *Astronomy & Astrophysics* 524, A42
- Phillips M.M., Wells L.A., Suntzeff N.B., et al., 1992, *Astronomical Journal* 103, 1632
- Pietrzyński G., Graczyk D., Gieren W., et al., 2013, *Nature* 495, 76
- Ponz J.D., Thompson R.W., Munoz J.R., 1994, *Astronomy & Astrophysics Supplement* 105, 53
- Porquet D., Dubau J., Grosso N., 2010, *Space Science Reviews* 157, 103
- Prantzos N., 2011, arXiv e-prints arXiv:1101.2112
- Predehl P., 1999, In: Siegmund O.H., Flanagan K.A. (eds.) *EUV, X-Ray, and Gamma-Ray Instrumentation for Astronomy X*, Vol. 3765. Society of Photo-Optical Instrumentation Engineers (SPIE) Conference Series, p.172
- Predehl P., 2017, *Astronomische Nachrichten* 338, 159
- Predehl P., Andritschke R., Babushkin V., et al., 2016, In: *Proceedings of the SPIE*, Vol. 9905. Society of Photo-Optical Instrumentation Engineers (SPIE) Conference Series, p. 99051K
- Predehl P., Andritschke R., Böhringer H., et al., 2010, In: *Space Telescopes and Instrumentation 2010: Ultraviolet to Gamma Ray*, Vol. 7732. Society of Photo-Optical Instrumentation Engineers (SPIE) Conference Series, p. 77320U
- Predehl P., Andritschke R., Bornemann W., et al., 2007, In: *UV, X-Ray, and Gamma-Ray Space Instrumentation for Astronomy XV*, Vol. 6686. Society of Photo-Optical Instrumentation Engineers (SPIE) Conference Series, p. 668617
- Predehl P., Bornemann W., Bräuninger H., et al., 2018, In: *Proceedings of the SPIE*, Vol. 10699. Society of Photo-Optical Instrumentation Engineers (SPIE) Conference Series, p. 106995H
- Predehl P., Friedrich P., Hasinger G., 2003a, In: Truemper J.E., Tananbaum H.D. (eds.) *X-Ray and Gamma-Ray Telescopes and Instruments for Astronomy*, Vol. 4851. Society of Photo-Optical Instrumentation Engineers (SPIE) Conference Series, p.314
- Predehl P., Friedrich P., Hasinger G., et al., 2003b, *Astronomische Nachrichten* 324, 128
- Predehl P., Hasinger G., Böhringer H., et al., 2006, In: *Space Telescopes and Instrumentation II: Ultraviolet to Gamma Ray*, Vol. 6266. Society of Photo-Optical Instrumentation Engineers (SPIE) Conference Series, p. 62660P
- Reynolds S.P., Keohane J.W., 1999, *The Astrophysical Journal* 525, 368
- Rho J., Petre R., 1998, *The Astrophysical Journal* 503, L167
- Sasaki M., 2019, *Interstellar Medium*, Lecture held at FAU
- Schaudel D., 2003, Ph.D. thesis, Ludwig-Maximilians-Universität München
- Schmid C., 2012, Ph.D. thesis, Friedrich-Alexander-Universität Erlangen-Nürnberg
- Sedov L.I., 1959, *Similarity and Dimensional Methods in Mechanics*, Academic Press, New York
- Seward F.D., Charles P.A., 2010, *Exploring the X-ray Universe*, Cambridge University Press
- Soderberg A.M., Berger E., Page K.L., et al., 2008, *Nature* 453, 469
- Stephenson F.R., Green D.A., 2002, *Historical supernovae and their remnants* 5
- Strüder L., Briel U., Dennerl K., et al., 2001, *Astronomy & Astrophysics* 365, L18

- Tappe A., Rho J., Reach W.T., 2006, *The Astrophysical Journal* 653, 267
- Taylor G., 1950, *Proceedings of the Royal Society of London Series A* 201, 159
- Truelove J.K., McKee C.F., 1999, *The Astrophysical Journal Supplement Series* 120, 299
- Truemper J., 1982, *Advances in Space Research* 2, 241
- Turner M.J.L., Abbey A., Arnaud M., et al., 2001, *Astronomy & Astrophysics* 365, L27
- van den Bergh S., 1976, *Astrophysical Journal* 208, L17
- Vink J., 2008, *Astronomy & Astrophysics* 486, 837
- Vink J., 2012, *The Astronomy & Astrophysics Review* 20, 49
- Vink J., Kaastra J.S., Bleeker J.A.M., 1997, *Astronomy & Astrophysics* 328, 628
- Vink J., Yamazaki R., Helder E.A., Schure K.M., 2010, *The Astrophysical Journal* 722, 1727
- Vitale V., 2004, Ph.D. thesis, Technische Universität München
- Voges W., Aschenbach B., Boller T., et al., 1999, *Astronomy & Astrophysics* 349, 389
- Vogt F., Dopita M.A., 2011, *Astrophysics and Space Science* 331, 521
- Weiler K.W., Panagia N., 1978, *Astronomy & Astrophysics* 70, 419
- Wells D.C., Greisen E.W., Harten R.H., 1981, *Astronomy & Astrophysics Supplement* 44, 363
- Westerlund B.E., 1969, *Astronomical Journal* 74, 879
- Westerlund B.E., Mathewson D.S., 1966, *Monthly Notices of the Royal Astronomical Society* 131, 371
- White R.L., Long K.S., 1991, *The Astrophysical Journal* 373, 543
- Willingale R., West R.G., Pye J.P., Stewart G.C., 1996, *Monthly Notices of the Royal Astronomical Society* 278, 749
- Wilms J., 2018, *Astrophysical Radiation Processes*, Lecture held at FAU
- Winkler, P. F. J., Laird F.N., 1976, *Astrophysical Journal* 204, L111
- Wolter H., 1952a, *Annalen der Physik* 445, 94
- Wolter H., 1952b, *Annalen der Physik* 445, 286
- Wosley S., Janka T., 2005, *Nature Physics* 1, 147
- Xiao X., Chen Y., 2008, *Advances in Space Research* 41, 416
- Yamaguchi H., Koyama K., Katsuda S., et al., 2008, *Publications of the Astronomical Society of Japan* 60, S141
- Zirakashvili V.N., Aharonian F., 2007, *Astronomy & Astrophysics* 465, 695

Acknowledgment

Used software and services

This research has made use of the *XMM* ESAS package.

This research has made use of ISIS functions (ISISscripts) provided by ECAP/Remeis observatory and MIT (<http://www.sternwarte.uni-erlangen.de/isis/>).

This thesis adopted scripts to create skyplots of source positions from Moritz Boeck and Felicia Krauss. Thank you for providing the scripts in the Remeis Wiki!

The “real” acknowledgment

First of all, I would like to thank my supervisor Manami Sasaki for allowing me to work on this interesting topic. And also for including me in her multiwavelength working group since I switched from the X-ray gang to a new challenge. Thanks for always having an open door to ask questions also those about the structure of Japanese addresses.

I would also like to thank Jonathan Knies and Manami for their patience when answering all my questions and teaching me how to work with XSPEC. In addition, thank you, Jonathan, for your helpful explanations and suggestions.

Thank you to Thomas Dauser and Christian Kirsch for solving my problems with SIXTE.

Another big thank you to our admins at the observatory for keeping the computers running and the software working.

Big thank you to Edith Day for doing all that bureaucratic paper work regarding Hiwis and for sending reminders every now and then to hand in timesheets or other documents. Without you the observatory would not run as smoothly as it does.

Special thanks to Steven Hämmerich, Dominic Bernreuther, and Eva von Gemünden for making the organization of the Open Day such fun. Although we were working hard (we were!) it felt easier with you guys around and we managed to create such an amazing event!

Thanks to Philipp Weber for getting my software run again when I was stuck with stupid mistakes and lost because of the lacking proper documentation. And also for having breakfast in my office (;)) and all our discussions and working together during our studies.

A thank you to Steven and Alexander Reichel for the funny train rides we had together and all the interesting and encouraging discussions and conversations.

Thanks to Katharina Egg for having some distracting time during hot summer days when building Jörn’s LEGO model of the moon landing.

Of course, thank you to my office mates Jakob Stierhof, Simon Kreuzer, Markus Dimpel, Eva, and Katharina (and sometimes Anna) for all the funny moments and very interesting discussions about astronomy, life and everything.

Thank you to Jörn for supporting me when applying for an ESAC traineeship. I had a great time there in Spain. And also thanks for letting me finally switch to Manami's working group.

Thank you to all the people at the observatory for the hard work and the fun and (of course!) all the cake! With cake everything is better! I really enjoyed the atmosphere at the Remeis observatory!

Thanks again to Steven and my sister for proofreading of my thesis and finding all my minor and major typos and mistakes.

Of course also thanks a lot to my family for their support during my studies and during my whole life!

Thanks to my boyfriend's family for including me into your family and accepting me as a family member.

Last but not least, thank you very much to my boyfriend Chris for enduring all my highs and lows during my studies and especially during the last year when working on my thesis. Thank you for giving me the opportunity to spend some time in Spain and for cheering me up when I felt homesick and I got mad about my flatmates and Spanish people and culture in general. I'm looking forward to our future!

A big thank you also to everyone whom I forgot to mention here by name but who supported me. Please forgive me to not have mentioned you by name!

Eigenständigkeitserklärung

Hiermit bestätige ich, dass ich diese Arbeit selbstständig und nur unter Verwendung der angegebenen Hilfsmittel angefertigt habe.

Ort, Datum

Melanie Lang